Characterizing Intermittent Turbulent Wave Kinetics and Energy Transfer via Three-Wave Coupling in Dipole-Confined Plasma

Mel Abler

Submitted in partial fulfillment of the
requirements for the degree of
Doctor of Philosophy
under the Executive Committee
of the Graduate School of Arts and Sciences

COLUMBIA UNIVERSITY

2021

Abstract

Intermittency of Fluctuation Power and Power Transfer via Three-Wave Coupling in Dipole-Confined Plasma Turbulence

Mel Abler

Plasmas confined by a dipole magnetic field exhibit interchange and entropy mode turbulence causing bursty intermittent transport of particles and energy [1]. On the Collisionless Terrella Experiment (CTX), this turbulence is dominated by low-frequency, long-wavelength modes with amplitudes and phases that vary chaotically in time [2]. We present a new paradigm for characterizing this turbulence by measuring the time-evolution of the fluctuation power spectrum and the instantaneous bispectrum using the continuous wavelet transform [3, 4] and computing the statistical properties of turbulent wave kinetics. We observe that both the fluctuation power and the energy transfer by three-wave coupling, or bispectrum, between these fluctuations can be intermittent. When antenna are used to actively launch waves into the turbulence, the intermittency of the driven waves decreases, while the intermittency of other waves increases. Similarly, application of active feedback [5] to amplify the turbulence decreases the intermittency of the wave energy, while suppressing feedback increases this intermittency. Measurements based on this new paradigm show that the transfer of wave energy to larger and smaller scales in a turbulent plasma is not steady but occurs in short and intense bursts, analogous to the better-known short bursts of particle transport in magnetized plasma.

Table of Contents

List of Tables

List of Figures

Acknowledgements

First and foremost, I want to thank my parents, Mike Abler and Brenda Abler, for their support and patience over the last seven years. You have always made time for me when I needed it and supported me in what I want to do, and I am so grateful. I would never have gotten here without you.

I also want to acknowledge my advisor, Mike Mauel, for creating a remarkably independent and self-directed doctoral experience. Thanks also to Jeff Levesque and Kyle Mandli, neither of whom was responsible for me but both of whom took the time to help me when I needed their expertise.

I'm eternally grateful to Emily Lichko and Jimmy Juno, friends who stepped up to advise and support me over the last year. I owe a particular debt to Emily, who single-handedly kept me in the field through a combination of encouragement, connecting me to exactly the right opportunity, and refusing to let me believe so many of the things I had come to internalize over my time in graduate school. I am also grateful to Chris Wright for his help and incredible patience as he mentored me through the process of learning to code.

Additional thanks go out to the friends who have been such imporant sources of support, ideas, and joy during my time in the APAM department: Bernard Lipat, Chris Wright, Alex Saperstein, Ian Stewart, Pat Byrne, Zane Martin, Jessie Oehrlein, Sai Sunku, E-Dean Fung, Max Terban, Liz Culbertson, Olivia Winn, and Josh Cabrera. All of you helped to keep me in the program long enough for this document to exist. Beyond the department, I also owe a great deal of my personal development over the past 7 years to my comrades from CAWDU, who reminded me that there is a world to fight for outside of research. And of course to the friends who predate my time in New York, particularly Stevi Matz, Tricia Horvath, and Alex Watras for all the support, proofreading, empathy, and encouragement over the years. I'm so glad we have stayed close despite so many

changes in time zones, jobs, and relationships. You're chosen family.

I also owe a debt to my coworkers at TopRow. I learned from you what it feels like to be a valued and respected part of a community, and I will carry that with me for the rest of my life. In particular, I want to thank Jasper Smink for making every accommodation to allow me to have the unconventional dual career path that I've chosen, and Milan Kamphuis for taking on extra responsibility to allow me to focus on completing this thesis. My deepest thanks to all the rowers I've worked with over the years, especially Hilary Callahan and Jessica Sabat, for their faith and support. You have no idea how much it kept me going when I needed it most.

Finally, so many thanks and so much love to my wonderful, fluffy nugget of a cat, Sebastian. Having another living being to care for and interact with every day has kept me sane through both graduate school and a pandemic. He's a pretty good enforcer of work-life balance too.

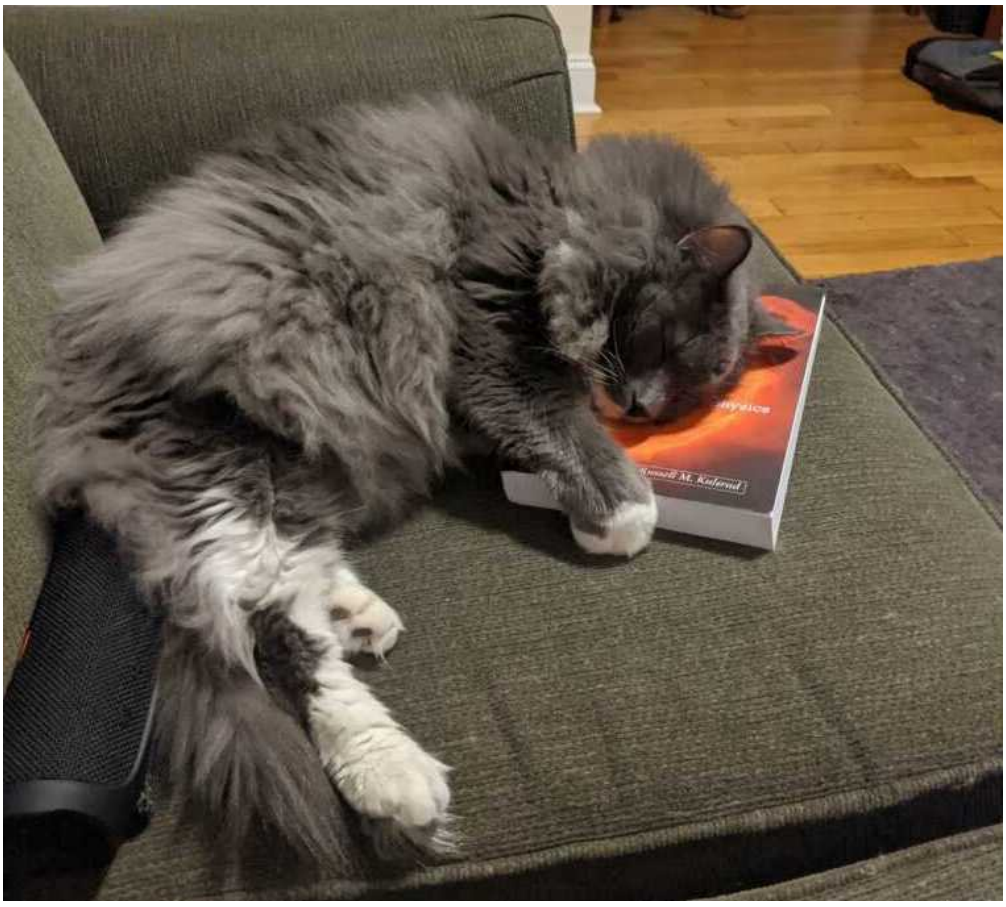

Chapter 1: Introduction

Describing the turbulent motion of fluids has challenged researchers for more than a century, even as these flows are ubiquitous in daily life. Plasmas also display turbulent behavior similar to that of neutral fluids, but with the added complexity of electromagnetic effects. In both cases, the turbulent flows are made up of eddies at many scales which interact with each other via complex nonlinear processes. Despite decades of development in theory, simulation, and experiment, we still lack a complete understanding of turbulent systems. This thesis will focus on experiments describing the wave-wave interactions between electrostatic fluctuations in a turbulent plasma confined by a dipolar magnetic field, how those interactions can be changed by feedback or injected waves, and characterize the intermittency of both the fluctuation power and the transfer of that power between frequencies via three-wave coupling.

Note that this chapter does not pretend to be a comprehensive discussion of the rich field of plasma turbulence, but is instead a brief review of aspects most relevant to the results presented in this work.

1.1 Dipole-Confined Plasmas

Plasmas confined by dipolar magnetic fields are best exemplified in nature by planetary magnetospheres. The Earth, Jupiter, and Saturn all have strongly dipolar magnetic fields which confine plasmas composed primarily of protons and electrons, along with some helium ions from the solar wind mixed with ionized gases from the atmosphere of the planet. Magnetospheric field lines terminate at the poles of the planet, intersecting the planet's atmosphere and precipitating particles which cause aurora. The plasma contained in a magnetosphere is nonuniformly distributed between relativistic radiation belts (such as the Van Allen belts at 2-6 Earth radii), a hot ring current,

and a cold plasmasphere (Figure 1.1) [Fok 2020 Ring Current Investigations]. Magentospheric plasmas exhibit a number of features and instabilities which can be recreated and further studied in the laboratory, including the interchange instability [Singh 2011 Planetary and Space Science].

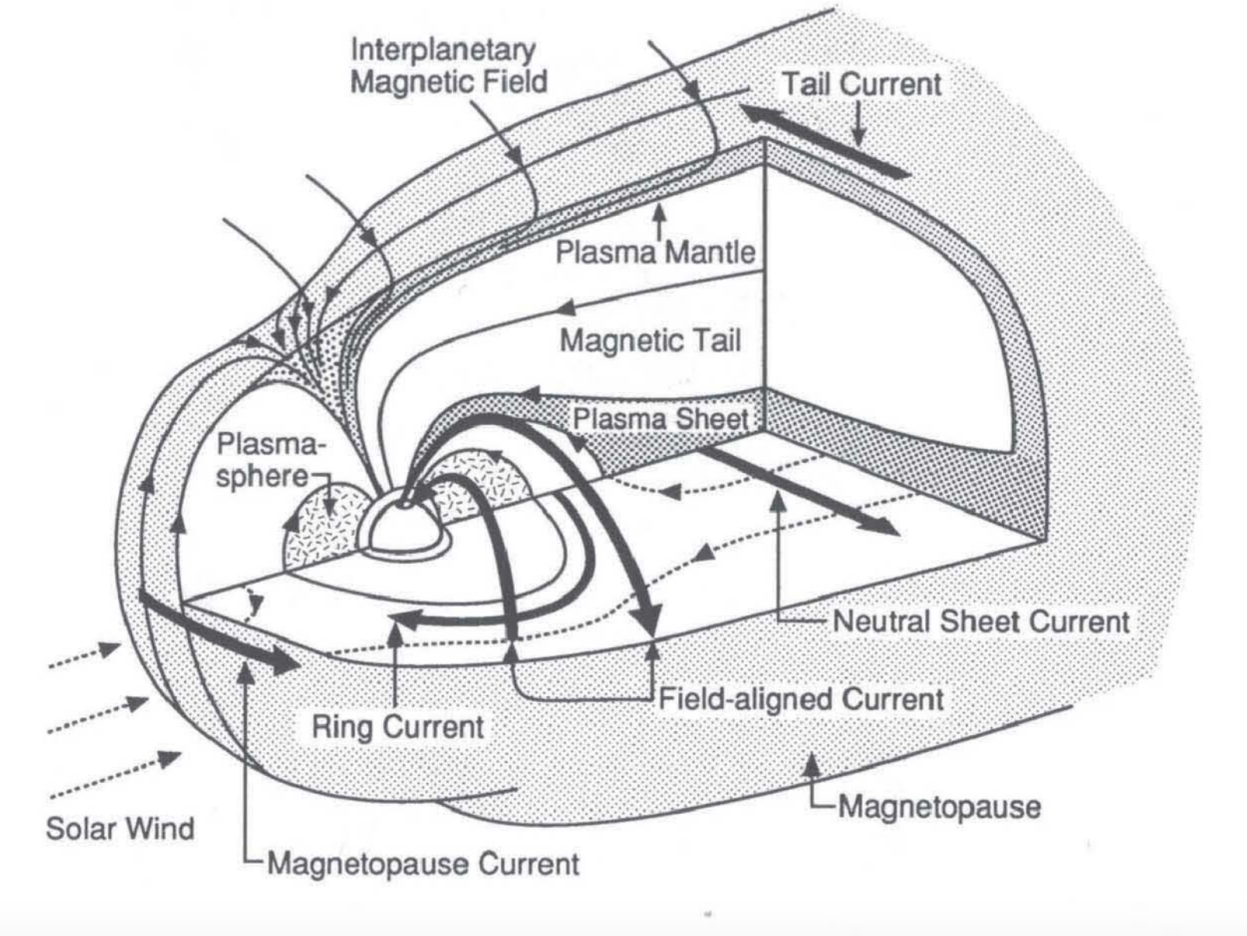

Figure 1.1: A cartoon of the Earth's magnetosphere highlighting the locations of various plasma populations and currents [6].

1.1.1 Laboratory Experiments

There is a rich history of dipole-confined plasma experiments dating back over a century to Birkeland's "terella" (little Earth) experiments. Birkeland's work was among the first controlled plasma experiments and facilitated some of the earliest laboratory studies of the aurora [7]. Over the last 25 years, larger scale laboratory experiments have also been developed. Experiments like the Levitated Dipole Experiment (LDX) and Ring Trap 1 (RT-1) use a levitated superconducting

current ring to produce the confining magnetic field and microwave heating to produce the plasmas. Because the ring is levitated, the magnetic field lines close on themselves, rather that intersecting a planetary atmosphere or other conducting surface. The (relatively) small closed field lines mean there are no currents parallel to the field lines ($k_{\|} \approx 0$), as demonstrated by experimental measurements. Dipolar magnetic fields lack magnetic shear, and the collective motion of the plasma is governed by gradients in density and pressure perpendicular to the magnetic field which drive the interchange and entropy instabilities of interest in this thesis. These levitated experiments have focused on studies of highly peaked density and pressure profiles [8, 9, 10, 11]. The Collisionless Terella Experiment (CTX) has similarly peaked profiles, but uses a mechanically supported dipole magnet rather than a levitated ring. This means that the field lines terminate on the insulating surface of the magnet casing, rather than closing on themselves or intersecting a conducting layer such as an ionosphere; there are still no field-aligned currents due to the insulating termination of the field lines. The plasma is again produced using microwave heating, and has been a platform for studying interchange modes, interchange turbulence,and radial transport [12, 13, 14, 1, 2, 5]. In both CTX and LDX, the field-line integral of the divergence of the perpendicular magnetic drift must be equal to zero [15], meaning we cannot accumulate plasma only on particular field lines. Correspondingly, the electron diamagnetic current must be balanced by the ion polarization current. Roberts et al [5] demonstrated that introducing an additional current via a biasing electrode can simulate the effects of field-aligned currents in CTX and impose an effective "ionospheric regulation" on the plasma fluctuations.

Interchange instabilities are not unique to laboratory dipole experiments and can occur in any plasma with the appropriate pressure or density profiles, including rotating magnetospheres [16], plasmaspheres [17, 18], and in the scrape-off layer of tokamaks [19, 20]. The prevalence of interchange instabilities in magnetized plasmas has motivated a variety of laboratory investigations of interchange modes driven by everything from pressure and density gradients [[2, 1, 5, 21], to plasma rotation [22, 14, 23, 24], to energetic particles [25, 13].

1.2 Physics of Dipole-Confined Plasmas

To fully describe the motion of a plasma confined by a magnetic field, one must account for both the motions of individual particles, and the bulk, fluid-like motion of the whole plasma. Often, it is more practical to focus on only one description at a time, bearing in mind that one description will not capture all of the dynamics. We will focus first on describing the motions of a single particle confined by a dipole magnetic field, then move to the magnetohydrodynamic (fluid-like) description and associated instabilities.

1.2.1 Single Particle Motions

There are three important single-particle motions in a dipole magnetic field: cyclotron, bounce, and drift. Each motion has a characteristic frequency and adiabatic invariant associated with a conserved quantity. These are listed in Table 1.1 and shown in Figure1.2.

Motion	**Frequency**	**Adiabatic Invariant**	**Conserved Quantity**
Cyclotron	$\omega_c = \frac{\lvert q\rvert B}{m_q}$	$\mu = \frac{m_q v_\perp^2}{2B}$	flux inside gyro orbit
Bounce	$\omega_b = \frac{2\pi}{\int \frac{ds}{v_\parallel}}$	$J = \int_a^b m_q v_\parallel ds$	action along bounce path
Drift	$\vec{u}_d = \frac{\mu}{q}\frac{\vec{\nabla}B\times\vec{B}}{B^2}$	$\psi = \oint m_q E_\perp d\varphi$	flux inside drift orbit

Table 1.1: Single particle motions in a dipole magnetic field, their associated adiabatic invariants and conserved quantities.

1.2.2 Magnetohydrodynamics and the Interchange Instability

A fluid description can often be a simple and effective way to describe plasma dynamics, even in regimes of low collisionality. Precisely how this simplification is done depends upon the specific plasma phenomena being studied: one can either treat the entire plasma as one fluid (ideal magnetohydrodynamics), or treat the ions and electrons as two separate interacting fluids each with different conditions (two-fluid magnetohydrodynamics).

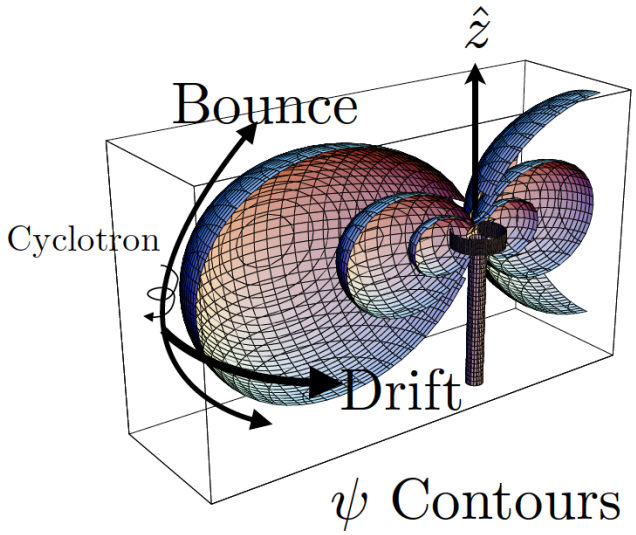

Figure 1.2: Single particle motions in a dipole magnetic field with contours of constant ψ.

The ideal MHD case is simpler and easier to visualize, as we can treat the field lines as being "frozen" to the plasma [26]. By "frozen," we mean that the magnetic field must move with the plasma; as a consequence, the system can be decomposed into tubes of equal magnetic flux. If a flux tube moves radially outward, it moves into a region of lower magnetic field [27], which increases the volume of the flux tube and adiabatically cools it. For a flux tube to move outward, it must exchange places with another flux tube moving inward, whose volume will be reduced in the region of stronger magnetic field and lead to adiabatic heating. This swapping of flux tubes is known as an electrostatic interchange (or flute) instability [28]. Note that by definition there is no change to the magnetic topology and there are no parallel currents. This mode is the plasma equivalent of the Rayleigh-Taylor instability in neutral fluids, in which a heavy fluid is supported a against gravity by a lighter fluid. In neutral fluids the instability grows when the pressure gradient is anti-parallel to the gravitational force; in plasmas it grows when the pressure gradient is antiparallel to the radius of curvature of the magnetic field; such plasmas are often referred to as having "bad" curvature.

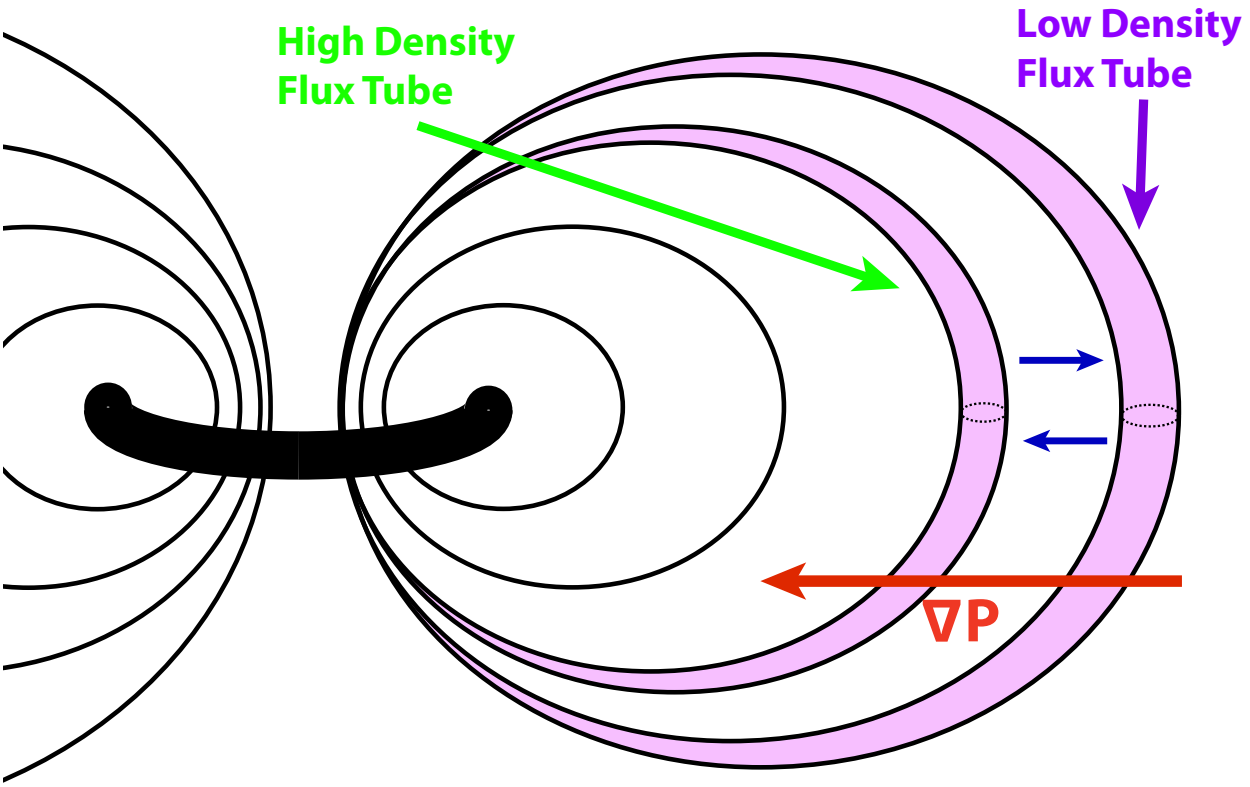

Figure 1.3: Cartoon demonstrating the interchange motion of flux tubes.

Following the derivation of Rosenbluth and Longmire [28], a plasma is interchange unstable when

$$\Delta E = \delta p \delta V + \gamma p \frac{(\delta V)^2}{V} = V^{-\gamma} \delta \left(pV^{\gamma}\right) \delta V < 0. \tag{1.1}$$

Plasma confinement devices are considered to have "good" curvature when $\delta V < 0$ (the flux tube volume is reduced as it moves radially outward), but dipoles have "bad" curvature ($\delta V > 0$). Thus, the only way to stabilize a dipole against the ideal interchange instability is to have the other differential term ($\delta \left(pV^{\gamma}\right)$) be greater than zero. The volume of a flux tube varies like R^4 [29] (see Figure 2.3); applying this we see that

$$\delta \left(pV^{\gamma}\right) \sim \delta \left(pR^{4\gamma}\right). \tag{1.2}$$

To achieve marginal stability ($\Delta E = 0$), we would require $p \sim R^{-4\gamma}$, indicating a sufficiently

gradual pressure profile can stabilize the ideal interchange mode. A similar argument can be made using the density profile [30]. The effects of the pressure [9] and density [8] profiles have been studied on LDX and show rough agreement with this theory.

Because a marginally stable pressure profile can be achieved with a wide variety of plasma density and temperature profiles, a more complete picture of the instabilities at play in a dipole-confined plasma requires the use of the two-fluid MHD framework to include the entropy mode [21, 31].

1.2.3 Dipole Coordinates

Plasma dynamics are highy dependent on magnetic field strength, which makes it convenient to use the dipole field as a coordinate system. Note that for the purposes of this section we will set $\mu_0/4\pi = 1$, as this factor does not alter the calculation. From undergraduate electrodynamics [32], the field of a point dipole can be written in spheical coordinates as:

$$\vec{B} = \frac{M}{r^3}\left(2\cos\theta\hat{r} + \sin\theta\hat{\theta}\right), \tag{1.3}$$

which means that

$$|\vec{B}| = \frac{M}{r^3}\sqrt{1 + 3\cos^2\theta}. \tag{1.4}$$

To visualize the geometry of a magnetic dipole, we can use the equation of a field line, which we find from the ratio of the field components:

$$\frac{1}{r}\frac{dr}{d\theta} = \frac{B_r}{B_\theta} = \frac{\frac{2M}{r^3}\cos\theta}{\frac{M}{r^3}\sin\theta} = \frac{2\cos\theta}{\sin\theta}. \tag{1.5}$$

Rearranging terms and integrating, we see

$$\int \frac{1}{r} dr = \int \frac{2\cos\theta}{\sin\theta} d\theta$$
$$ln\,(r) = ln\left(\sin^2\theta\right) + C$$
$$r = L\sin^2\theta$$

where the equatorial radius $L = r\,(\theta = \pi/2)$. These field lines can be seen in black in Figure 1.4.

Note the absence of φ in the above equations, meaning the dipole field strength is symmetric in the azimuthal angle, but varies with the polar angle and radius. A simpler description would have only one variable change as a particle moves along a field line; this can be achieved by moving to the Clebsch representation, which describes the system in terms of magnetic flux ψ, magnetic scalar potential χ, and azimuthal angle φ. (A detailed description of the transformation from spherical coordinates to Clebsch coordinates is given in Appendix B of [29]). In Clebsch coordinates - also known as dipole coordinates - magnetic flux acts as a radial coordinate, magnetic scalar potential indicates position along a field line, and the magnetic field can be written (ignoring a factor of 2π) as

$$\vec{B} = \nabla\varphi \times \nabla\psi = \nabla\chi. \tag{1.6}$$

The scalar fields used in Clebsch coordinates and their gradients are explicitly defined (in spherical coordinates) as:

$$\varphi = \varphi \qquad \psi = \frac{M}{r}\sin^2\theta \qquad \chi = \frac{M}{r^2}\cos\theta \tag{1.7}$$

$$\nabla\varphi = \frac{1}{r\sin\theta}\hat{\varphi} \tag{1.8}$$
$$\nabla\psi = -\frac{M}{r^2}\sin^2\theta\hat{r} + 2\frac{M}{r^2}\sin\theta\cos\theta\hat{\theta} \tag{1.9}$$
$$\nabla\chi = -2\frac{M}{r^3}\cos\theta\hat{r} - \frac{M}{r^3}\sin\theta\hat{\theta}. \tag{1.10}$$

Additionally, it should be noted that at the equator ($\theta = \pi/2$) the magnetic flux is inversely pro-

portional to the radius (see equation 1.7), which provides a convenient coordinate for parametrizing a magnetic flux surface. Every field line can thus be denoted by two dimensions (ψ, φ), corresponding to the natural two-dimensional magnetic coordinates to describe plasma equilibrium and interchange mode dynamics.

Dipole coordinates can be see in Figure 1.4, along with spherical coordinates and dipole field lines for reference.

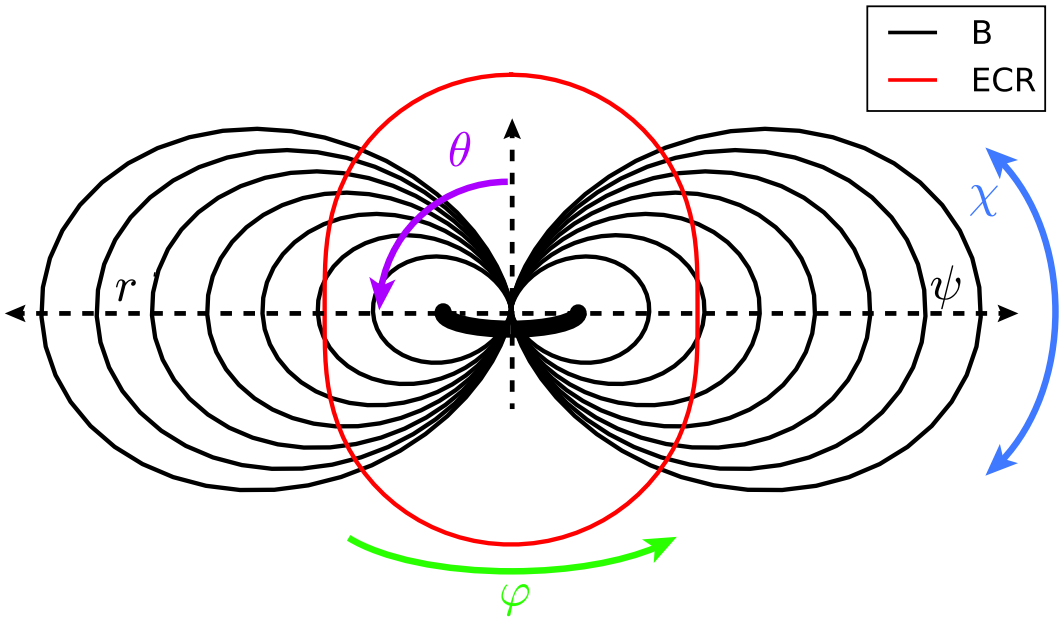

Figure 1.4: Dipole field lines with both spherical (r, θ, φ) and dipole (ψ, χ, φ) coordinates.

To re-write the equation for dipole field lines in dipole coordinates, we use

$$B^2 = \vec{B} \cdot \vec{B} = \vec{B} \cdot \nabla\chi = B\frac{d\chi}{dl}. \tag{1.11}$$

Solving for dl, we see

$$dl = \frac{d\chi}{B}, \tag{1.12}$$

which will always be directed along B, as $\vec{B} = \nabla\chi$.

It is often convenient to describe volumes in dipole coordinates in terms of magnetic flux tubes, as the volume of these flux tubes plays an important role in the dynamics of dipole confined

plasmas:

$$V = \int A \cdot dl = \int \frac{\psi}{B} dl = \psi \int \frac{1}{B} dl \tag{1.13}$$

Solving for the differential volume δV per unit magnetic flux, we describe a flux tube as

$$\delta V = \frac{V}{\psi} = \int \frac{dl}{B}. \tag{1.14}$$

Subsitituting our definition of dl in dipole coordinates into our flux tube description, we can now define the differential magnetic flux tube volume as

$$\delta V(\psi) \equiv \int_{-\infty}^{+\infty} \frac{d\chi}{B^2}. \tag{1.15}$$

Integrating along the field lines over a differntial flux tube volume dramatically simplifies the description of low frequency plasma dynamics by effectively averaging over a flux tube.

Changing back to spherical coordinates makes the integration in equation 1.15 much easier to solve. We begin with

$$\chi = \frac{M}{r^2} \cos\theta. \tag{1.16}$$

Solving our previous definition of ψ (equation 1.7) we get $r(\psi, \theta)$, which can be subsituted back into equation 1.16 to give

$$\chi = \frac{M \cos\theta}{\left(\frac{M}{\psi} \sin^2\theta\right)^2} = \frac{\psi^2 \cos\theta}{M \sin^4\theta}. \tag{1.17}$$

Treating ψ as fixed, we can differentiate to find an expression for $d\chi$:

$$d\chi = \frac{\partial \chi}{\partial \theta} d\theta = -\frac{\psi^2}{M} \frac{1 + 3\cos^2\theta}{\sin^5\theta} d\theta. \tag{1.18}$$

Similarly, we substitute $r(\psi, \theta)$ into our previous definition for $|\vec{B}|$ (equation 1.4) and squaring:

$$B^2 = \frac{M^2}{r^6} \left(1 + 3\cos^2\theta\right) = \frac{\psi^6 (1 + 3\cos\theta)}{M^4 \sin^{12}\theta}. \tag{1.19}$$

Substituting our new solutions for B^2 and $d\chi$ into our integral for $\delta V(\psi)$ and solving yields:

$$\delta V(\psi) = \int_{\pi}^{0} \frac{-\frac{\psi^2}{M}\frac{1+3\cos^2\theta}{\sin^5\theta}d\theta}{\frac{\psi^6\left(1+3\cos^2\theta\right)}{M^4\sin^{12}\theta}} = -\frac{M^3}{\psi^4}\int_{\pi}^{0}\sin^7\theta d\theta = \frac{32}{35}\frac{M^3}{\psi^4} \approx 0.91\frac{M^3}{\psi^4}. \tag{1.20}$$

Note the integration in θ is done from π to 0 because this is the direction of increasing χ (our original intergration variable) in dipole coordinates.

From this definition of the differential magnetic flux tube volume, we can define the flux-tube average of a quantity X as

$$\langle X \rangle \equiv \frac{1}{\delta V}\int_{-\infty}^{+\infty}\frac{X d\chi}{B^2}. \tag{1.21}$$

1.3 Turbulence in Two-Dimensional Systems

Quasi-two-dimensional turbulence has been observed in planetary atmospheres such as Earth's and Jupiter's [33, 34], the scrape-off layer of toroidal fusion devices [35], and strongly magnetized laboratory plasma devices [36, 37, 38], among other systems. Turbulence in such two-dimensional systems exhibits unique behaviors. Fluid motions are described by the Navier-Stokes equation:

$$\rho\frac{D\vec{u}}{Dt} = -\vec{\nabla}p + \vec{\nabla}\cdot\overleftrightarrow{\tau} + \rho\vec{F}, \tag{1.22}$$

where D/Dt is the material derivative $\partial/\partial t + \vec{u}\cdot\vec{\nabla}$, ρ is the density, $\vec{u}$ is the flow velocity, p is the pressure, $\overleftrightarrow{\tau}$ is the stress tensor, and $\vec{F}$ represents all external forces and accelerations acting on the fluid (such as gravity). If we assume that the fluid is incompressible, this simplifies to:

$$\frac{D\vec{u}}{Dt} = \frac{\partial\vec{u}}{\partial t} + \left(\vec{u}\cdot\vec{\nabla}\right)\vec{u} = -\frac{\vec{\nabla}p}{\rho_0} + \nu\nabla^2\vec{u} + \vec{F}, \tag{1.23}$$

where ν is the kinematic viscosity and ρ_0 is the density of the fluid.

By assuming that our 2D motion takes place in the $x-y$ plane and taking the curl of Equation

1.23, we can generate a similar equation which applies to the vorticity $\omega = (\nabla \times \vec{v}) \cdot \hat{z}$:

$$\frac{D\omega}{Dt} = \frac{\partial \omega}{\partial t} + \left(\vec{u} \cdot \vec{\nabla}\right) \omega = \vec{\nabla} \times \vec{F} \cdot \hat{z} + \nu \nabla^2 \omega. \tag{1.24}$$

If the curl of the external forces is in-plane ($\vec{\nabla} \times \vec{F} \cdot \hat{z} = 0$) and $\nu = 0$, vorticity will be conserved. This is similar to kinetic energy being conserved in Equation 1.23 if there are no external forces, dissipation (from viscosity), or internal pressure gradients.

A fundamental difference between two and three dimensional turbulence is in the conserved quantities and the movement, or cascade, of these quantities in wavenumber space. Perhaps most importantly, 3D turbulence only conserves energy and is characterized by a cascade of energy to higher wavenumbers (smaller spatial scales), referred to as a "forward" energy cascade [39, 40, 34]. When energy is injected into the system at some scale k_i, it is transferred to smaller and smaller scales (larger and larger k) until it reaches the dissipation scale k_d whereby some process, such as viscous damping, dissipates the energy as heat. This forward cascade follows a $k^{-5/3}$ power law in the inertial range (between k_i and k_d) [41]. Contrastingly, 2D turbulence conserves both energy and enstrophy (mean-squared vorticity $Z = \langle \frac{1}{2} \omega^2 \rangle$) [42]. This results in a forward (to smaller scales/larger k) enstrophy cascade following a k^{-3} power law and an inverse energy cascade (to larger scales/lower k) following a $k^{-5/3}$ power law (Figure 1.5).

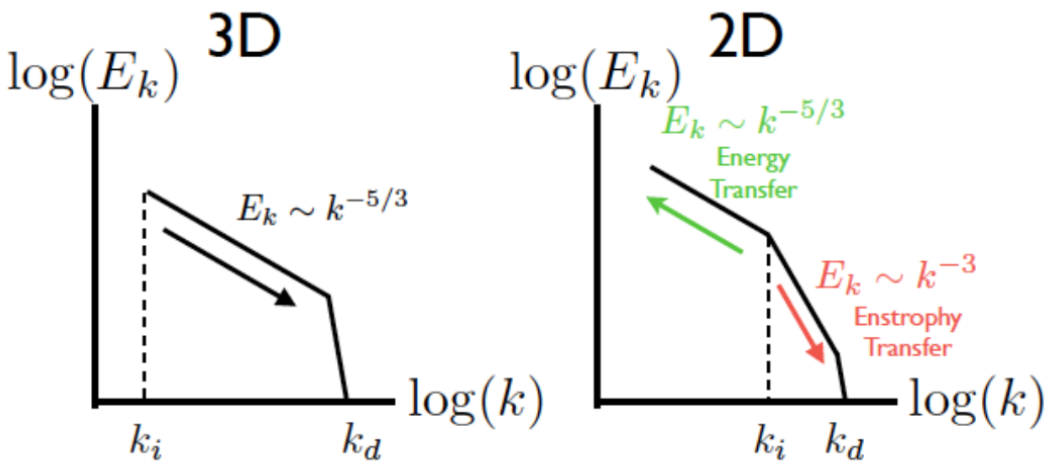

Figure 1.5: Cartoon depiction of the spectral shapes and directions of energy transfer for 3D (left) and 2D (right) turbulence.

Note that these cascades refer to net effects; in practice, some amount of the energy injected at scale k_i in 2D turbulence goes to smaller scales (forward cascade), but more goes to larger scales (inverse cascade). To demonstrate this, assume we can inject energy into some scale $k_i = 2k_0$ and $k_0 < k_i < k_1 = 3k_0$. Conservation of energy and enstrophy then become

$$\delta E_0 + \delta E_i + \delta E_1 = 0 \tag{1.25}$$

$$\delta Z_0 + \delta Z_i + \delta Z_1 = 0 = k_0^2 \delta E_0 + k_i^2 \delta E_i + k_1^2 \delta E_1. \tag{1.26}$$

The above system can be solved for δE_0, δE_1, δZ_0, and δZ_1 in terms of k_i and E_i:

$$\delta E_0 = -\frac{5}{8}\delta E_i \qquad \delta E_1 = -\frac{3}{8}\delta E_i \tag{1.27}$$

$$\delta Z_0 = k_0^2 \delta E_0 = -\frac{5}{32} k_i^2 \delta E_i = -\frac{5}{32}\delta Z_i \qquad \delta Z_1 = k_1^2 \delta E_1 = -\frac{27}{32} k_i^2 \delta E_1 = -\frac{27}{32}\delta Z_i. \tag{1.28}$$

Equation 1.28 clearly shows that most of the enstrophy moves to the larger k_1 (smaller scale), while more of the energy moves to the smaller k_0 (larger scale).

1.3.1 Two-Dimensional Interchange Turbulence in Dipole Plasmas

Because low-frequency interchange motion is definitionally perpendicular to the magnetic field, it is essentially two-dimensional [43]. The electrostatic field is constant along a magnetic field line, and perpendicular gradients of the electric field cause plasma to convect and mix. For laboratory dipole experiments, the magnetic field lines neither bend nor twist significantly, field-aligned currents are weak, the parallel wavelength $k_{\|} \approx 0$, and interchange instabilities lead to fully-developed two-dimensional turbulence exhibiting the expected power law fluctuation spectra [2]. Such plasmas also exhibit highly intermittent particle transport caused by field-aligned, low-frequency chaotic vortices which generate intermittent filaments [1]. A description of the turbulence specific to CTX can be found in Section 2.3.

1.4 Modifying Plasma Turbulence

Many experiments have used feedback to interact with unstable plasmas [44, 45, 46]. Such feedback can involve directly applying currents or using control coils to stabilize specific modes [47, 48, 49, 50]. This section reviews experiments that apply electrostatic feedback using biasable probes, as that is the technique used in the CTX feedback system.

1.4.1 Feedback on Turbulent Plasmas

Researchers on the Texas Experimental Tokamak (TEXT) experiment [51] have used a biasable electrode at the edge of a tokamak to apply feedback to drift-wave turbulence by meansuring field-aligned potential fluctuations then applying a similar bias to that same field line [52, 53]. This feedback is able to significantly amplify or suppress the turbulence near the biasing electrode, with the effect being reduced further away on the field line (Figure 1.6). Amplifying feedback also reduced the bandwidth of the turbulent spectrum, while suppression maintained the turbulence's initial broad frequency range. Although the drift-wave turbulence on TEXT is distinct from the interchange turbulence on CTX, the TEXT experiments demonstrate that a biasable probe connected

to measurements of local floating potential is a viable local feedback system.

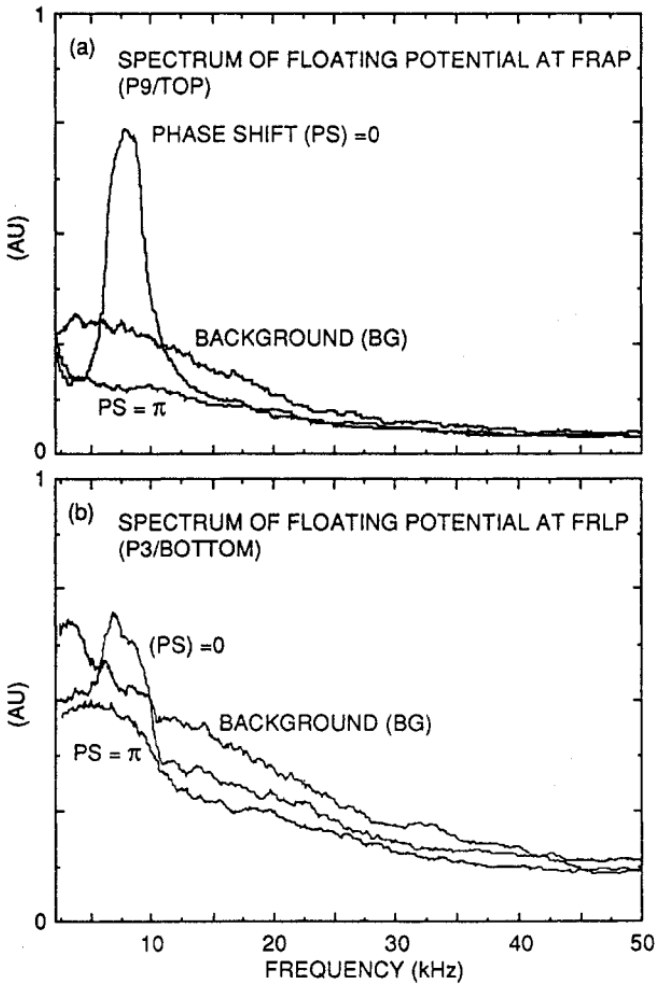

Figure 1.6: Figure 8 of [52], demonstrating the phase and distance dependence of the TEXT electrostatic feedback system.

1.4.2 Feedback on Interchange Unstable Plasmas

In an early case of feedback being applied to an interchange-unstable plasma, Prater et al used a sensor to measure fluctuations in the density of a plasma in a multipole-like magnetic geometry with bad curvature and a steep pressure gradient [54]. The density fluctuations were then phase shifted and amplified before being applied to the plasma by capacitively coupled biasing electrodes. Scans of the applied phase shift and gain, as well as tuning of a plasma collimator, revealed optimal

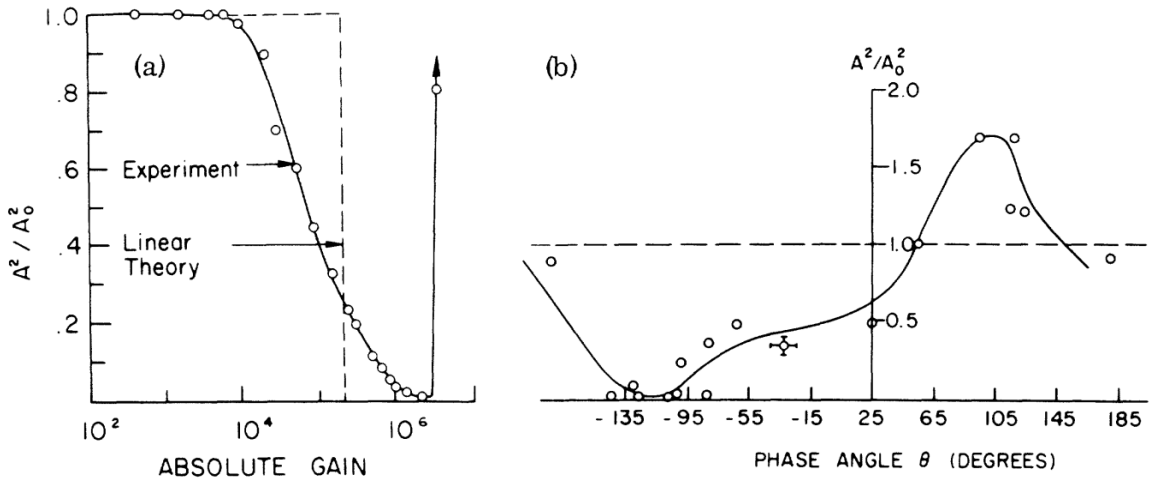

Figure 1.7: Figure 3 of [54], demonstrating the amplification or suppression of a flute mode using feedback.

parameters to significantly suppress the dominant $m = 1$ flute mode present in the system (Figure 1.7). While this system has a single dominant unstable mode rather than the broadband interchange turbulence found in CTX, it demonstrates feedback suppression of an interchange instability.

1.4.3 Feedback on Interchange Turbulent Plasmas

Most recently, Roberts [5] combined the approches discussed above to apply feedback to an interchange-turbulent dipole plasma, and demonstrated that different phase shifts allowed for maximum broadband amplification ($-45°$) or suppression ($+135°$) of the turbulent fluctuations (Figure 1.8). He also demonstrated that the decreased response to feedback with distance holds as a cross-field effect in CTX, rather than along the same field line as on TEXT. A further discussion of this feedback system can be found in Section 2.5 of this work, with greater detail in Chapter 3 of [29].

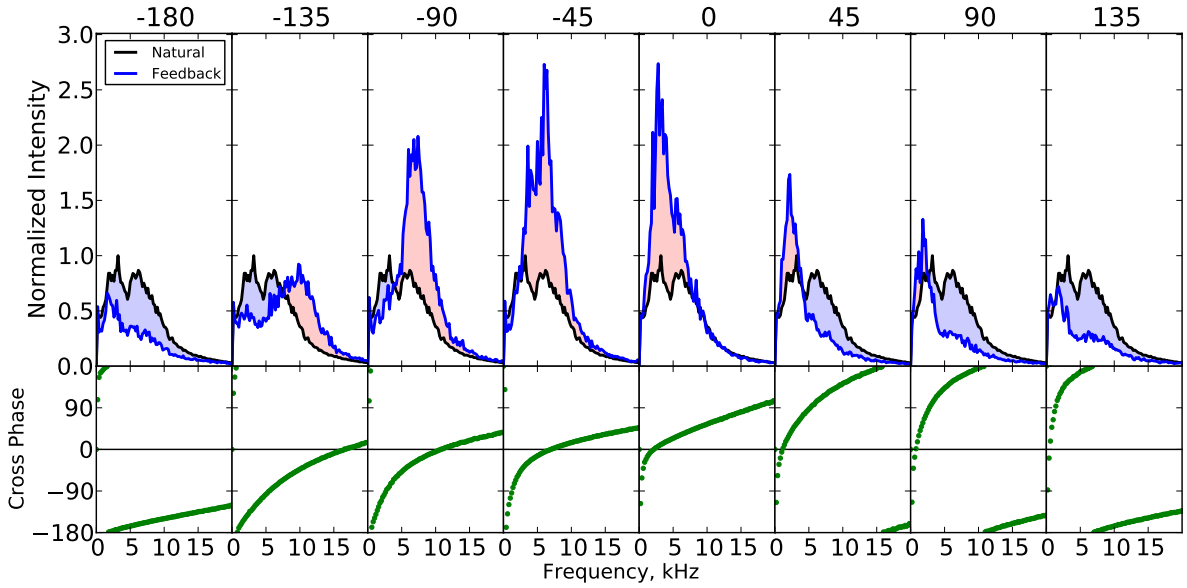

Figure 1.8: Figure 4.10 of [29], demonstrating the broadband amplification and suppression of interchange turbulence on CTX using electrostatic feedback.

1.5 Intermittency

Intermittency is a defining characteristic of turbulence, and can be described as "the nonuniform distriubtion of eddy formations in a stream" [55]. Spatial intermittency occurs when turbulent eddies are generated over a wide range of scales but do not fill the fluid volume, only irregular sub-volumes [56]; this is associated with sharp gradients and coherent structures. Temporal intermittency occurs when fluctuations appear as "bursts" in time with varying durations and is characteristic of the turbulent cascade. Matthaeus and co-authors review the properties of spatial and temporal intermittency in both fluids and plasmas [57]. Intermittency is related to nonlinear phase-space structures called "holes" and "clumps" which were originally found in electrostatic turbulence simulations [58, 59]. Temporal intermittency has been associated with the inverse cascade of two-dimensional turbulence, as described in Section 1.3.

Descriptions of turbulence often use statistical averages of the underlying intermittent quantities. In plasmas confined by dipolar magentic fields, this average turbulent particle flux has been shown to correspond to a quasilinear model of particle flux based on a random collection of low-

frequency waves [1, 8, 21]. The phase space structures of the turbulent eddies leading to energetic transport have been measured directly [12] and showed a correspondence between the bursts of outward energentic particle flux and a time-averaged quasilinear approximation [60]. Observations of bursty changes in plasma properties are common wherever plasmas turbulence is studied. Satellite missions and ground-based observers have found intermittency in turbulent fluctuations downstream of the Earth's bowshock [61], as well as in the Earth's magnetotail [62], magnetosheath [63], and magnetopause [64]; the Galileo mission also found intermittency in Jupiter's plasma sheet [65]. Both velocity and magnetic fluctuations in the solar wind show intermittency [66, 57] , with compressive magnetic fluctuations being the most intermittent [67]; this intermittency increases with heliocentric distance in the fast solar wind, but is relatively constant in the slow wind [67]. Most related to this work, intermittency in turbulence has also been widely observed in laboratory devices, from spheromaks [68] and helimaks [69, 70] to the scrape-off layers of tokamaks [71, 72, 73], where intermittent structures can account for more than 50% of radial particle flux.

Although temporal and spatial averages can be helpful when studying plasma turbulence, understanding the underlying nonlinear processes requires careful statistical representation. Previous studies of plasma turublence in a laboratory dipole have shown intermittent bursts of both ion saturation current and floating potential [1, 8], as characterized by the kurtosis of the respective probability distribution functions (PDFs) (see Section 3.6 for further explanation of the kurtosis).

Intermittency in turbulence is not restricted to particle flux, but can also appear in fluctuation power. The intermittency of wave power was first established in fully developed boundary layer turbulence measured with a bank of tuned filters [74]. These measuments are presented in Figure 1.9 and clearly show intermittent bursts of fluctuation power at all measured frequencies. The kurtosis of the velocity distribution function increases with frequency, meeting the criteria for intermittency laid out by Frisch [34]. The first measurements of intermittent fluctuation power in plasma turbulence were made by van Milligen et al [4] at the Advanced Toroidal Facility (ATF), and relied on the wavelet transform to separate frequencies, rather than individual filters. Van

Milligen's work extends the study of intermittency to the phase-coupling of waves in plasma turbulence, noting that short bursts of coherence in the summed wavelet bicoherence indicate that this process must be intermittent. The bulk of the intermittency comes from diffuse structures at higher frequencies, while the coupling of single modes to the broadband spectrum is relatively constant.

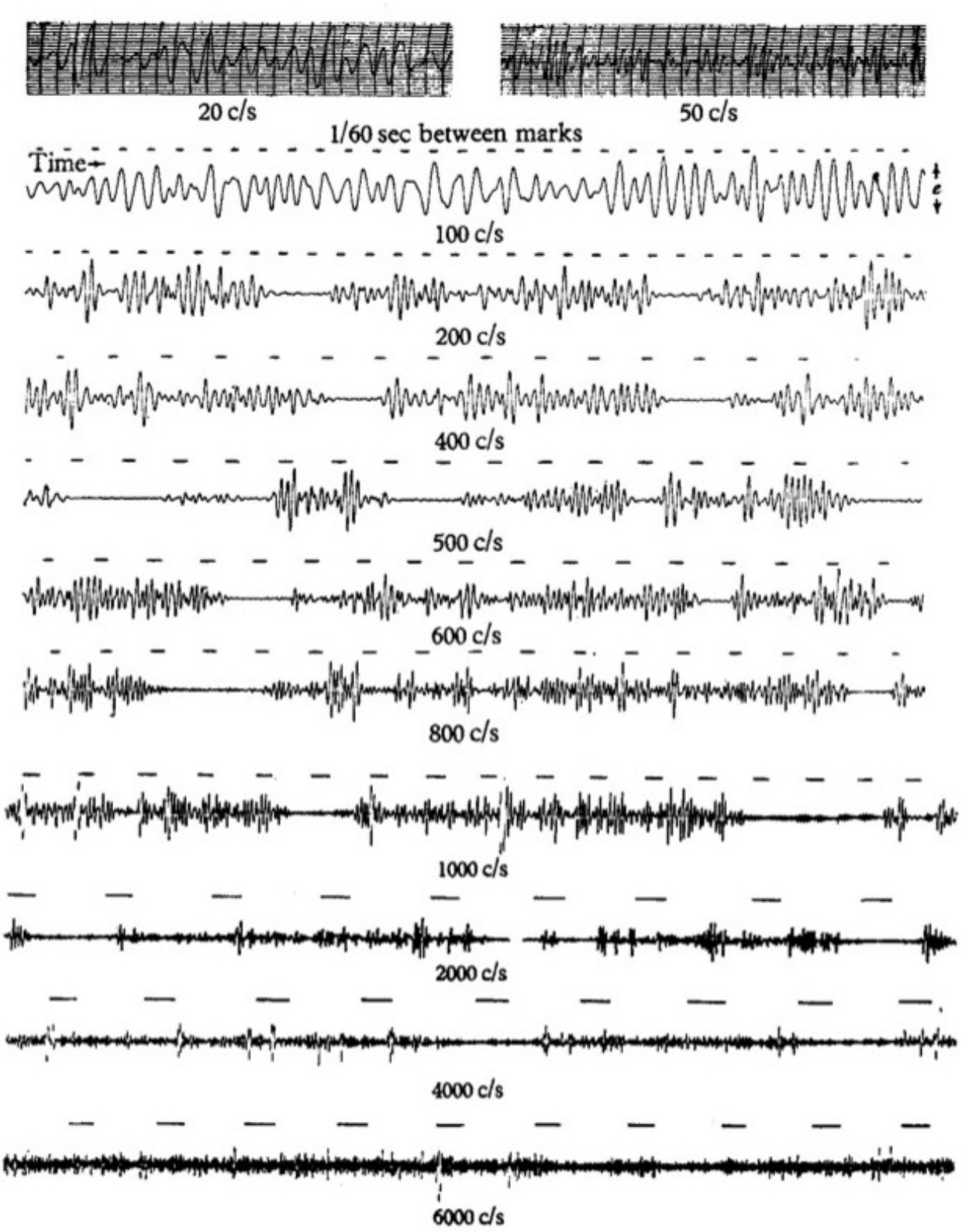

Figure 1.9: Figure 5 of [74], showing the intermittency of fluctuation power at a variety of frequencies in boundary layer turbulence 0.005 in from a pipe wall.

1.6 Organization of this Thesis

The remainder of this thesis presents the first application of wavelet transform-based techniques to a laboratory dipole plasma and strives to answer three questions:

1. What are the temporal dynamics of the power spectrum in 2D electrostatic turbulence?
2. What is the time dependence of the power transfer via three-wave coupling?
3. How does launching waves into the turbulence alter the temporal dynamics of the power spectrum and power transfer?

We will demonstrate that both the wave power spectrum and the energy transfer by three-waave coupling are intermittent, and that this intermittency can be enhanced or reduced by launching waves into the plasma.

Chapter 2 provides an overview of the Collisionless Terella Experiment (CTX) and its plasmas, as well as the diagnostics used to study them. Chapter 3 introduces the spectral analysis techniques used throughout the thesis, and demonstrates their most important features and uses on artificial data. Chapter 4 applies the spectral analysis techniques of Chapter 3 to characterize the intermittency of the floating potential fluctuation power on CTX during the naturally occurring interchange turbulence. Building on this foundation, we then examine how both feedback and driven waves modify the temporal dynamics of the turbulent fluctuations. We will further demonstrate that some of the temporal variations in the power of injected waves can be explained by linear interference effects. In Chapter 5 we explore the intermittency of energy transfer by quadratic wave-wave coupling in interchange turbulence on CTX, and how this energy transfer is modified by feedback or driven waves. Chapter 6 provides a brief summary and a few suggestions for future work which could build on the results in this thesis.

Chapter 2: The Collisionless Terella Experiment

All experiments in this thesis were conducted on the Collisionless Terella Experiment, commonly referred to as CTX [Figure 2.1]. CTX plasmas are confined by a dipole field created by a mechanically supported, water-cooled copper electromagnet inside an aluminum vacuum vessel approximately 1.5 m in length and diameter. These plasmas are unstable to interchange and entropy modes, and under certain conditions continuously exhibit fully developed two-dimensional turbulence [31, 75]. A variety of radially and azimuthally distributed diagnostics allow for spatially and temporally resolved analysis of the turbulent fluctuations.

This chapter covers the design of the CTX device, useful diagnostics, the nature of CTX plasmas, and the feedback/drive system.

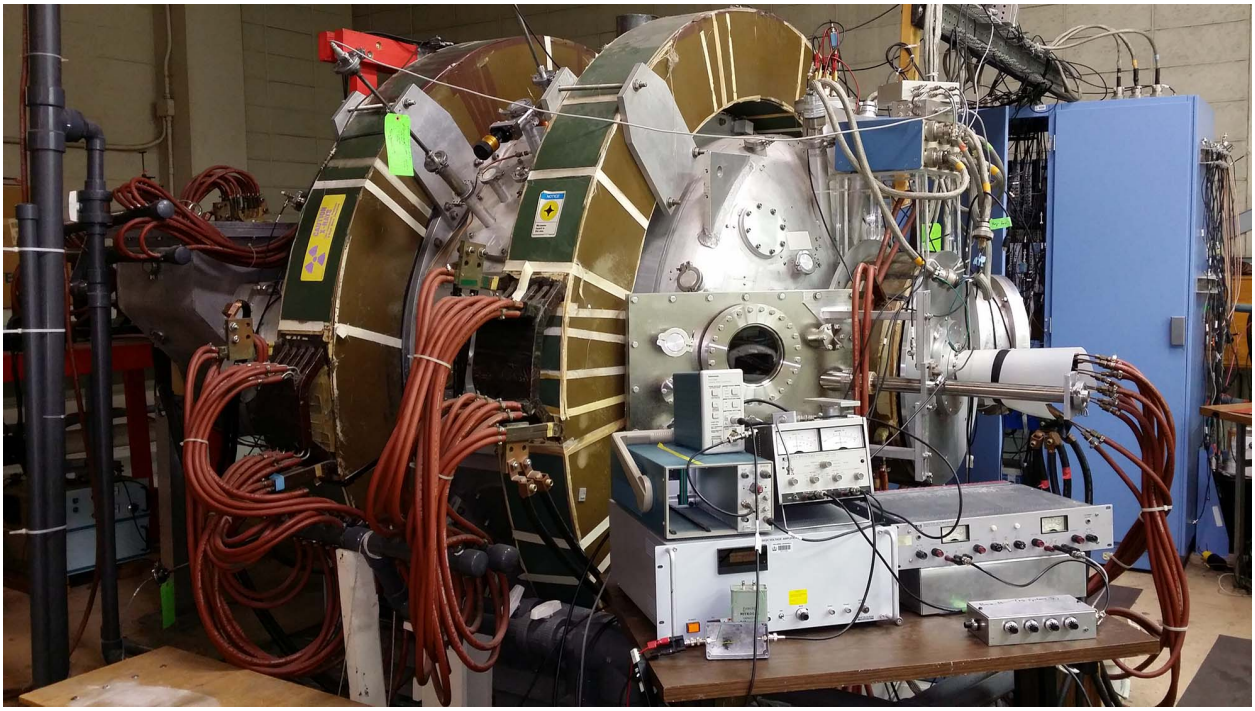

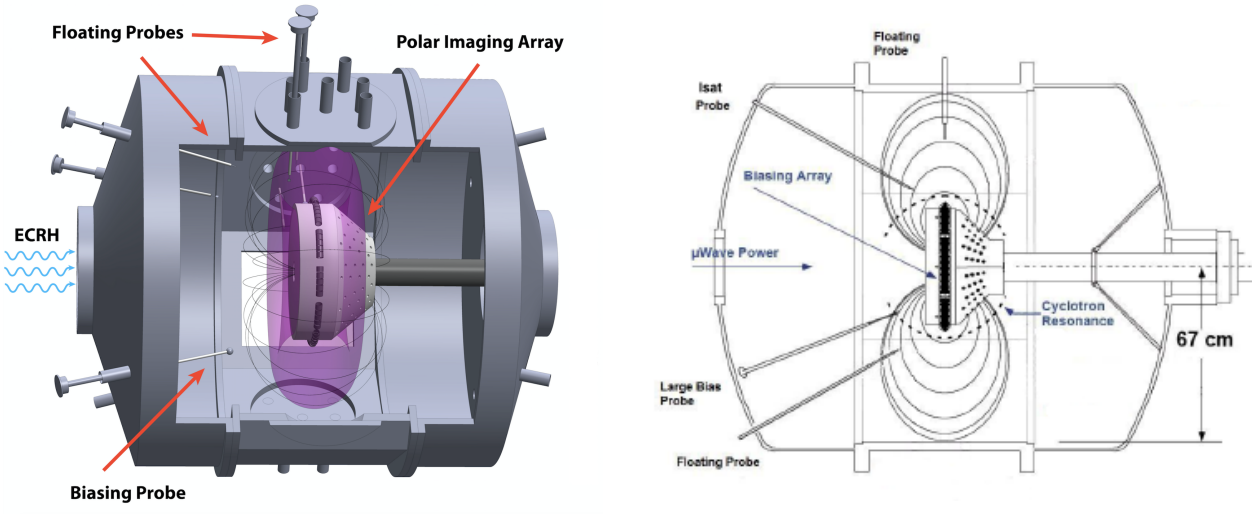

Figure 2.1: a) The CTX device, as seen in the lab. b) 3D rendering of the CTX device highlighting major features. c) Cross-sectional view cut along the dipole axis.

2.1 Generating the CTX Magnetic Field

The dipolar magnetic field of CTX is generated by a mechanically supported copper current-winding composed of six 12x14 coil-pancakes. These pancakes are wound such that all connet-

cions are on the inner edge of the pancakes and are in series [Figure 2.2]. The wires are hollow for water cooling, which is performed in parallel. The winding is housed in an insulating alumina-coated casing to prevent the generation of field aligned currents.

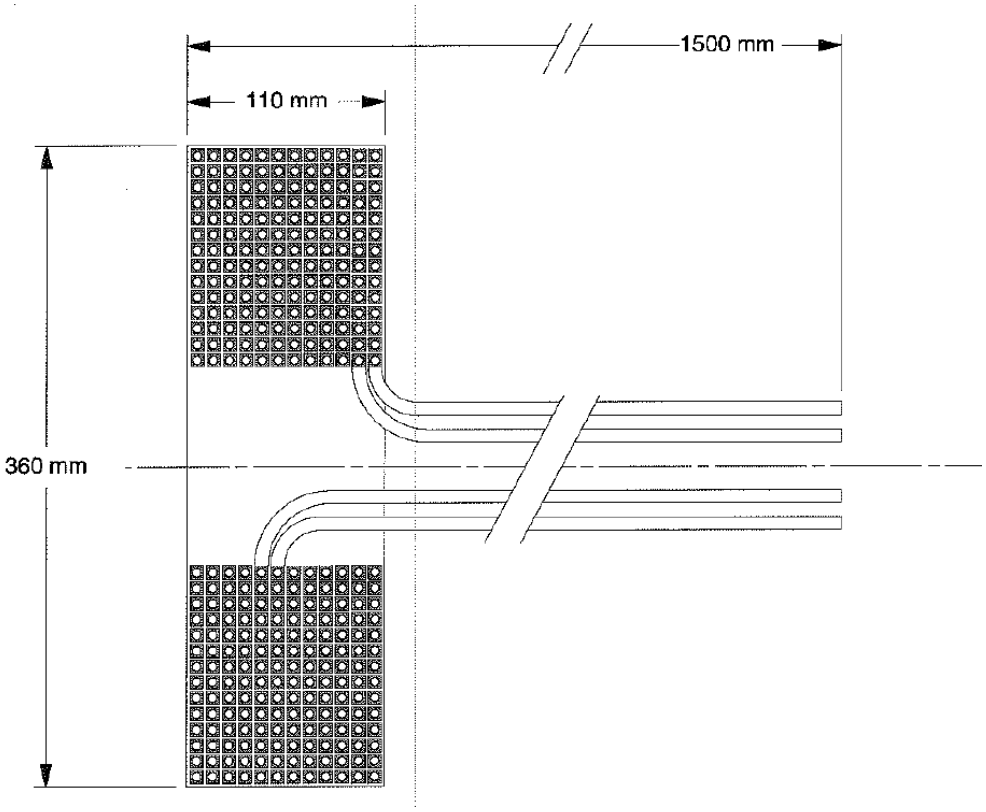

Figure 2.2: Cross-section of the CTX current winding, showing the 12x14 pancake structure of the wires.

The magnetic field in CTX is well appproximated by a point dipole [76] and is modeled as such. At the magnet casing (equatorial radius $L = 21\ cm$) the field is approximately 1500 Gauss, falling off to approximately 50 Gauss at the chamber wall ($L = 67\ cm$).
The magnetic dipole moment can be calculated from

$$\vec{M} = B_0 L_0^3 \hat{z}. \tag{2.1}$$

In CTX, we perform this calculation at the ECRH resonance surface (to be discussed in the next section), where $B_0 \approx 0.0875\ T$ (875 Gauss) and $L_0 \approx 0.27\ m$, giving a dipole moment of $|M| =$

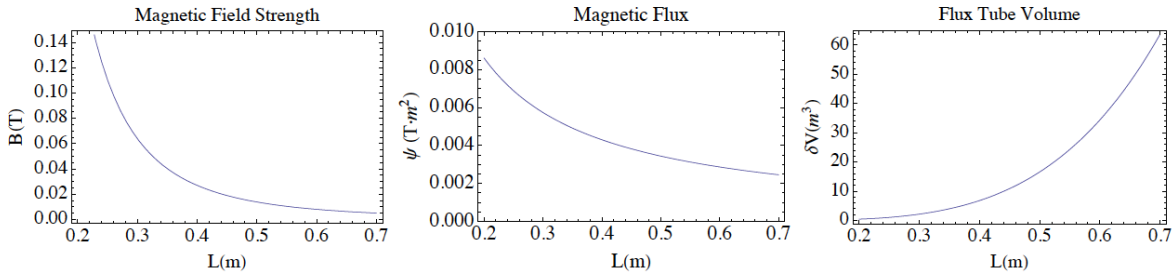

Figure 2.3: Magnetic field strength, magnetic flux, and flux tube volume (per unit flux) as a function of equatorial radius L.

$1.72 \times 10^{-3}\ Tm^3$ and allowing us to write the magnetic field strength at the midplane as

$$|B| = \frac{1.72 \times 10^{-3}}{L^3}. \tag{2.2}$$

Magnetic field strength, magnetic flux, and flux tube volume at the midplane are shown as a function of L in Figure 2.3.

2.2 CTX Plasmas

2.2.1 Plasma Creation: Electron Cyclotron Resonance Heating

To create plasmas in CTX, neutral hydrogen is puffed into the vacuum chamber via a piezoelectrice valve in two or three intervals of a few microseconds to achieve the desired plasma density. At the same time, plane-polarized microwaves at 2.45 GHz are injected into the chamber from a 1.6 kW magnetron through a waveguide system shown in Figure 2.4. The waveguide system measures both the input and reflected microwave power. The microwaves reflect off the chamber walls and pass through the plasma many times; on each pass, some energy from the microwaves is absorbed by electrons whose cyclotron frequency is equal to the microwave input frequency. This resonance occurs at

$$\omega_c = \frac{qB}{2\pi m_e} = 2.45\ GHz \longrightarrow |\vec{B}| = 875\ Gauss; \tag{2.3}$$

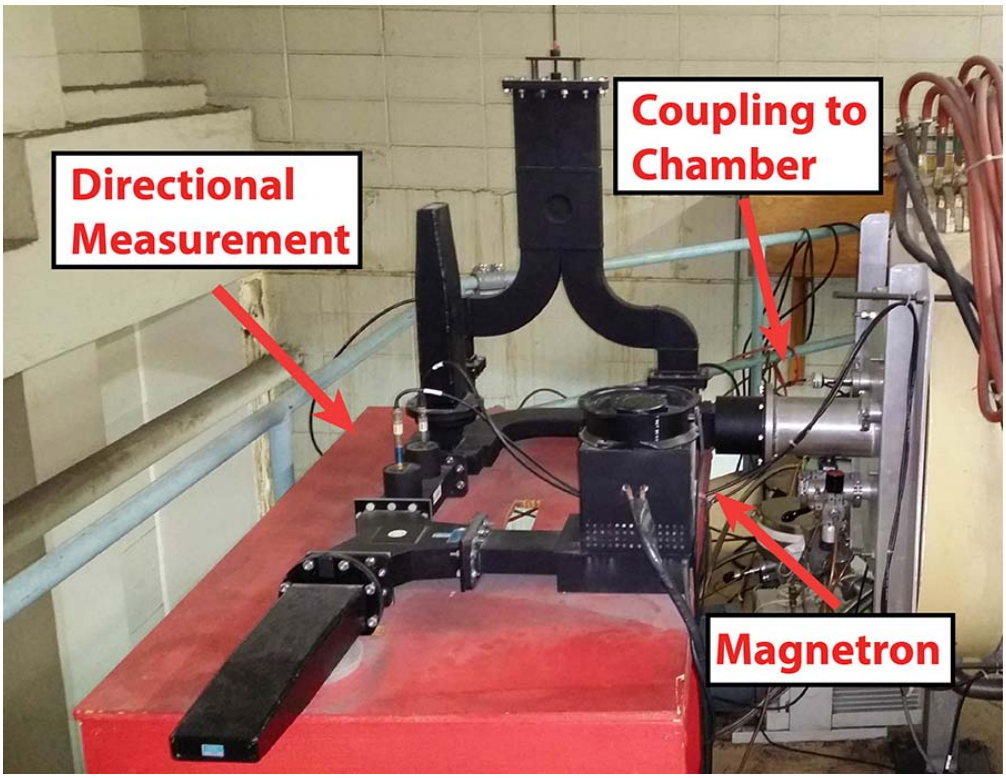

Figure 2.4: Waveguide connecting the magnetron to the CTX vacuum chamber. Input and reflected microwave power are measured by directional antennas.

the surface where this resonance occurs in the plasma can be seen in Figure 1.4. Where this resonance coincides with the device midplane $\left(\theta = \frac{\pi}{2}\right)$, it impacts all trapped electrons on that field line. This creates a region of hot and deeply trapped electrons that form a radial peak in plasma density and temperature, as well as a persistent radial electric field. In CTX, this occurs at $L = 27\ cm$. This region of hot electrons is responsible for the aptly named Hot Electron Interchange Instability [77, 78], which was the focus of early work on CTX [14] as well as other laboratory dipole and mirror experiments [79, 80].

However, the plasma cannot continute to absorb microwaves once it has reached a sufficiently high density. Beginning with the dispersion relation for an electromagnetic wave propagating through an unmagnetized plasma [81],

$$\omega = \sqrt{c^2k^2 + \omega_p^2} = ck\sqrt{1 + \frac{\omega_p^2}{c^2k^2}} \tag{2.4}$$

we can solve for the condition where the wavenumber becomes imaginary and microwaves are reflected by the plasma:

$$n_c = \frac{m_e \epsilon_0 \omega^2}{e^2} \tag{2.5}$$

We see that the critical quantity is the electron plasma frequency, which is determined by the density:

$$\omega_{pe} = \sqrt{\frac{e^2 n}{\epsilon_0 m_e}} \approx 18\pi\sqrt{n} \tag{2.6}$$

For microwaves at 2.45 GHz, we find that the cutoff density is $n_c \approx 7.7 \times 10^{16}\ m^{-3} = 7.7 \times 10^{10}\ cm^{-3}$, which approximates an upper limit on the density of CTX plasmas.

2.3 Turbulence in CTX

Once a low density $\left(n \sim 10^{14}\ m^{-3}\right)$ plasma is created in CTX, a second hydrogen puff can cause a sudden transition to a high density state, approaching the cutoff density $\left(n \sim 7.7 \times 10^{16}\ m^{-3}\right)$. The increase in neutral pressure above $\sim 10^{-5.3}\ Torr$ from the second puff decreases the ratio of hot to cold electrons, stabilizing the hot electron interchange instability [82] and allowing the transition to fully developed turbulence. A number of plasma parameters undergo sharp changes at this transition, as can be seen in Figure 2.5. Most notably, the density increases approximately two orders of magnitude and the electron temperature decreases by an order of magnitude. Average parameter values in the turbulent regime at $L \approx 45\ cm$, where all experiments for this thesis were conducted, are given in Table 2.1.

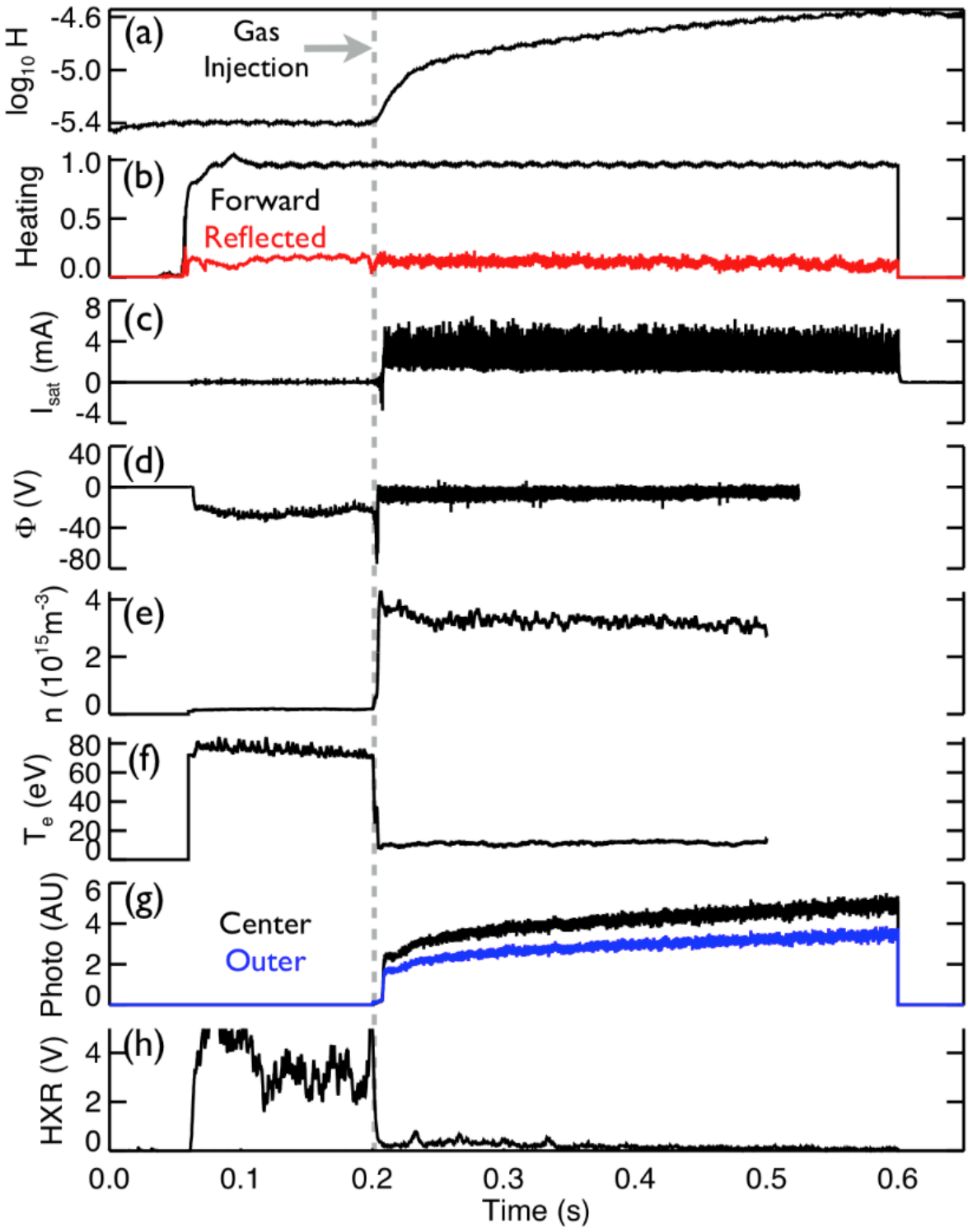

Figure 2.5: Evolution of plasma parameters during a discharge which transitions to the turbulent regime at 0.2 seconds. a) Hydrogen pressure, b) microwave power, c) ion saturation current, d) edge floating potential, e) edge density (smoothed), f) electron temperature (smoothed), g) photodiodes, and h) hard x-ray emission.

Mean Plasma Density	$\bar{n}$	$7 \times 10^{10} cm^{-3}$
Electron Temperature	T_e	25-50 eV
Ion Temperaature	T_i	1 eV
Plasma Beta	β	0.01
Electron Cyclotron Frequency	ω_{ce}	500 MHz
Electron Bounce Frequency	f_{be}	1.5 MHz
Ion Cyclotron Frequency	ω_{ci}	250 kHz
Ion Bounce Frequency	f_{bi}	7 kHz
Drift Frequency	ω_{de}	2-4 kHz
ECR Frequency	f_{μ}	2.45 GHz
B at ECR Resonance	B_0	875 Gauss

Table 2.1: Plasma parameters at L = 45 cm for CTX in the high density, turbulent state.

Once the turbulence has saturated, large amplitude $\left(\frac{\delta n}{n_0} \sim 50\%\right)$ broadband fluctuations in potential and density occur, as can be seen in the floating potential signal in Figure 2.6. The density displays similarly large fluctuations concentrated in the audio range. CTX plasmas are highly reproducible and allow study of sustained plasma turbulence for up to 400 ms per shot, meaning ensemble statistics are well-converged. The spectra of the potential and density fluctuations obey power law scalings characteristic of turbulent cascades, potential as $\sim f^{-5}$ and density as $\sim f^{-3}$ [Figure 2.7].

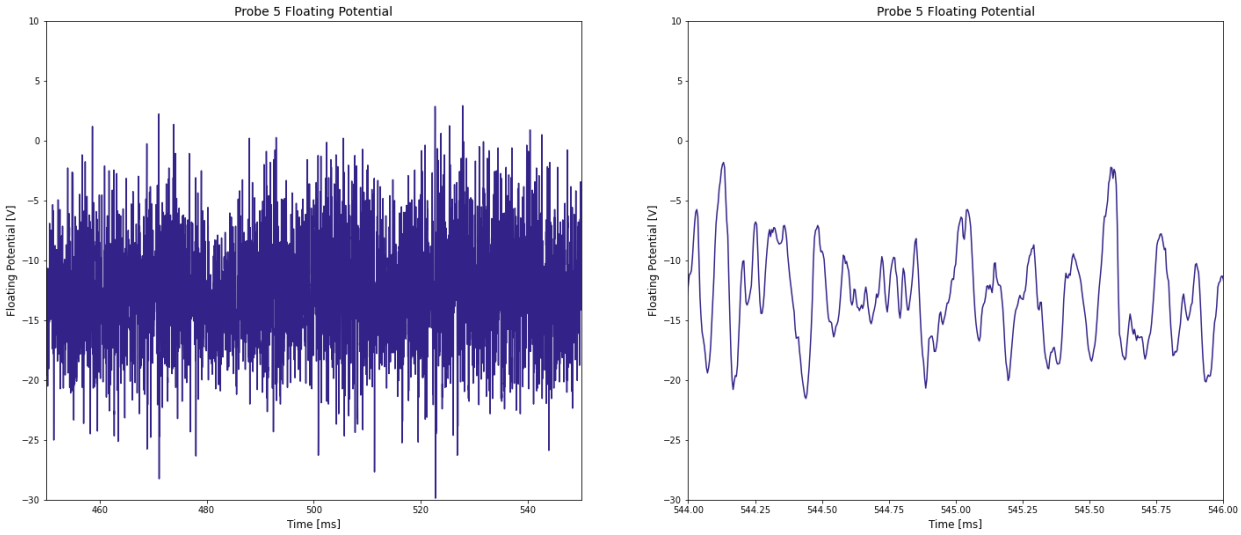

Figure 2.6: a)Sample floating potential measurement over a turbulent 100 ms window; b) same floating potential measurement, zoomed in on a 2 ms window to show detail.

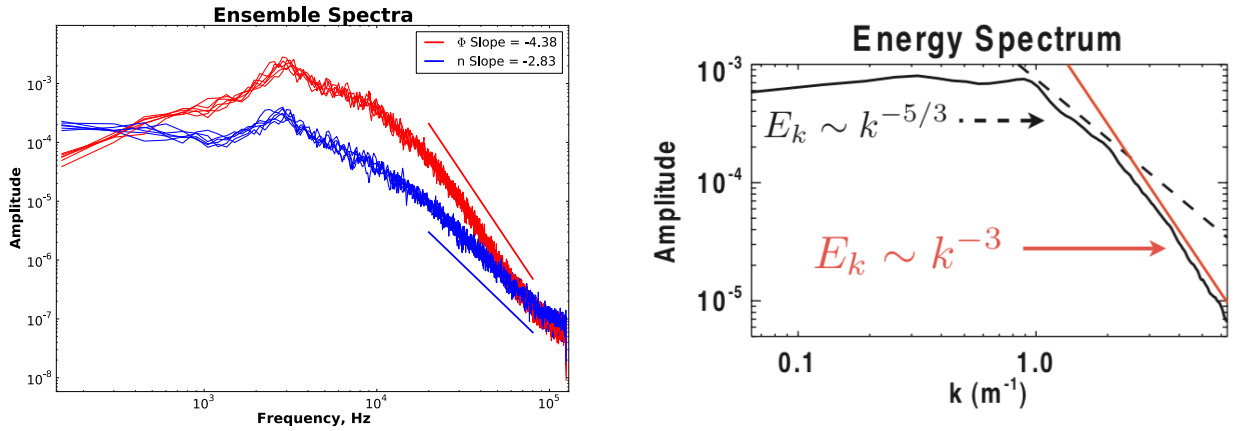

Figure 2.7: a) Power law trends in floating potential (red) and density (blue) consistent with a forward enstrophy cascade. b) Power law trends in energy consistent with an inverse cascade of energy and 2D turbulence.

2.4 Diagnostics

A variety of diagnostics are used on CTX to measure both basic plasma parameters and the specific features of interest, either directly (e.g. Langmuir probes, energy analyzers) or indirectly (e.g. photodiodes, x-ray emission) at a variety of azimuthal and radial locations. Only direct diagnostics are used for the analysis in this work, and will be described this section. Other diagnostics are described in [75]. All diagnostic data is digitized and recorded at 250 kHz on Jorway A14 transient recorders.

2.4.1 Floating Potential Probes

CTX is equipped with five radially adjustable floating potential probes, each at a different azimuthal location (somewhat determined by restricted port access). Each probe consists of a stainless steel wire tip and a 100 $k\Omega$ resistor, with the resistor and and coaxial connections housed inside a $12in$ alumina shaft, connected to a stainless steel shaft exiting the vacuum chamber via a KF-40 sliding feedthrough. These probes are the primary diagnostic for the experiments in this work, and some serve as sensors for the feedback experiments. Typical floating potential fluctuations are on the order of 3 V RMS, significantly larger than the diagnostic noise level of

0.01 V RMS. The noise level is the same with both the magnet and microwave power supplies off (gas puff on), microwaves and gas puff on (magnet off), or magnet and gas puff on (microwaves off).

2.4.2 Bias Probes

Two 1 in diameter biasable probes are positioned 90° apart azimuthally, well off the midplane to minimize the perturbation to the plasma. The spherical collecting area of each is roughly 20 cm^2. The design is similar to that of the floating potential probes described in Section 2.4.1, with the exception of the conducting tip, and can be seen in Figure 2.8. One of these probes will be used as the actuator in the feedback experiments, and both will be used to drive waves at specific frequencies during driven experiments.

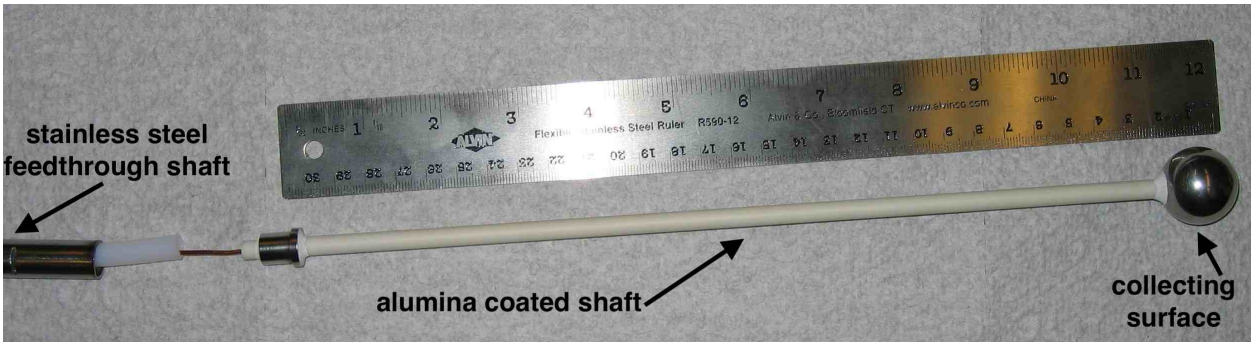

Figure 2.8: Bias probe partially disassembled on the bench, with components labelled.

The azimuthal locations of the bias and floating probes can be seen in Figure 2.9, and an idea of their 3D positioning can be gleaned from Figure 1.1 b).

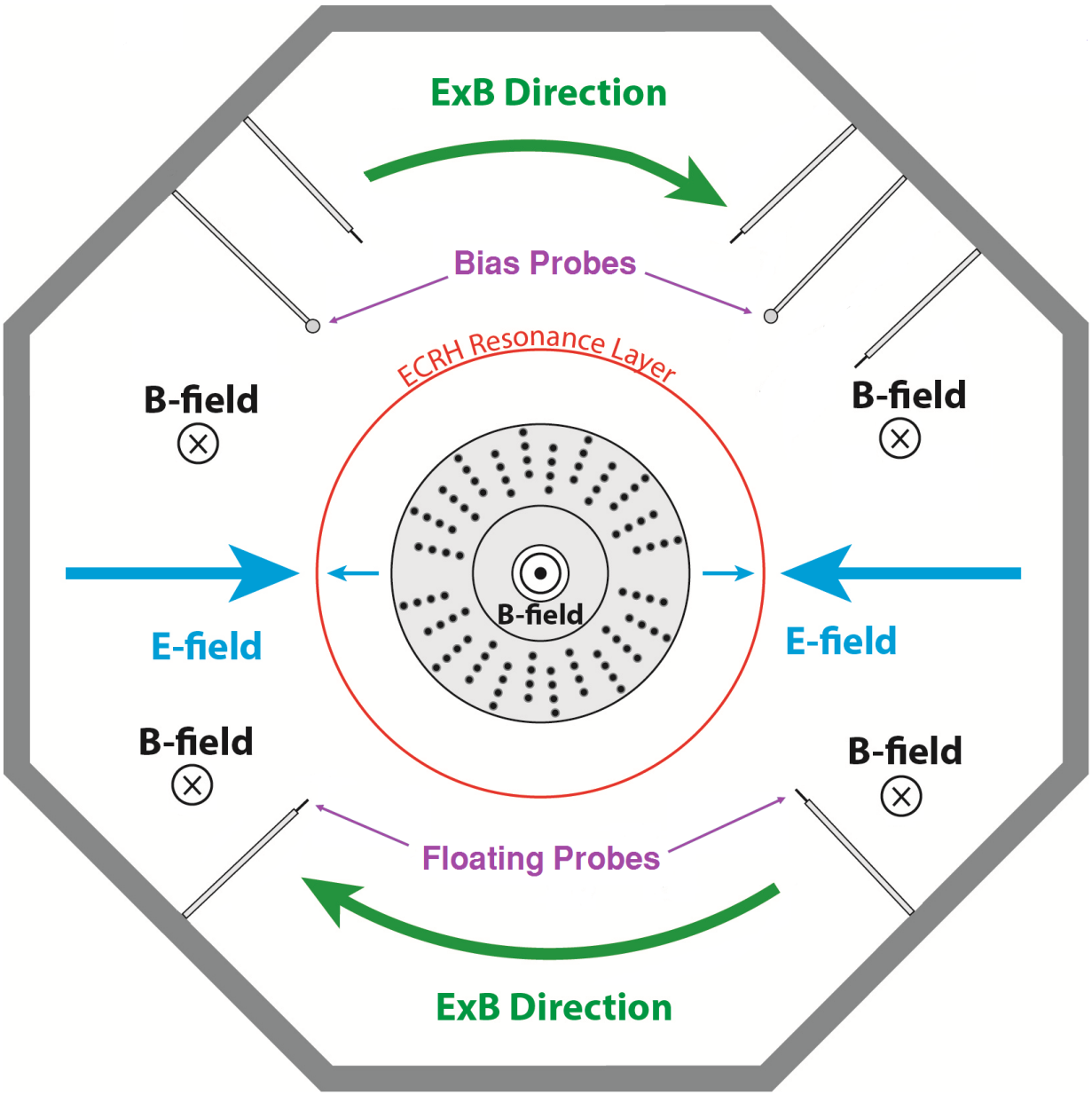

Figure 2.9: View of CTX along the axis of the mechanical support showing all diagnostics used in this work, as well as a few major plasma features.

2.4.3 Langmuir Probe

The Langmuir probe consists of a 1 cm^2 square conducting plate, and is constructed similarly to the bias and floating probes of the previous subsections. For all experiments in this work the probe is biased to $-180\ V$ to collect ion saturation current $\left(-180\ V \gg \frac{T_e}{e}\right)$. The bias is provided

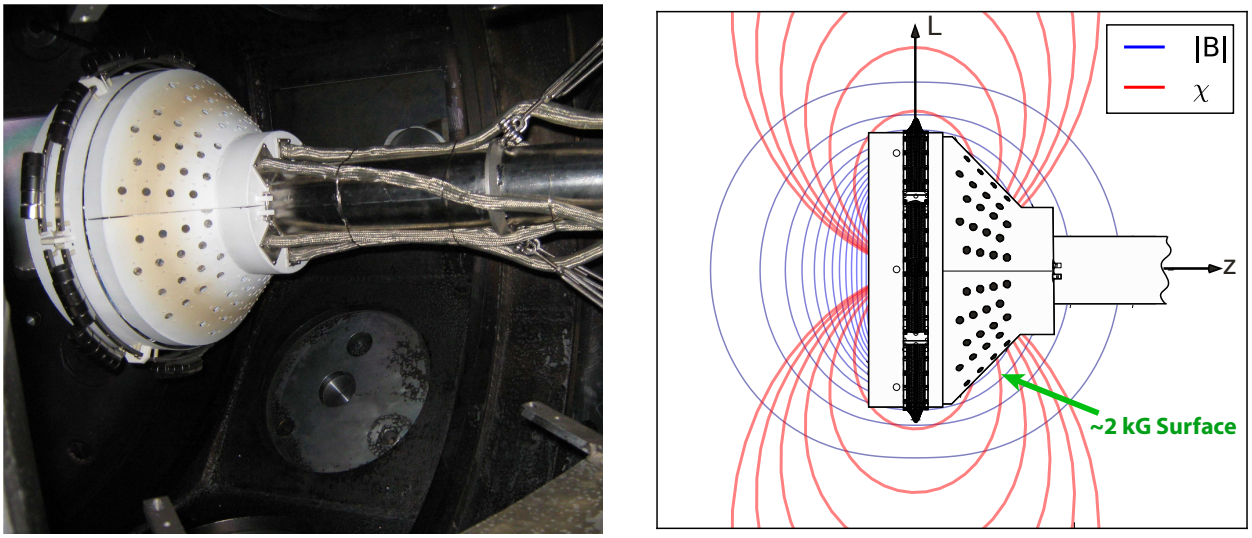

Figure 2.10: Photograph of the Polar Imager and magnet casing inside the CTX vacuum chamber (left) and a rendering of the Polar Imager (right) showing the magnetic field lines (red) and surfaces of constant magnetic field strength (blue). The $2\ kG$ surface is labelled; note the proximity of the particle detectors to this surface.

by a battery in parallel with a 0.1 μF capacitor to improve the high frequency response.

2.4.4 Polar Imaging Array

The Polar Imaging Array, or Polar Imager, is positioned on one of the poles of the magnet housing and serves as a plasma imaging diagnostic. It is made up of 96 gridded particle detectors providing measurements of plasma parameters at 12 azimuthal locations on 8 radii. All detectors are on or close to the $B \approx 2\ kG$ surface to ensure particles entering each detector have the same gyro radius, as can be seen in Figure 2.10.

Holes in the magnet housing allow ambipolar flow of plasma to the particle detectors inside. Each detector consists of three individually biased stainless steel meshes in front of a collection plate; the biases on each of these meshes can be tuned to select for particle species and energy (Figure 2.11), allowing a mapping of the plasma phase space. The first grid is biased to repel electrons, the second is biased to repel ions, and the third is always biased to $-9\ V$ to suppress secondary electron emission from the collection plate. For all experiments in this work, the particle detectors are set to collect flux-tube integrated ion saturation current, allowing the calculation

of the plasma density at each location. Over time some detectors failed, and their locations are interpolated over in any analysis.A more detailed description of this diagnostic, including a detailed digitizing map, can be found in Appendix D of [29] and [76].

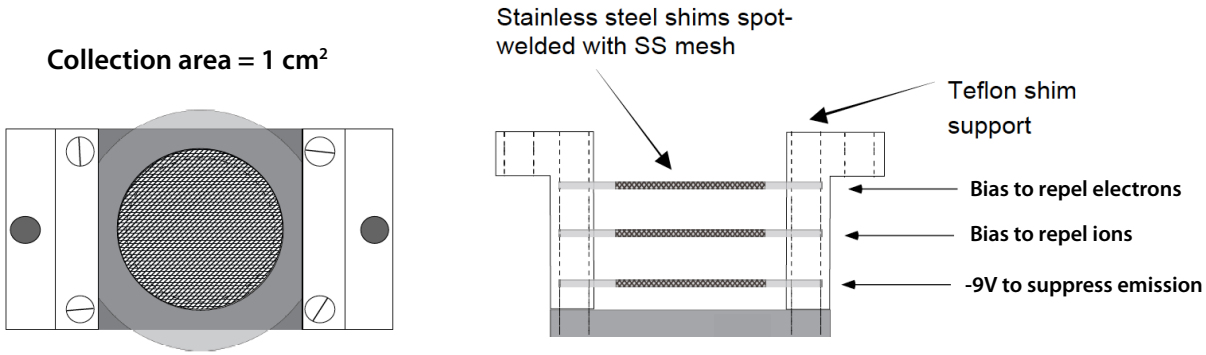

Figure 2.11: Top and side views of the particle detectors comprising the Polar Imager.

2.5 Feedback/Drive System

All experiments in this thesis use one or two identical electrostatic feedback/drive systems to modify the naturally occuring turbulent dynamics. There are three fundamental parts to any feedback system: the sensor, actuator, and feedback circuit connecting the two. On CTX, any of the five floating potential probes can be used as the sensor, and either bias probe can be used as the actuator. Throughout this work, we will use "upstream" and "downstream" directions to refer to the location of sensors relative to actuators and the direction of mode rotation. An example configuration including this directional convention can be seen in Figure 2.12. A detailed description of the feedback circuit can be found in Chapter 3 of [29].

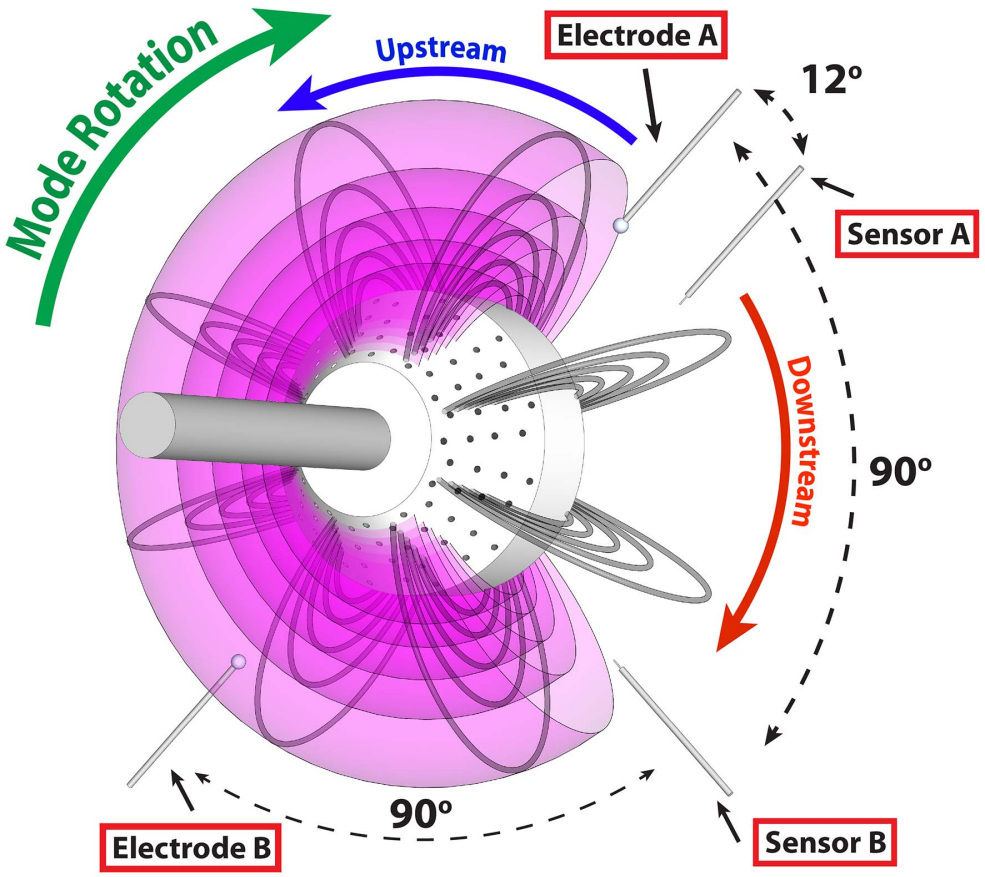

Figure 2.12: 3D rendering of CTX plasma showing the direction of mode rotation and the upstream/downstream directional convention for sensor/actuator pairs. Sensors A is 12° downstream of electrode A, while sensor B is 90° upstream of electrode B.

2.6 Summary

The Collisionless Terrella Experiment (CTX) is the first laboratory device to explore the dynamics of relatively high-temperature plasma confined by a large, high-field dipole magnet. CTX operates with long pulses. When he neutral gas density is low, energetic electrons excited to quasi-relativistic energies by microwave heating. When the neutral gas pressure increases, the plasma makes a spontaneous transition to a higher density plasma with warm electrons that exhibits continuous, fully-developed two-dimensional electrostatic turbulence. Interchange and entropy modes cause plasma transport and exhibit nonlinear chaotic behavior.

The results from the CTX experiment guided the design and operation of the Levitated Dipole

Experiment (LDX) and the superconducting ring-trap device (RT-1) at the University of Tokyo, as discussed in Chapter 1. These devices also showed spontaneous transitions from a low-density plasma dominated by energetic trapped electrons to a plasma with higher density and warm electrons dominated by interchange and entropy mode turbulence.

The research presented in this thesis focuses on high density plasmas exhibiting fully developed turbulence on CTX. These plasmas have large relative fluctuations of potential and density and exhibit a wide spectral cascade resulting from wave-wave coupling. A biasable electrode is inserted into the plasma that can launch coherent electostatic waves and apply active feedback to explore how active wave excitation modifies plasma turbulent dynamics.

Chapter 3: Spectral Analysis Techniques

The analysis in this thesis focuses on characterizing temporal changes in the frequency content of the turbulent spectrum on the CTX device. This chapter introduces the primary analysis techniques, their relationship to each other, and their respective strengths and weaknesses when analyzing data. Our work with these methods has benefitted greatly from the excellent review of wavelet transforms by Torrence & Compo [3] and their extension to higher order spectral quantities by van Milligen et al [83], as well as the helpful review of applications to space plasma processes by de Wit and co-authors [84].

To demonstrate features of the techniques outlined in this chapter, we'll apply them to an artificially generated test time series. This test will consist of the superposition of four sinusoids at 2, 3.2, 4.2, and 5.2 kHz, where the 2, 3.2, and 5 kHz waves are phase coupled and all sinusoids have up to $\pm 30^{\circ}$ of random phase noise (Figure 3.1). All of these techniques assume that we are analyzing a time series with measurements taken at regular intervals. To be consistent with experiments, all measurements are made at a sampling frequency of 250 kHz, and we study a 100 ms time window during which the mean background plasma parameters are constant and the signals are ergodic.

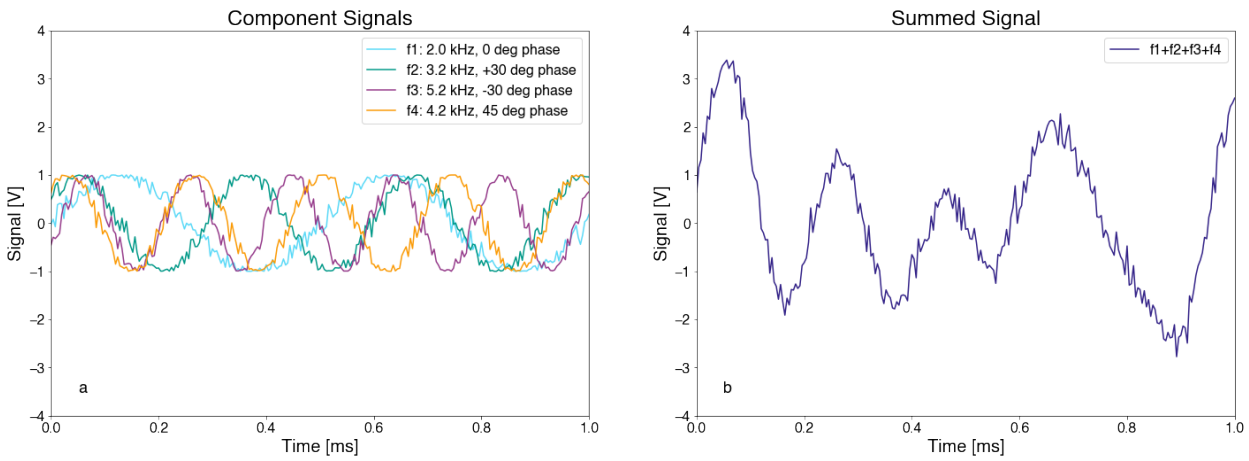

Figure 3.1: Test data at 2, 3.2, 4.2, and 5.2 kHz with ±30° of random phase noise (a), and their sum (b).

This chapter begins by introducing the initial signal processing (Section 3.1) before moving on to spectral analysis. We'll review Fourier-based, time-averaged techniques first (Sections 3.2 and 3.3) before introducing time resolution via the continuous wavelet transform (Section 3.4) and extending the higher-order spectra of Section 3.3 to the wavelet domain in Section 3.5. Section 3.6 provides an introduction to some of the mathematical techniques used to diagnose intermittency.

3.1 Initial Signal Processing

To extract frequency information from a signal we conduct the Fourier transform (see Section 3.1.2) over a segment of length T in a time series, which returns evenly spaced frequencies from 0 to the Nyquist frequency f_N (one half the sampling frequency, or 125 kHz for this work). The number of frequencies will be equal to the number of samples used in the transform - a longer time window allows both a lower minimum frequency T^{-1} and higher frequency resolution, as more frequencies are used to span the range $[0, f_N]$. However, when calculating ensemble averaged quantities from a single time series, it is necessary to divide T into a number of sub-intervals K and conduct the Fourier transform of each sub-interval. The exact value of K required for ensemble averaged quantities to converge depends on the quantities being calculated; for this work we require $K \geq 30$ [85].

For the K sub-intervals, each of length M, the mean is calculated and subtracted from each point to remove the DC component of the signal, as we are only interested in the fluctuations about that mean. This subtraction also makes statistical quantities constructed from the Fourier transforms of these windows easier to analyze, as the DC component can be orders of magnitude larger than any fluctuations. Note that it will be the length M of these segments that sets the resolution of the Fourier spectrum. There is also a tradeoff between the length of the segments and the number of segments contained in a time T, resulting in a tradeoff between frequency resolution and statistical convergence. We choose $M = 1000$ samples (4 milliseconds) to minimize window length (and thus maximize the number of windows K) while retaining all major features of the Fourier spectrum.

Applying a windowing function to each sub-segment of the data and padding that subsegment can further increase our frequency resolution without sacrificing statistical convergence. We choose the Bartlett Triangular Window as our window function because it has less spectral leakage than a simple rectangular window, smooths out discontinuities at the beginning and end of the window, and preserves signal amplitude when windows have a 50% overlap [86]. Overlapping sub-segments in this manner nearly doubles the number of segments K without sacrificing frequency resolution by making shorter windows. To further increase frequency resolution, we pad the windowed segment of data with zeros on either end. This increases the number of samples fed into the Fourier transform, which increases spectral resolution. Choosing the pad size is a trade off between computational time and frequency resolution, though above some pad size the major features of the spectrum will have been resolved and further increase does not add to the analysis.

For this work, we use 4 ms windows with 50% overlap, each symmetrically padded by 4 ms of zeros. An example of such a window and how it is padded is shown in Figure 3.2. Note that if we were to sum all segments (after windowing and padding), we would perfectly recreate the original signal everywhere except the first and last segments, which would each retain one side of the triangular window. All signal processing discussed in this section is conducted prior to the FFT for each segment, following the Welch method [87] of subdividing the signal into sub-intervals with 50% overlap, then windowing each sub-interval.

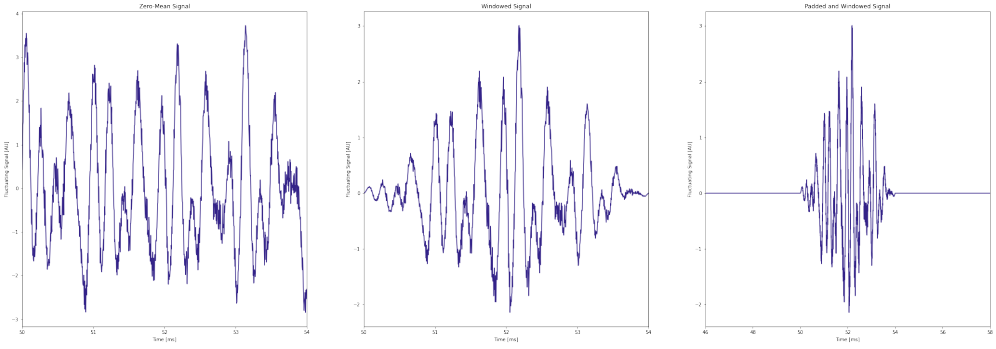

Figure 3.2: a) 4 ms window of zero-mean data, b) with window function applied, and c) with padding.

3.2 The Fourier Transform & Power Spectrum

The Fourier transform of a time series $x(t)$ transforms the data from the time domain to the frequency domain - the signal is broken down as a sum of periodic components, rather than as its amplitude at each time. Studying the Fourier transform of a signal can offer insight into the periodicity of that signal and aid in understanding the process generating it. Because data analysis is being conducted using Python, we use their unitary Fast Fourier Transform (FFT), which is a version of the Discrete Fourier Transform (DFT)

$$X(f_q) = \frac{1}{\sqrt{M}} \sum_{p=0}^{M-1} x(t_p) e^{-i2\pi pq/M} \tag{3.1}$$

The Fourier transform of a time series is a complex quantity containing both amplitude and phase information. Because the basis functions of the Fourier transform are complex exponentials (essentially sines and cosines), any time localization is lost after a Fourier transform. This means that it is not possible to observe most transient fluctuations using Fourier techniques alone, though some can be captured by a spectrogram (a consecutive series of windowed Fourier transforms). Such transient fluctuations are essential when studying intermittency, so this lack of time resolution will be addressed in Section 3.3.

In this work we will focus on the power contained in fluctuations, rather than the fluctuations

themselves. To do this we use the power spectrum, a quantity which is second order in the Fourier transform:

$$P(f) = \langle X(f) - X(-f) \rangle = \langle X(f)X^*(f) \rangle = \langle |X(f)|^2 \rangle, \tag{3.2}$$

where $\langle \alpha \rangle$ denotes the expectation value and α^* denotes complex conjugation. We can think of the power spectrum as the distribution of the signal across the frequency channels of our Fourier transform. To estimate the power spectrum of a time series we use the techniques outlined in Section 3.1.1, compute the FFT and power spectrum of each segment, then create an ensemble averaged power spectrum

$$\hat{P}(f) = \frac{1}{K} \sum_{j=0}^{K-1} \hat{P}_j(f) = \frac{1}{K} \sum_{j=0}^{K-1} X_j(f) X_j^*(f) \tag{3.3}$$

where the index j ranges over each of the K signal segments. An example of both the full and ensemble averaged power spectra for the test data is shown in Figure 3.3. Note that the ensemble average spectrum captures the correct peak frequencies, but those peaks are broadened due to the lesser frequency resolution of the shorter sub-intervals (125 Hz vs 5 Hz). Any phase information is lost in the calculation of the power spectrum, which means that the power spectrum (and any other second order quantity) can only fully describe linear processes [85].

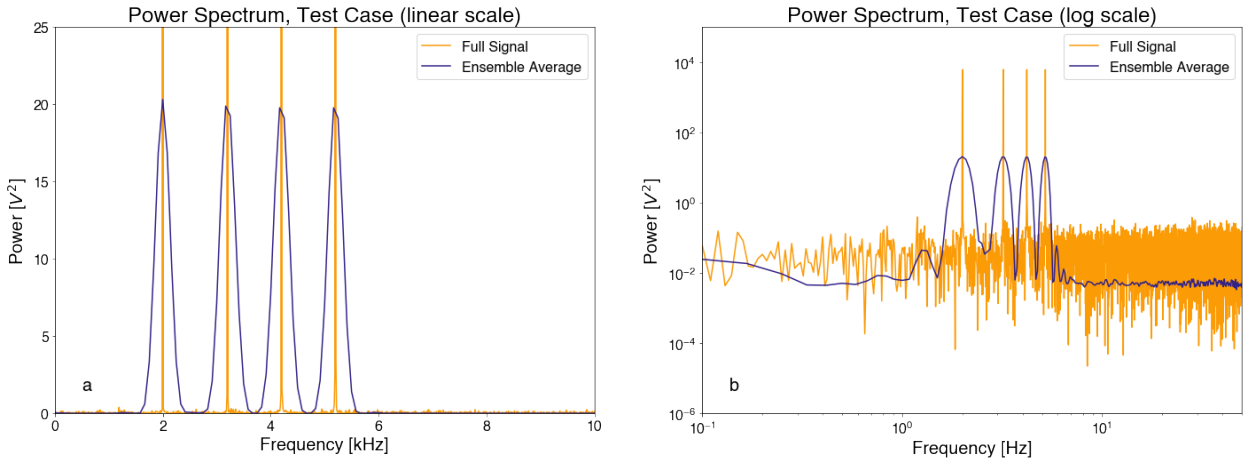

Figure 3.3: Power spectrum of the test data, calculated with both the full 100 ms and an ensemble average of 4 ms segments on a linear (left) and logarithmic (right) scale.

3.3 Bispectrum & Bicoherence

Moving beyond the power spectrum, we can construct a similar quantity which is now third-order in the Fourier transform: the bispectrum

$$B(f_1, f_2) = \langle X(f_1)X(f_2)X^*(f_1 + f_2)\rangle. \tag{3.4}$$

Much like with the power spectrum, calculating an estimate of the bispectrum is done by creating an ensemble average from the available data

$$\tilde{B}(f_1, f_2) = \frac{1}{K}\sum_{j=0}^{K-1} B_j(f_1, f_2) = \frac{1}{K}\sum_{j=0}^{K-1} X_j(f_1)X_j(f_2)X_j^*(f_1 + f_2). \tag{3.5}$$

In the limit of sufficiently large segment size (M) and number of segments (K), this ensemble average has been shown to be an approximately unbiased estimate of the true bispectrum [88, 89].

Higher order quantities like the bispectrum allow us to look at deviations from Gaussianity, study the phase characteristics of the signal, and detect and quantify nonlinearities [90]. Because the bispectrum has both magnitude and phase information it can be used to dectect quadratic nonlinearities via three-wave coupling, which occurs when three waves meet both frequency and wavenumber matching conditions

$$f_1 + f_2 = f_3 \tag{3.6}$$

$$k_1 + k_2 = k_3. \tag{3.7}$$

Grierson [75] previous demonstrated that Taylor's approximation holds for CTX plasmas at the frequencies of interest in this work, so the wavenumber matching condition will be met if the frequency matching condition is met. For three-wave coupling to result in net energy transfer, the frequency (and wavenumber) matching condition must be met for a sufficiently long time (and

over a sufficiently large region of space). This leads to a further phase matching condition

$$\phi_1 + \phi_2 = \phi_3. \tag{3.8}$$

When the frequency, wavenumber, and phase matching conditions are (on average) met, fluctuations can nonlinearly exchange energy. Note that the bispectrum is agnostic as to the process generating the nonlinearity.

The bispectrum is typically plotted in the $f_1 - f_2$ plane, as both f_1 and f_2 are independent variables; an example for our four-sinusoid test case is shown in Figure 3.4. Although the bispectrum can be calculated over the full plane, there are a number of symmetries which make much of that information redundant; for example, the choice of which frequency is denoted f_1 and which is denoted f_2 is arbitrary, so the bispectrum will be reflected across the $f_1 = f_2$ line. A discussion of all the symmetries applicable to the bispectrum can be found in [91, 92, 89]. After accounting for these symmetries, we are left with only the primary domain containing non-redundant information. The primary domain of the continuous bispectrum is shown in Figure 3.5. Although we are using a discrete calculation of the bispectrum which has additional symmetries, those symmetries do not affect the frequency range of interest, so the continuous symmetries are sufficient [93]. Using those symmetries, we will only show the principle domain of the bispectrum and bicoherence, as in Figure 3.4.

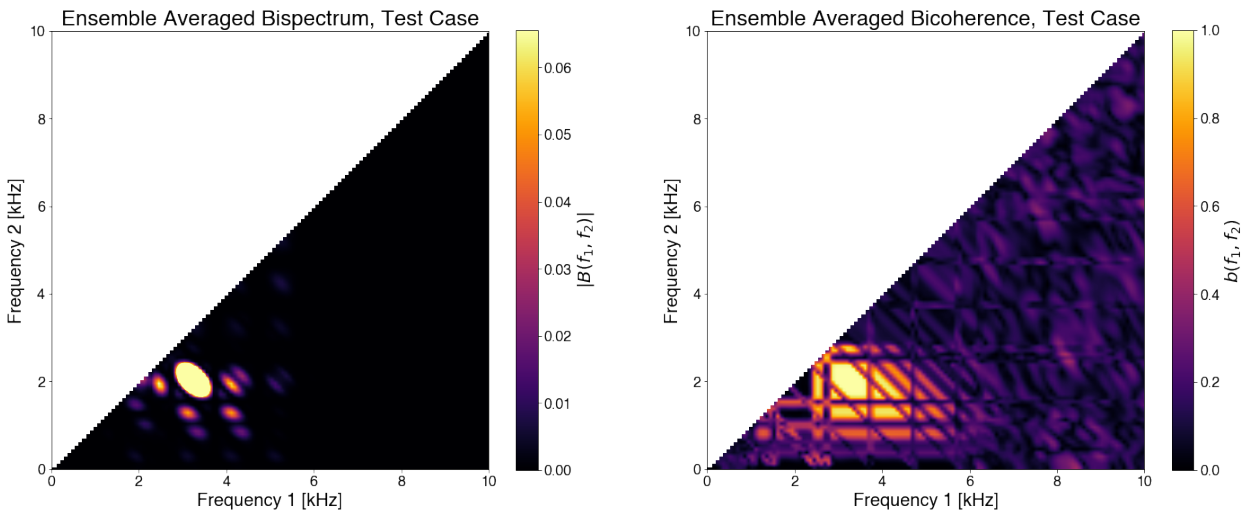

Figure 3.4: Ensemble averaged bispectrum (left) and bicoherence (right) for the test data. Note that the interference patterns around the point of true phase coupling are due to the concentration of power in very few frequencies; this problem does not arise when studying turbulent data.

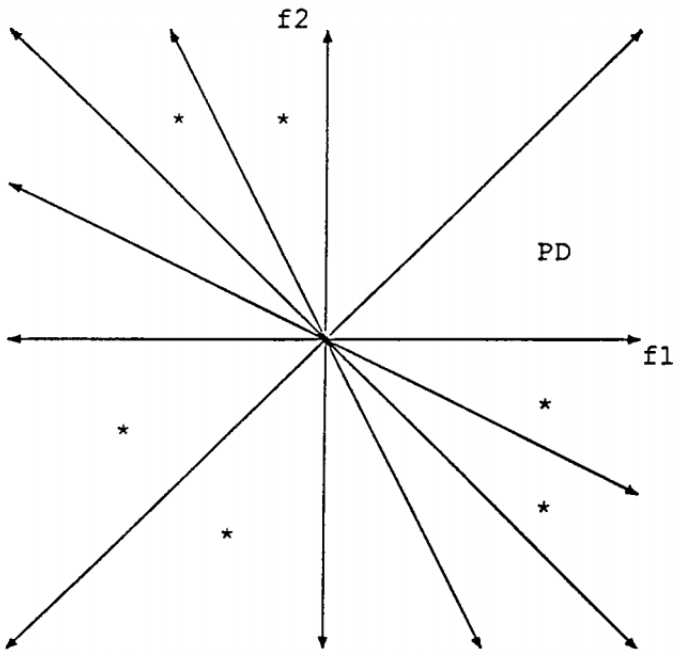

Figure 3.5: The $f_1 - f_2$ plane divided according to the symmetries of the (continuous) bispectrum [93]. PD denotes the primary domain, the region containing all non-redundant information. Regions marked with $*$ require complex conjugation as well as permutation to map back to the principal domain.

The value of the bispectrum $B(f_1, f_2)$ at a point (f_1, f_2) is a measure of the energy transferred

via three-wave coupling from the frequency components at f_1 and f_2 to $f_3 = f_1 + f_2$, and large values are indicative of a nonlinear interaction between fluctuations at those frequencies. This makes the bispectrum a useful tool for diagnosing nonlinearities. However, it is not normalized - sufficient power at a frequency (say f_1) which is not particularly well phase-coupled to f_2 and f_3 can still result in a nontrivial bispectrum simply because $X(f_1)$ is large. To address this, it can be preferable to use the bicoherence b, defined by

$$b^2(f_1, f_2) = \frac{|B(f_1, f_2)|^2}{\langle |X(f_1)X(f_2)|^2 \rangle \langle |X(f_1 + f_2)|^2 \rangle} \tag{3.9}$$

to provide a normalized measure of the quadratic phase coupling present in the system. Just as with the bispectrum, the true bicoherence must be estimated from a sufficient sample of the data as

$$\tilde{b}^2(f_1, f_2) = \frac{|\frac{1}{K}\sum_{j=0}^{K-1} X_j(f_1)X_j(f_2)X_j^*(f_1 + f_2)|^2}{\frac{1}{K}\sum_{j=0}^{K-1} |X_j(f_1)X_j(f_2)|^2 \frac{1}{K}\sum_{j=0}^{K-1} |X_j(f_1 + f_2)|^2}. \tag{3.10}$$

The bicoherence is typically shown in the same f_1-f_2 plane as the bispectrum, but is restricted to values between 0 and 1, with 0 meaning there is absolutely no phase coupling between a given triad of fluctuations and 1 meaning there is perfect phase coupling between those fluctuations. It is important to note that sometimes a number of small peaks may appear in the bicoherence due to the denominator being extraordinarily small; these peaks may obscure the couplings of greatest interest. A variety of solutions have been proposed [85], each with their own pros and cons. We have found that visual interpretation of the bicoherence is often aided in these situations by switching to a logarithmic scale for the bispectrum, without raising any of the issues of the other methods.

The bispectrum and bicoherence have a number of useful properties:

1. The bispectrum is blind to additive Gaussian noise (though the bicoherence is not).

2. A linear filter does not change the bicoherence of a signal.

3. The bicoherence will have peaks if there is quadratic phase coupling in a signal, meaning the

conditions of Equation 3.8 are met.

Property 1 means that Gaussian noise present in the system will not alter the resulting bispectrum, while Property 2 means that any linear effects in the system will not impact the bicoherence. These are helpful because we do not want our results to be influenced by noise or linear processes, as we are only interested in nonlinear interactions. We will rely in particular on Property 3 to study the quadratic phase coupling present on CTX, indicative of a nonlinear generating mechanism.

It is important to note that while the bispectrum and bicoherence can detect the presence and strength of three-wave coupling, neither can tell us how much energy actually moves through that coupling. Creating a detailed energy budget for the system requires the calculation of nonlinear coupling coefficients, which is beyond the scope of this work.

A more in depth discussion of the mathematical details of calculating the bispectrum and bicoherence from a time series can be found in Choudhury [85] Chapters 2, 3, 5, and 6.

3.4 Continuous Wavelet Transform

Although Fourier-based techniques are quite useful for resolving the average spectral properties of a signal, they are severely limited in resolving rapdily changing temporal dynamics. In contrast, wavelet transforms can be used to analyze time series with nonstationary power at a variety of frequencies [94, 95, 96, 97]. Wavelet transforms use basis functions with effective compact support in both time and frequency space to maintain temporal resolution while conducting spectral analysis. This means the non-zero part of the function is finite and localized. The complex exponentials used in the Fourier transform lack this compactness of support because they are unbounded in time.

There a number of distinct types of wavelet transforms, most prominently the continuous and discrete transforms. The continuous wavelet transform is better suited for data analysis, as it is more legible than the discrete wavelet transform (which is better suited for data compression or modeling) [98]. Note that the pre-processing of the time series covered in Section 3.1 is not necessary when using wavelet transforms.

Not just any function can be used as a wavelet, regardless of which wavelet transform is used.

To be admissible as a wavelet, a function must have zero mean and be localized in both time and frequency space [98, 83]:

$$\int_{-\infty}^{\infty} |X(\psi(\omega))|^2 |\omega|^{-1} d\omega < \infty. \tag{3.11}$$

As an example, the complex exponentials used in the Fourier transform fail this test because they are not localized in time. This work will use the Morlet wavelet as the "parent" wavelet, which determines the shape and structure of the wavelet "family." A Morlet wavelet takes the form of a plane wave modulated by a Gaussian (Figure 3.6).

$$\psi_0\left(\frac{t}{a}\right) = \pi^{-1/4} e^{i\omega_0 \frac{t}{a}} e^{-\frac{t^2}{2a^2 d^2}} \tag{3.12}$$

where d is a parameter which determines the exponential decay of the wavelet and ω_0 is a nondimensional frequency which determines the number of oscillations in the parent Morlet wavelet. We take ω_0 to be 6 in order to meet the admissibility condition [98], which also has the convenient property that the wavelet frequecy and equivalent Fourier frequency are approximately equal [3]. The frequency resolution can be approximated as $\Delta\omega = \omega/4d$ and the time resolution as $\Delta t = ad$ [83]. We take $d = 1$ in this work, as this is a common choice which makes a reasonable compromise between time and frequency resolution.

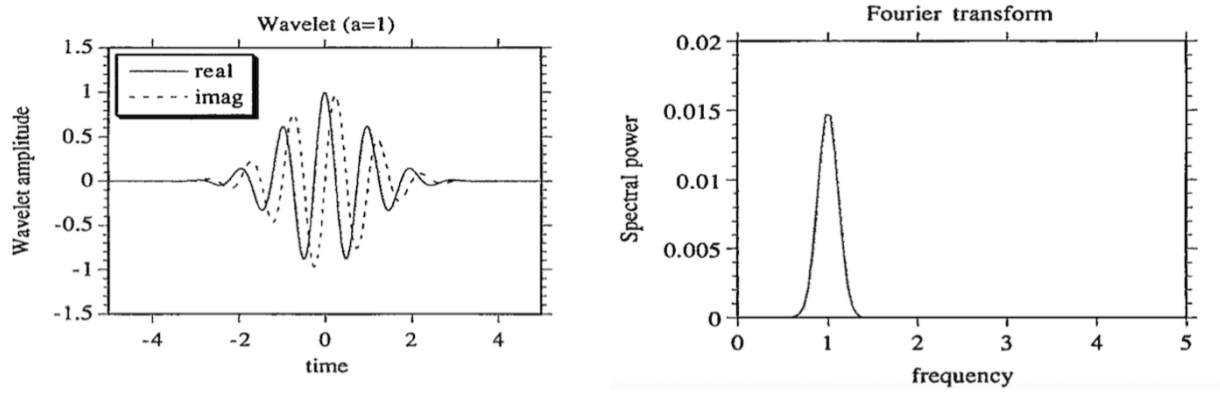

Figure 3.6: An example of a Morlet wavelet with $\omega_0 = 6$ in both the time domain (left) and frequency domain (right).

A corresponding wavelet family can now be constructed from the parent Morlet wavelet (Equa-

tion 3.12) by translating the function in time by some amount τ and scaling the function in frequency space using the scale length a, which is inversely proportional to the frequency of the wavelet

$$\psi_a(t-\tau) = \frac{1}{a^p}\psi\left(\frac{t-\tau}{a}\right). \tag{3.13}$$

Here p denotes the choice of normalization; $p = 1/2$ is used throughout this work, as it makes the L^2 norm independent of a and makes interpretation of the wavelet power spectrum, bispectrum, and bicoherence easier [83, 98, 3]. The continuous wavelet transform of a function $x(t)$ is then

$$W_f(a,\tau) = \int x(t)\psi_a(t-\tau)dt, \tag{3.14}$$

which can be interpreted as a version of f(t) that has been bandpassed by, or convolved with, the filter ψ_a. Writing the wavelet transform for a discrete time series with N points becomes

$$W(a,t) = \sum_{\tau=0}^{N-1} x(\tau)\psi\left(\frac{(t-\tau)\delta t}{a}\right) \tag{3.15}$$

Note that when using the continuous wavelet transform (Equation 3.14) with linearly spaced frequencies, the family of wavelets are not mutually orthogonal. This lack of orthogonality will not substantially impact results presented in this work, but is important for things like reconstructing a time series from the wavelet transform and setting a statistical noise floor [83, 3]. Additionally, if we wanted to impose orthogonality, we would have to restrict the scales used to $a \in \{2^n\}$, which is not the most useful set of scales when examining a (relatively) small frequency range. Instead, we use a linearly spaced set of scales with an equivalent frequency spacing of 100 Hz.

Analogously to the Fourier case, we construct a wavelet power spectrum

$$P_W(a) = \int_T W(a,\tau)W^*(a,\tau)\, d\tau. \tag{3.16}$$

Wavelet transforms and power spectra are typically visualized in the (a,t) plane. Varying the scale a and translating in time t constructs a picture showing the amplitude of fluctuations at different

scales and how those amplitudes vary in time. Importantly for this work, the wavelet transform conserves energy [98]. Note that the work in this thesis focuses on frequencies rather than scale lengths, so calculations will be made and shown in terms of f instead of a. Figure 3.7 provides an example of a wavelet transform for our test data.

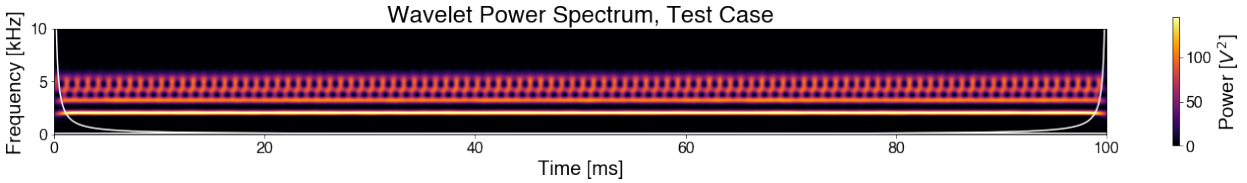

Figure 3.7: Wavelet power spectrum for our test data.

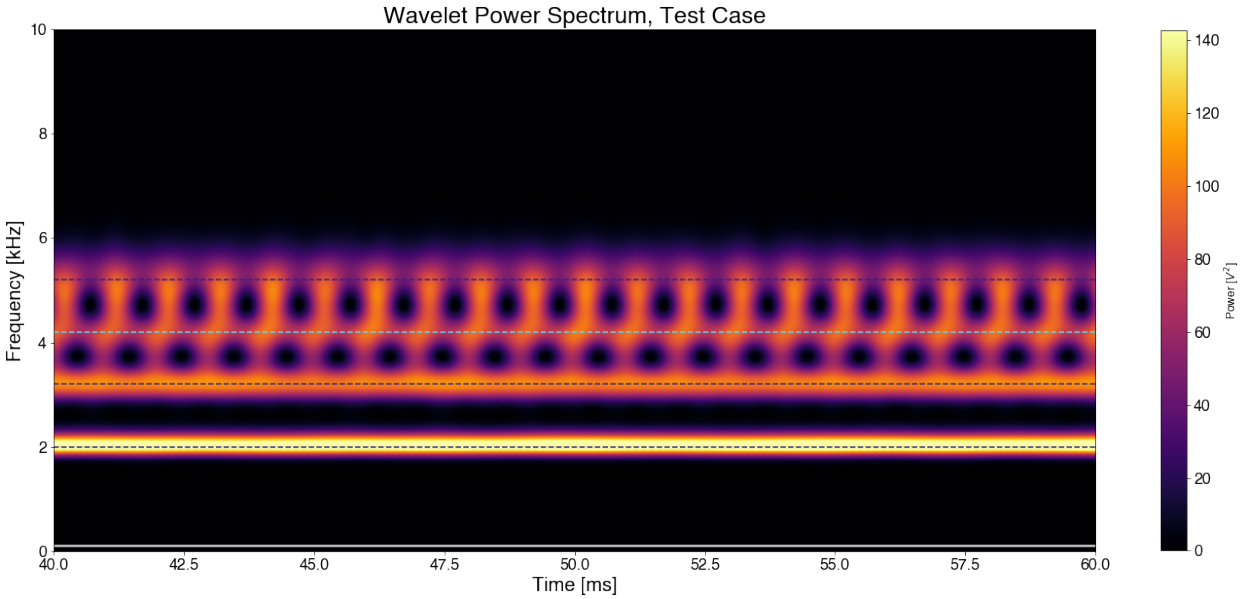

Figure 3.8: Zooming in on the 40-60 ms window of the wavelet power spectrum for our test data. Dark blue lines mark the 3 coupled frequencies (2, 3.2, and 5.2 kHz), while the cyan line marks the uncoupled frequency (4.2 kHz).

Although seeing all 100 ms can be useful, it can be hard to see details. Figure 3.8 zooms in on the 40-60 ms window. The nearly vertical lines which appear periodically between 4.2 and 5.2 kHz (and less intensely between 3.2 and 4.2 kHz) appear because these frequencies are somewhat close together, and their superposition can look like the superposition of fluctuations with power at many intermediate frequencies under a wavelet transform. Figure 3.9 shows examples of two

different frequency spacings and how they show up in a wavelet power spectrum. Frequency spacings greater than a factor of ~ 1.4 allow the frequencies to be resolved separately while closer spacings create this ambiguity. Note that the frequency at which the lines appear (1 kHz in Figure 3.8 and 300 Hz in Figure 3.9) is precisely the difference between the two close frequencies.

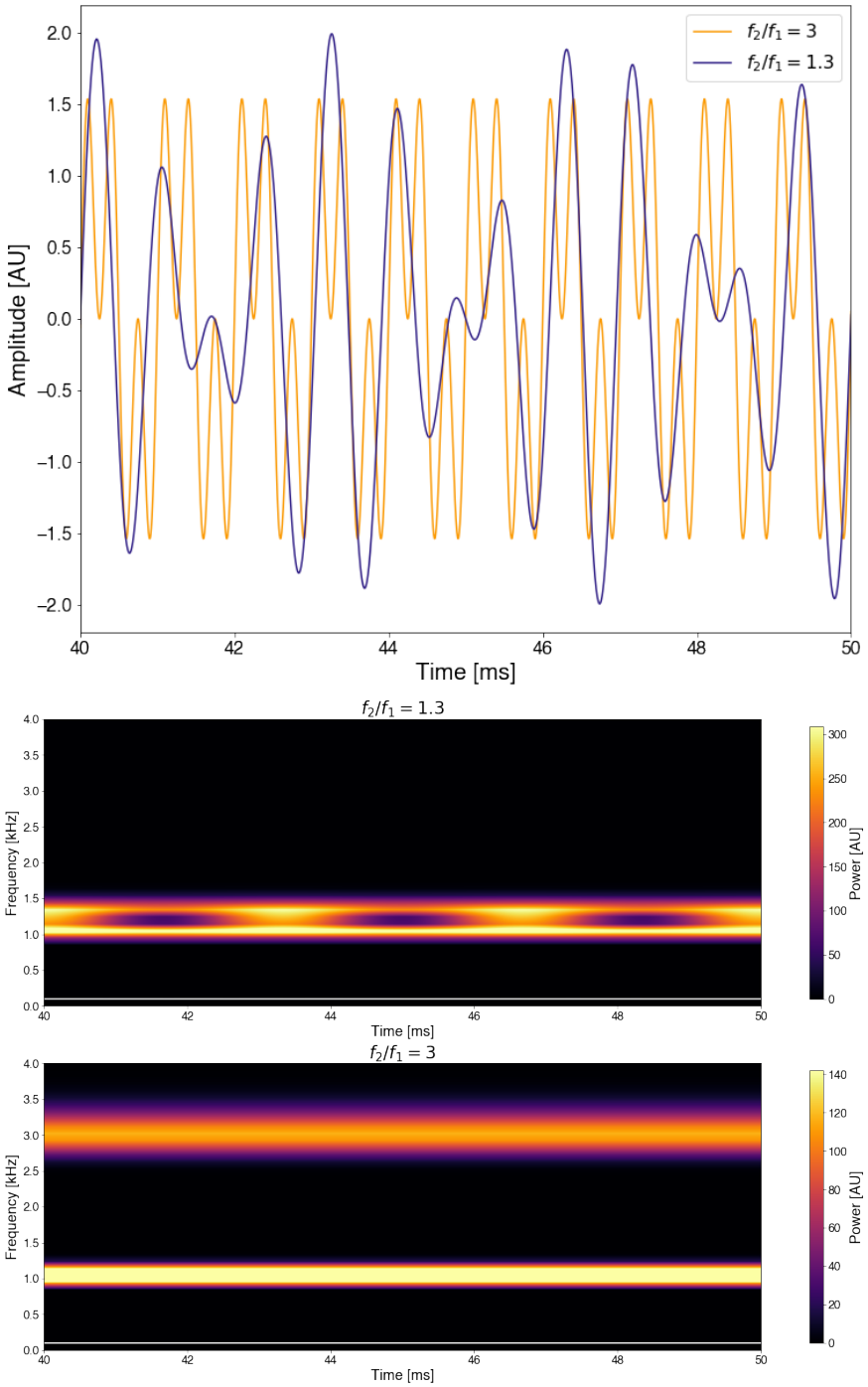

Figure 3.9: Demonstration of how closely spaced frequencies show up in a wavelet power spectrum. (Top)Temporal plot of both signals (center) Wavelet transform for frequencies separated by a factor of 1.3; c) wavelet transform for frequencies separated by a factor of 3.

Cone of Influence

As in Fourier analysis, a decision has to be made about how to handle the ends of a time series. One common solution is to pad the time series with zeros before conducting the wavelet transform, and remove them afterward. However, this will certainly impact the calculated values of the wavelet transform near the ends of the time series. The Cone of Influence is the region of the wavelet spectrum impacted by these boundary effects, and will be defined as the e-folding time for the autocorrelation of the wavelet power at each scale (meaning any effect from the boundary will have decreased by a factor of e^2) [3]; this is $\sqrt{2}a$ in the case of the Morlet wavelet. This is represented by the white lines seen in Figure 3.7. Anything outside those lines should not be trusted due to boundary effects. To ensure such boundary effects do not enter into calculations, higher-order quantities will only be calculated over the $20 - 80$ ms window.

Wavelets are in many ways designed to succeed where Fourier transforms fail. They provide time resolution in a mathematically robust way, rather than by imposing a pre-determined scaling, such as the selection of a window length. Additionally, the time averaged wavelet spectrum provides an unbiased estimate of the true power spectrum [99]. However, they are not perfect in their resolution, and there is a trade off between better frequency resolution at lower frequencies/longer times and worse frequency resolution at higher frequencies/shorter times. A useful pictorial representation of this is provided on Wikipedia (Figure 3.10). The cone of influence also provides a measure of the decorrelation time at a given frequency - if an apparent peak in the wavelet transform is shorter than the scale-appropriate decorrelataion time, it may well be due to random noise rather than a coherent signal [3].

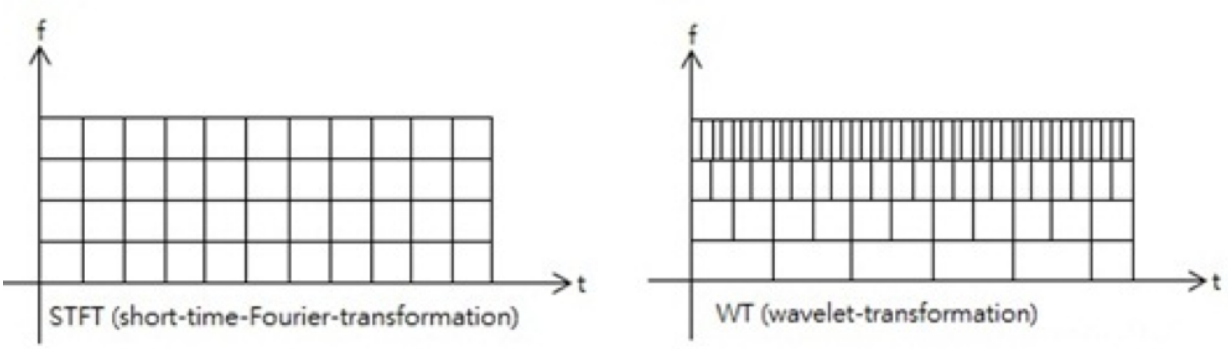

Figure 3.10: Resolution changes in the time-frequency plane for the Fourier (left) and wavelet (right) transforms.

3.5 Wavelet Bispectrum & Bicoherence

Analogous to the Fourier transform-based bispectrum and bicoherence, we can construct the wavelet bispectrum and bicoherence over some time interval T [4]:

$$B_W(f_1, f_2) = \int_T W(f_1, \tau) W(f_2, \tau) W^*(f_1 + f_2, \tau) d\tau \tag{3.17}$$

$$b^2_W(f_1, f_2) = \frac{|\int_T W(f_1, \tau) W(f_2, \tau) W^*(f_1 + f_2, \tau) d\tau|^2}{\int_T |W(f_1, \tau) W(f_2, \tau)|^2 d\tau \int_T |W(f_1 + f_2, \tau)|^2 d\tau}. \tag{3.18}$$

Again, this can be reformulated for use on a time series with N points with equal spacing δt as:

$$\tilde{B}_W(f_1, f_2) = \sum_{\tau=0}^{N-1} W_j(f_1, \tau) W_j(f_2, \tau) W^*_j(f_1 + f_2, \tau) \delta t \tag{3.19}$$

$$\tilde{b}^2_W(f_1, f_2) = \frac{|\sum_{\tau=0}^{N-1} W(f_1, \tau) W(f_2, \tau) W^*(f_1 + f_2, \tau) \delta t|^2}{\sum_{\tau=0}^{N-1} |W(f_1, \tau) W(f_2, \tau)|^2 \delta t \sum_{\tau=0}^{N-1} |W(f_1 + f_2, \tau)|^2 \delta t}. \tag{3.20}$$

The wavelet bicoherence is bounded between 0 and 1, just as in the Fourier case. Note that the results of these calculations will be strongly influenced by the choice of time interval T. Van Milligen et al. [83] detail how this time can set both the statistical noise level and the statistical error for the bicoherence. Throughout this thesis we use time intervals of $N = 1000$ points ($T = 4ms$), which results in an error estimate of 0.06 and a frequency-dependent bicoherence noise floor of

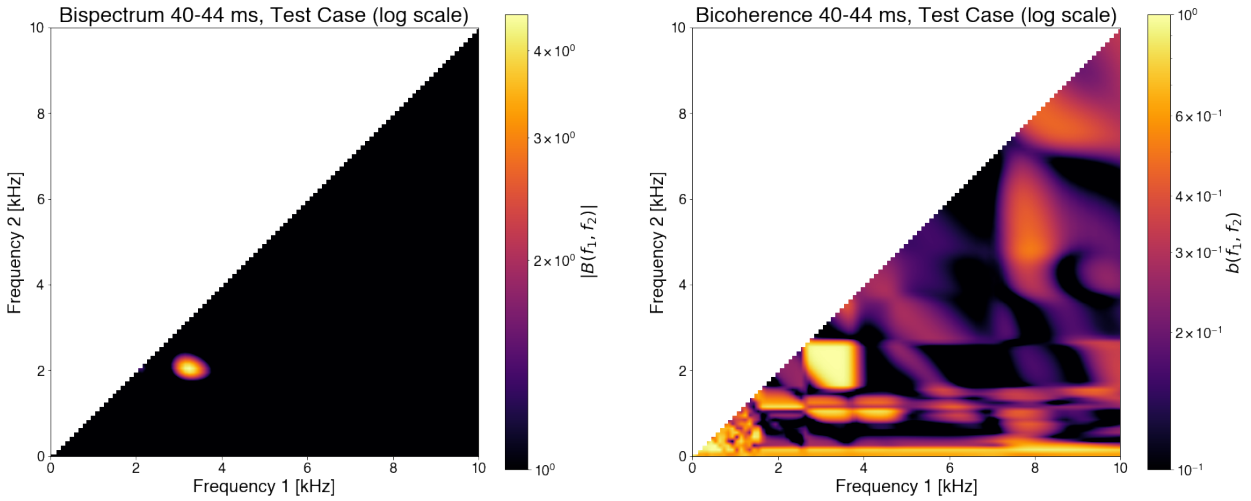

Figure 3.11: Wavelet bispectrum (left) and bicoherence(right) for a 4 ms segment of the test data. The coordinates of the phase coupled waves are clearly visible. Note that the high bicoherence along the $f_2 = 0.1$ kHz line is outside the cone of influence and therefore not to be trusted.

$\sim 0.35 - 0.15$ for the frequencies of interest. The change in the bicoherence of Gaussian noise (which approximates the noise floor) with the number of points used to calculate the bicoherence can be seen in figure 3.12. Because we are interested in the detailed temporal behavior of the three-wave coupling (which cannot be fully captured by the bicoherence due to the required integration times), we will primarily focus on the bispectrum and treat the results as qualitatively valid if the corresponding bicoherence is above the noise floor. It is worth noting that even with its restrictions, the wavelet bicoherence represents an improvement over the Fourier bicoherence, whose error decays as $\sqrt{M/N}$ [83] and thus requires a factor of M more samples to achieve the same statistical error. Although we cannot rigorously calculate the bicoherence at every point in time, it can capture features just as well as the Fourier bicoherence over the same time interval (see Figure 3.11).

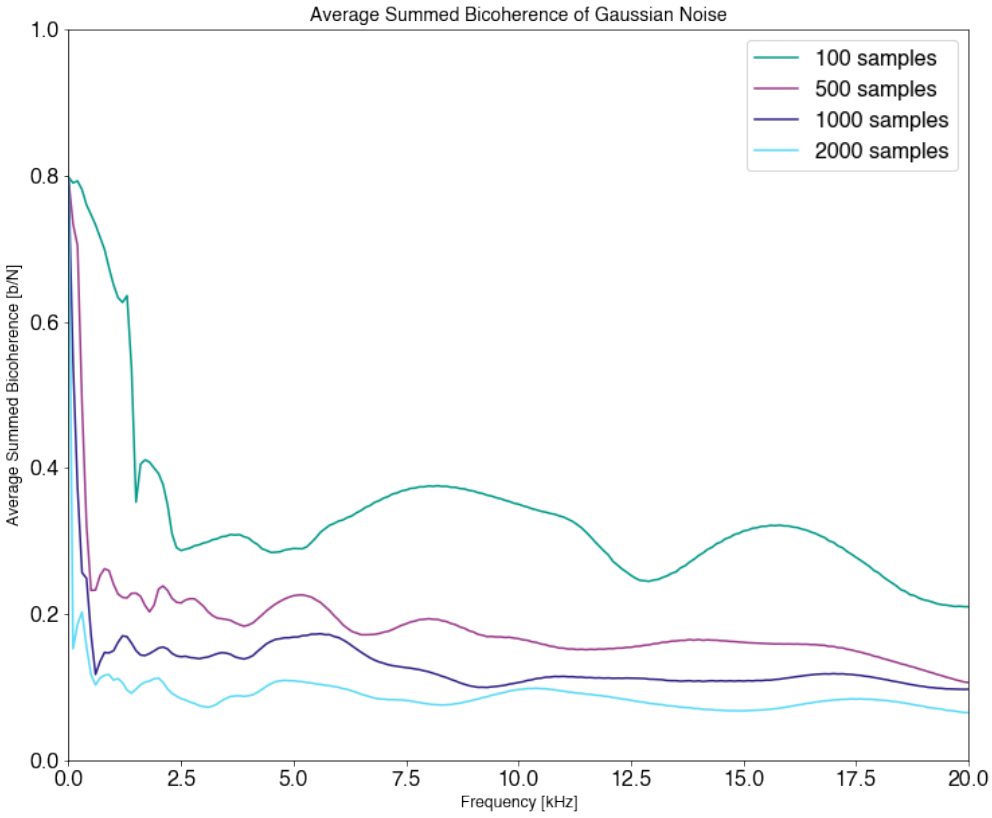

Figure 3.12: Convergence of the summed bicoherence of Gaussian noise toward 0 with increasing sample size. These traces approximate the changes in the noise floor with frequency and sample size. This work uses a sample size of 1000 points, resulting in an estimate for the noise floor of ~ 0.35 at 400 Hz and decreasing to ~ 0.15 for most of the frequency range of interest.

To see what this 4 ms resolution in the wavelet bicoherence gets us, we can plot slices taken at specific frequencies, which show how that frequency interacts with all other frequencies in time (Figure 3.13). The time resolution is set by the window size used to calculate the wavelet bicoherence.

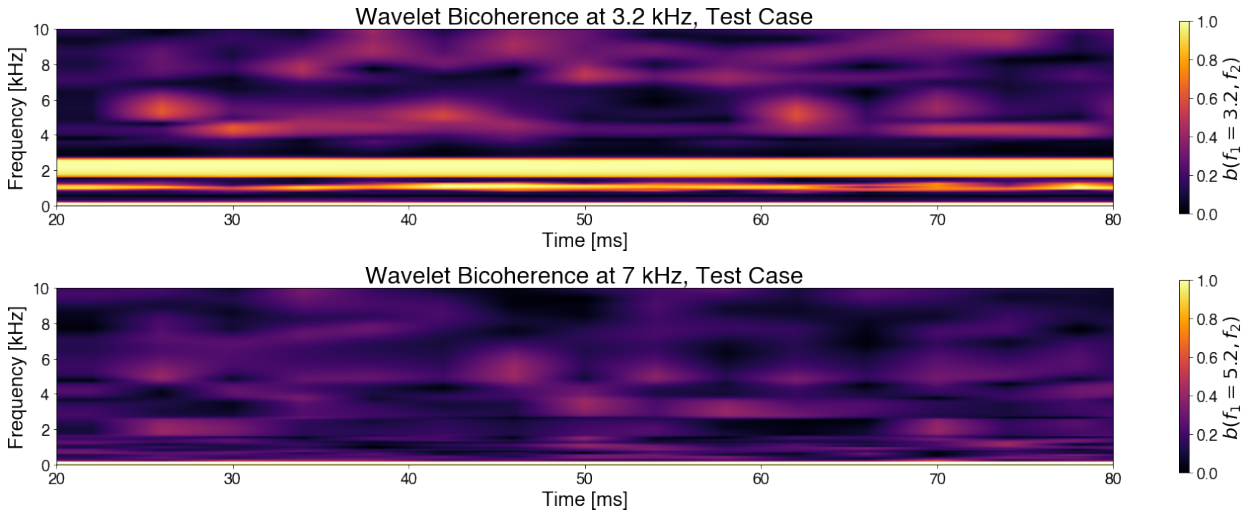

Figure 3.13: Time-resolved wavelet bicoherence (4 ms windows) showing interactions with 3.2 kHz (top) and 7 kHz (bottom). Note the clear phase coupling between 3.2 and 2 kHz, and the lack of any significant coupling with 7 kHz.

However, the bispectrum does not necessarily require the use of windows in the same way as the bicoherence does. Rather, we can treat each sample as being integrated over the 4 μs window it represents, and calculate the bispectrum with this 4 μs resolution (Figure 3.15). Note that the bispectrum calculated in this way will have a larger error than if estimated by integrating over a longer window. However, the results will still be qualitatively correct, and as our focus is the qualitative picture and the statistics of how the bispectrum is distributed, this is acceptable for our use so long as the corresponding bicoherence is above the noise floor.

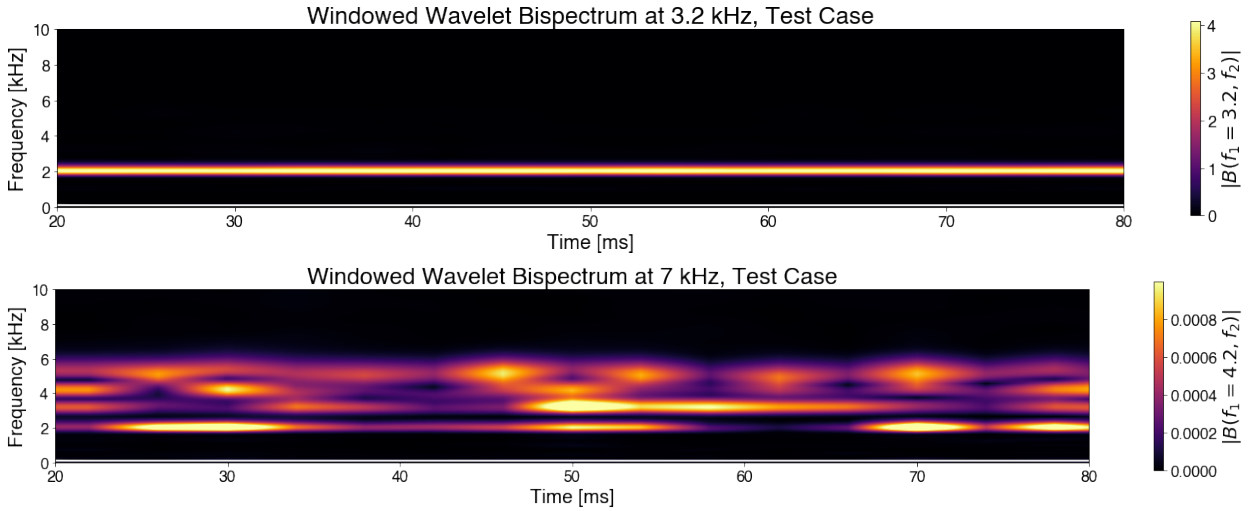

Figure 3.14: Wavelet bispectra constructed over a 4 ms window, in analogy with the wavelet bicoherence at 3.2 kHz (top) and 7 kHz (bottom). Note that the scales on the colorbar differ by 3 orders of magnitude; a 7 kHz fluctuation is not coupling with any other frequencies (because there is essentially no power at 7 kHz), while the 3.2 kHz fluctuation shows strong coupling with 2 kHz (as was imposed).

Note that when using the shortest possible integration window, the bispectrum will be orders of magnitude smaller because of the shortened integration window; this can be seen in the difference between the respective colorbars of Figures 3.14 and 3.15. However, the two figures are qualitatively in agreement, showing strong, consistent interaction between the phase-coupled oscillations at 2 and 3.2 kHz, while showing $\sim$ 1000$\times$ weaker interactions between 7 kHz and the 2-6 kHz frequency range. These weak interactions arise due to a combination of phase noise and use of signals close in frequency.

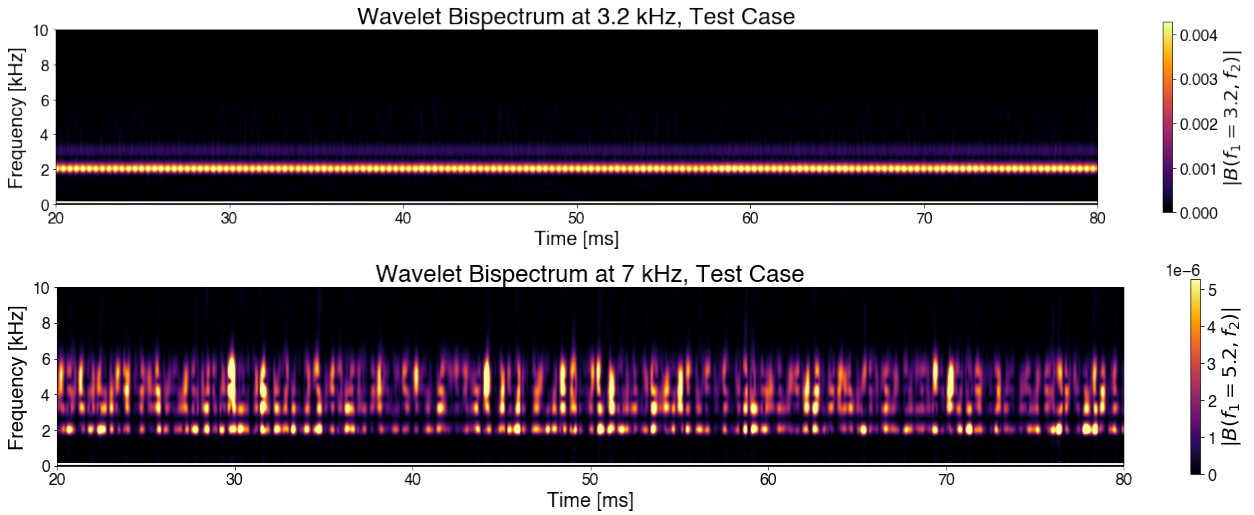

Figure 3.15: Wavelet bispectrum calculated every 4 μs (the sampling time) at 3.2 kHz (top) and 7 kHz (bottom). Note the scales on the colorbar differ by 3 orders of magnitude.

3.6 Intermittency and the Gamma Distribution

When discussing turbulent fluctuations, intermittency has a more precise meaning than it might in daily use. Rather than simply indicating that a signal is only occasionally present, it specifically means that the statistics of the fluctuating quantity deviate from a Gaussian distribution; more precisely, that there are large tails to the distribution indicating "extreme" events are more likely than if the fluctuations were purely random. This deviation from Gaussianity is quantified by the kurtosis

$$\kappa = \frac{\int_{-\infty}^{+\infty} x^4 f(x) dx}{\sigma^4} = \frac{\langle x^4 \rangle}{\langle x^2 \rangle^2} \tag{3.21}$$

where x is a random variable, $f(x)$ is the random variable's probability distribution function, and σ^2 is the variance of $f(x)$. The kurtosis is also a measure of the flatness of $f(x)$, with a more sharply peaked profile yielding $\kappa > 3$ (called leptokurtic) and a flatter profile yielding $\kappa < 3$ (called platykurtic); the kurtosis of a Gaussian is exactly 3. Leptokurtic distributions have heavier tails, indicating that extreme outlier events are more probable than in Gaussian or platykurtic distributions. Note that there are two ways to think about interimittency: whether the kurtosis of the fluctuations at a particular frequency are ≥ 3, and whether kurtosis increases with frequency with-

out bound [34]. Both definitions are important and will be used throughout this work. Examples of a histogram estimating the probability distribution function and the kurtosis of the wavelet power spectrum (Figure 3.8) for different frequencies in our test case are shown in Figure 3.16, while the kurtosis as a function of frequency is shown in Figure 3.17. We can summarize the information in these figures by stating that the wavelet power spectrum of this system shows intermittency, and that the distribution of power at frequencies outside the 2-6 kHz range is leptokurtic.

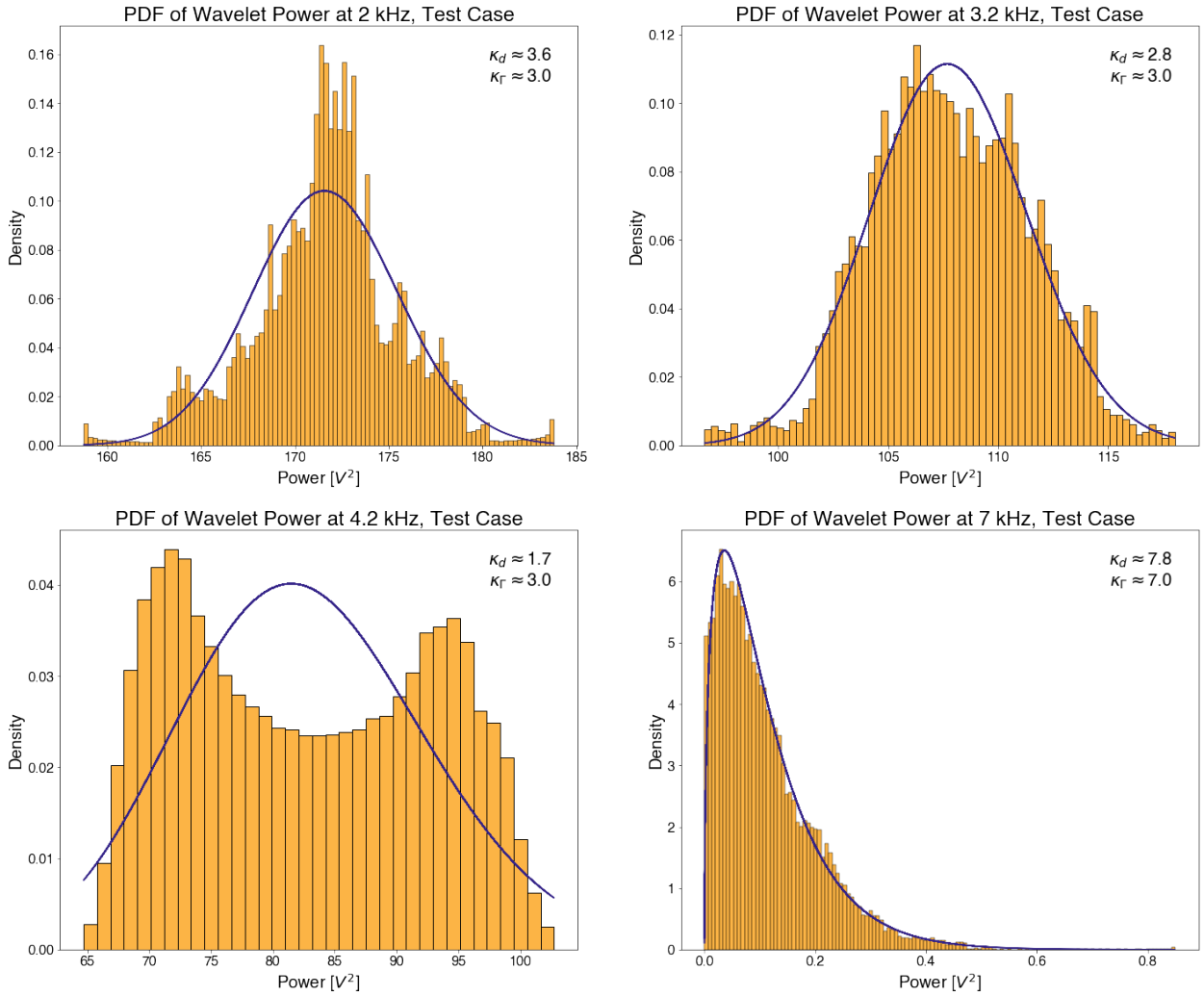

Figure 3.16: Histograms of the power at the three coupled and one uncoupled frequency. Note that 4.2 kHz has a distribution function characteristic of sinusoids due to the periodic variation in power at that frequency under the wavelet transform, while the distribution function at 7 kHz is nearly exponential. The distribution functions at 2, 3.2, and 7 kHz are all fairly well approximated by a Gamma distribution.

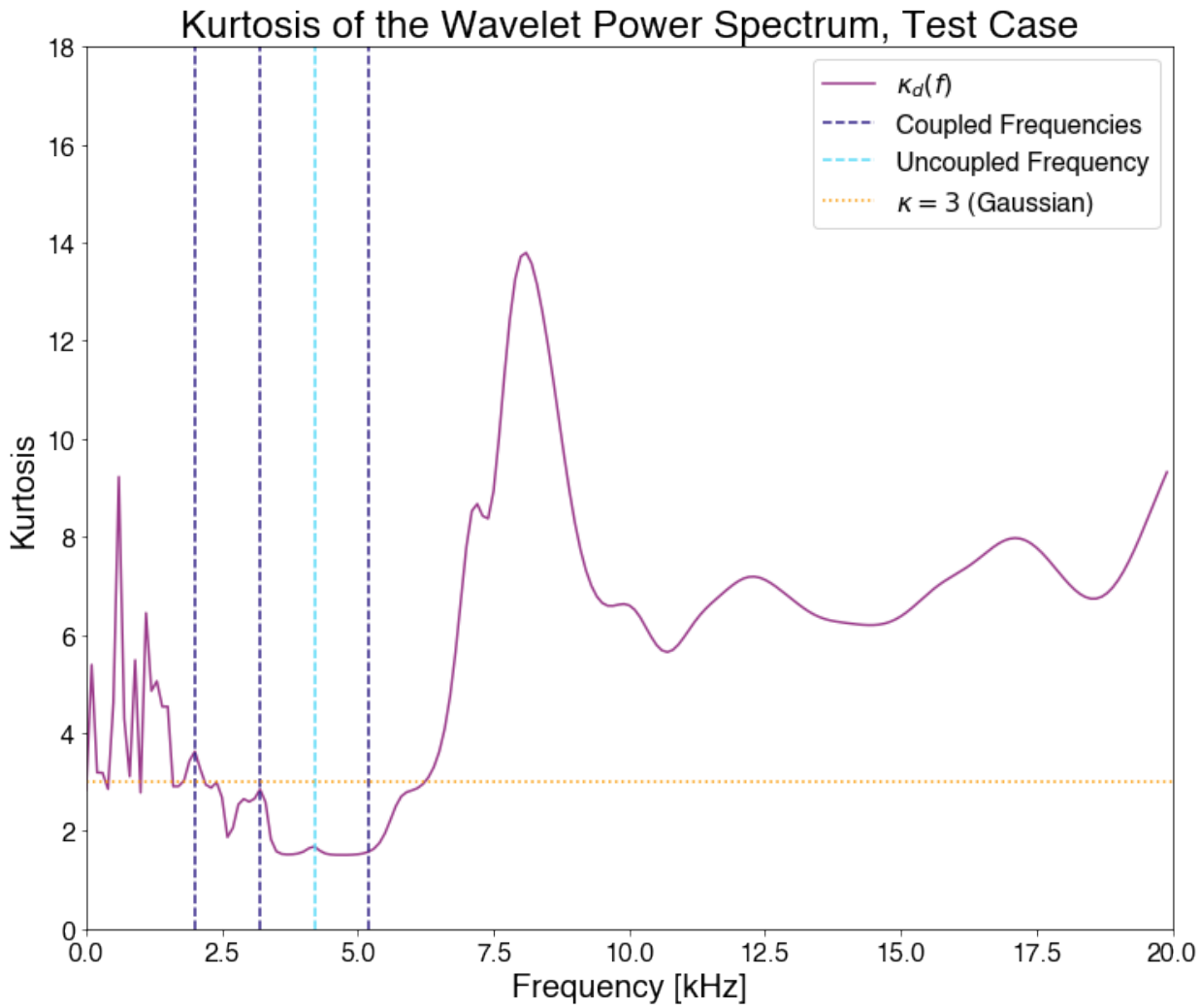

Figure 3.17: Kurtosis as a function of frequency for the test case, indicating intermittency at frequencies above 7 kHz and below 1.5 kHz

Rather than simply looking at histograms, it can be useful to characterize a variable by an analytic probability distribution function. Previous work has found that the amplitude of fluctuations in the scrape-off layer of tokamak plasmas can be well approximated by a Gamma distribution [100, 101]:

$$P(x) = \frac{\beta^{\alpha} x^{\alpha-1} e^{-\beta x}}{\Gamma(\alpha)}, \tag{3.22}$$

$$\alpha = \frac{\langle x \rangle^2}{\sigma(x)^2} \qquad \beta = \frac{\langle x \rangle}{\alpha} = \frac{\sigma^2}{\langle x \rangle} \tag{3.23}$$

where $\Gamma(*)$ is the gamma function, α is the shape parameter, and β is the rate parameter.. Garcia [102] presents a stochastic model for intermittent fluctuations in the scrape-off layer which treats the fluctuations as a series of bursts. In this model, α is proportional to the ratio of the burst duration to the wait time between bursts τ_d/τ_w, while β influences the width of the distribution. Part of the utility of the Gamma distribution is that it can take on different shapes based on the values of α and β, as can be seen in Figure 3.18. These shapes range from nearly Gaussian to highly exponential, ideal when studying intermittency.

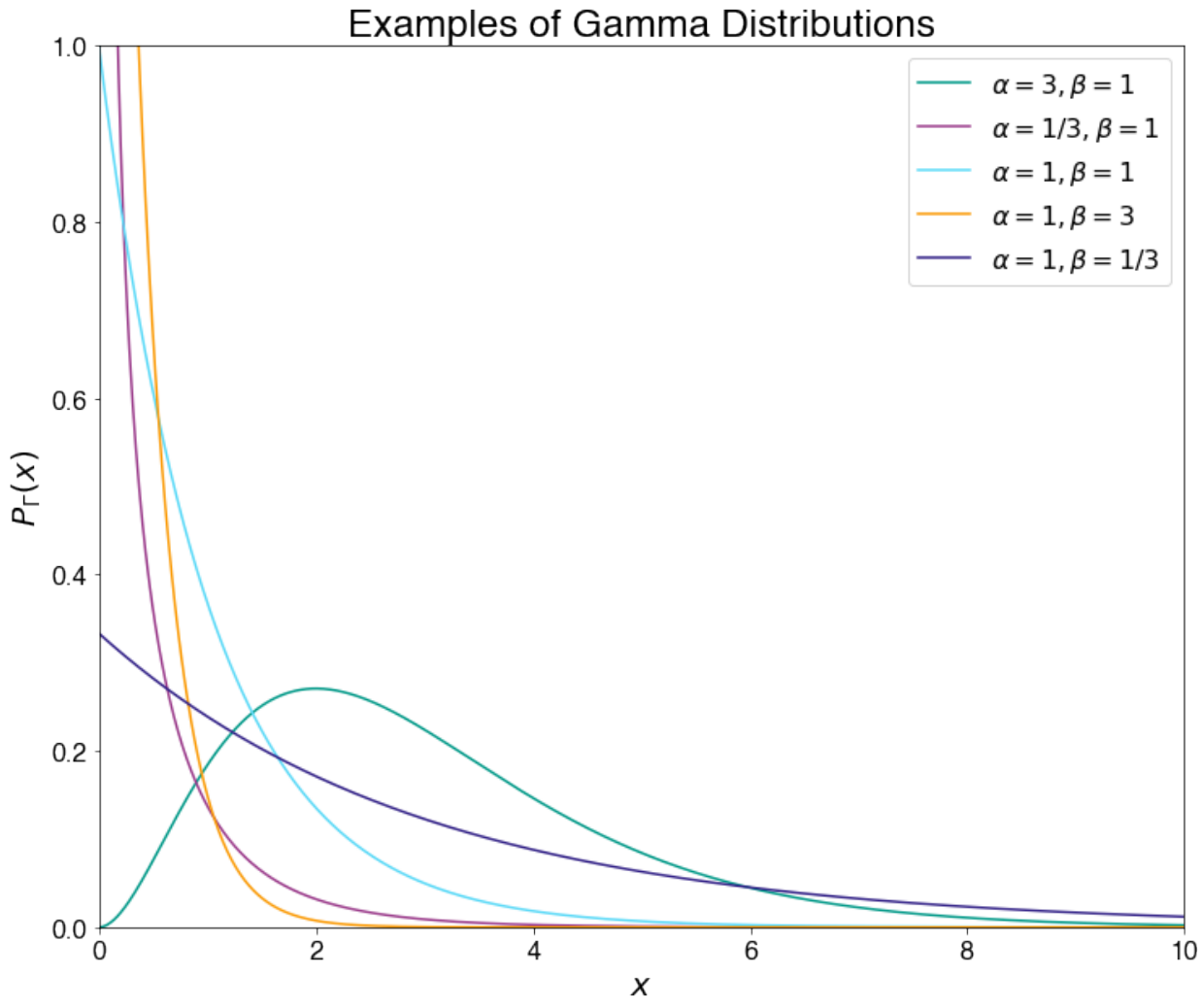

Figure 3.18: Examples of Gamma distributions for a variety of shape (α) and rate (β) parameters.

The Gamma distribution also provides a second method for calculating distribution moments, which can be related to the parameters α and β. Most relevant to this work is the kurtosis, which

is

$$\kappa_\Gamma = 3 + \frac{6}{\alpha} \tag{3.24}$$

for a Gamma distribution. Note that because alpha must always be positive, a Gamma distribution can never have a kurtosis less than 3. This means that a Gamma distribution is an incredibly poor fit for any platykurtic (flat) distribution, such as those for the wavelet power at 4.2 and 5.2 kHz in our test case (see Figure 3.16). This is not surprising, given that the Gamma distribution is intended for use with intermittent data and the power at the test frequencies varies periodically, rather than intermittently.

In situations where the use of the Gamma distribution is appropriate, comparing the kurtosis as calculated directly from the data to that of the corresponding gamma distribution provides an opportunity to assess whether enough samples have been used for the distribution statistics to converge to their true values; if the kurtosis calculations agree, we can use Garcia's physical interpretation of the α parameter when interpreting the results. There is no "goodness of fit" test for the Gamma distribution, so this method provides a somewhat intuitive check. Higher-order moments such as the kurtosis can require more than 30,000 samples to converge (Figure 3.19), while the mean and variance converge much more quickly. Computational limitations - specifically the memory available on the consumer laptop and desktop computers used for this analysis - prohibit us from using the full 30,000 samples to guarantee the convergence of the kurtosis in this work. We are instead restricted to using 15,000 samples, meaning the mean and variance have fully converged but the kurtosis has not. If the kurtosis of the Gamma distribution (calculated from the converged mean and variance) agrees fairly well with the kurtosis calculated from the data directly, we take that as a sign that the kurtosis is nearly converged and is useful for analysis; in cases of disagreement, additional samples are required to draw any conclusions.

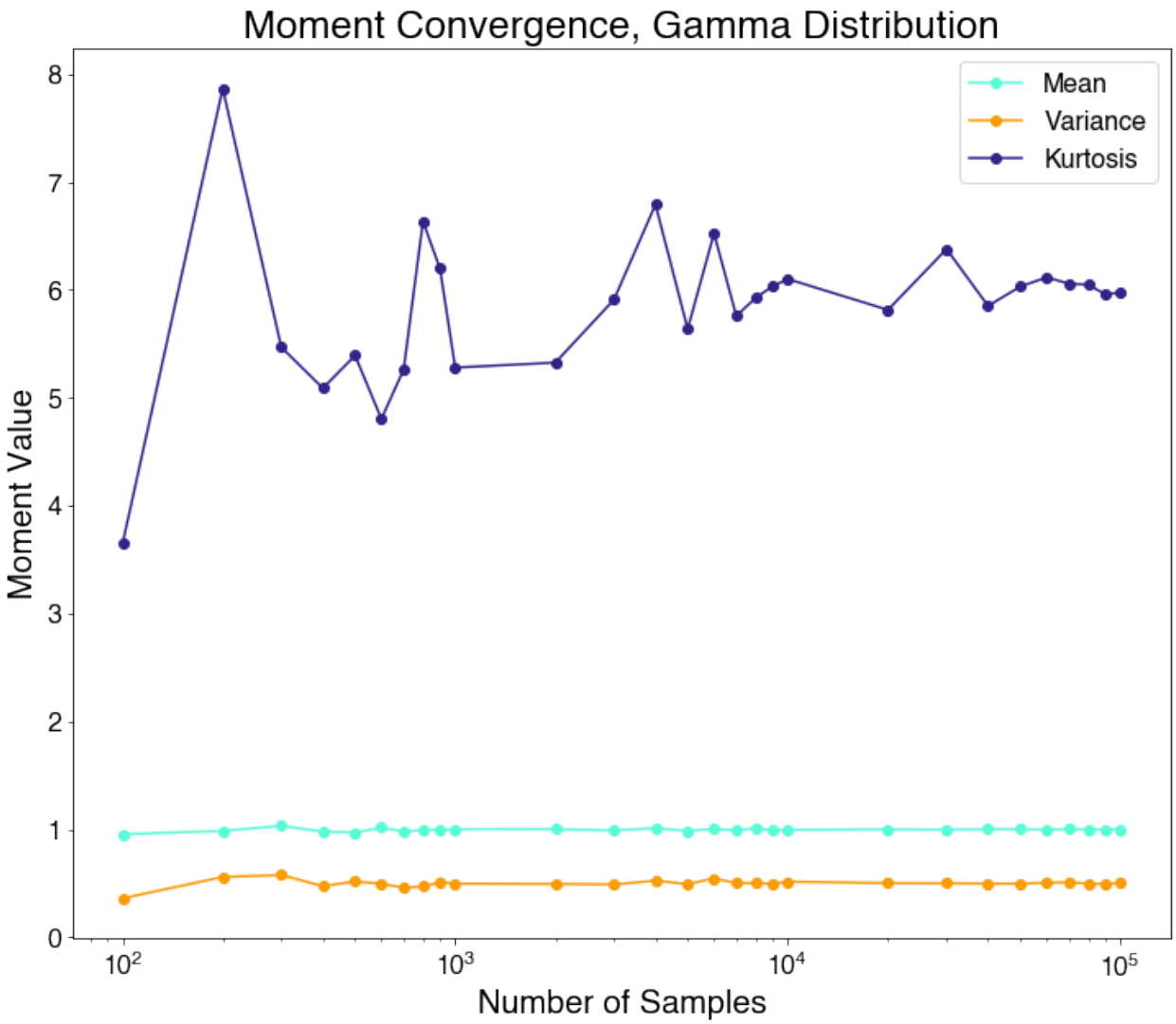

Figure 3.19: Change in mean, variance, and kurtosis for a gamma distribution as a function of the number of random samples used in the calculation.

3.6.1 Application to Bispectral Data

It is well established that the turbulent coupling between two frequencies is constant in time, but that does not mean that the power transfered between waves via that coupling is constant in time. To characterize the intermittency of power transfer via nonlinear interactions between oscillations at different frequencies, we apply the above techniques to the summed wavelet bispectrum, where the sum is conducted over all $f_1 = f$, $f_2 = f$, and $f_3 = f$ to capture the total amount of interaction with a particular frequency f (Figure 3.20). This sum will be conducted over only the central 60

ms window (470-530 ms) to avoid any edge effects from the wavelet transform at the frequencies of interest.

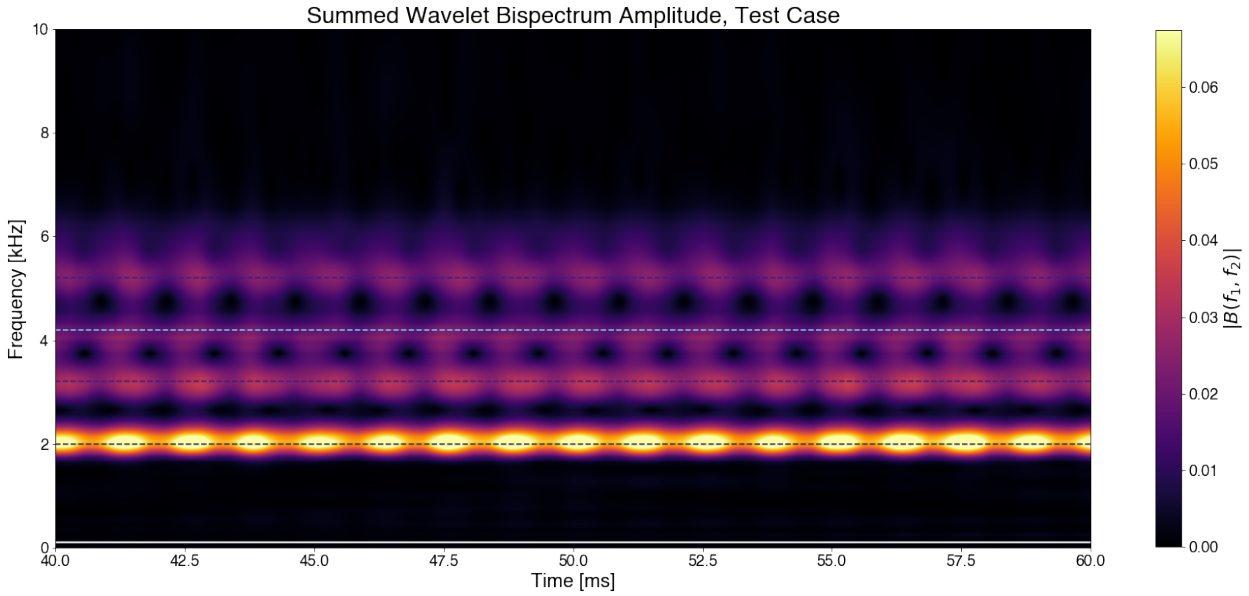

Figure 3.20: Summed wavelet bispectrum for our test case.

The bispectrum is largest at 2 kHz because it is the only frequency sufficiently separated from the others to avoid the close frequency effects shown in Figure 3.9. The summed wavelet bispectrum clearly shows that 2, 3.2, 4.2 and 5.2 kHz all participate in some type of coupling. However, when we check the wavelet bicoherence and time-resolved bispectrum at 4.2 kHz (Figure 3.21), we see that nealy all of the bispectrum arises from a supposed interaction with the 2 kHz wave, even though the bicoherence for 4.2 kHz at 2 kHz is always below our noise floor of 0.35. Thus we disregard the apparent summed wavelet bispectrum at 4.2 kHz as spurious. Contrastingly, for 3.2 kHz, we see a strong interaction with 2 kHz in the bispectrum (Figure 3.22), supported by a bicoherence of 1, so we take that coupling to be meaningful.

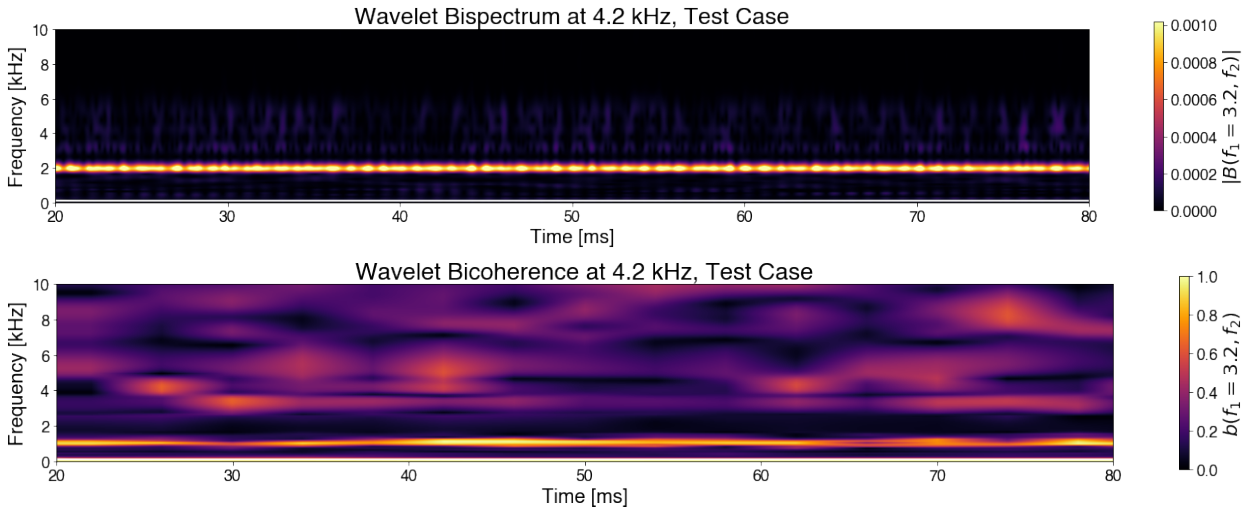

Figure 3.21: Wavelet bispectrum (top) and bicoherence (bottom) for our test case at 4.2 kHz. Note that even though the bispectrum is large at 2 kHz, the bicoherence is quite small and does not clear the noise floor, meaning the summed bispectrum value at 4.2 kHz in Figure 3.20 is spurious.

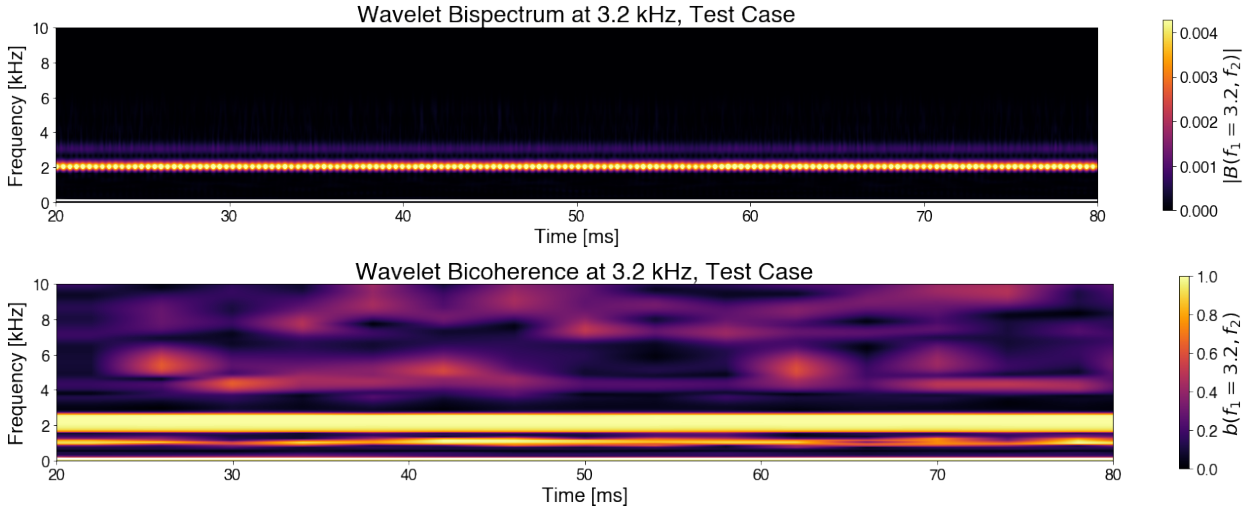

Figure 3.22: Wavelet bispectrum (top) and bicoherence (bottom) for our test case at 3.2 kHz. The large bispectrum at 2 kHz is supported by a bicoherence of 1, meaning the summed bispectrum value at 3.2 kHz in Figure 3.20 is trustworthy.

Turning our attention to the distribution functions for the summed wavelet bispectrum at the driven frequencies, we see that once again the Gamma distribution is a poor fit due to the lack of intermittency in our test case (Figure 3.23). Concerns about convergence of the kurtosis are irrelevant in this case because the Gamma distribution by definition will not be able to capture the true behavior of the system.

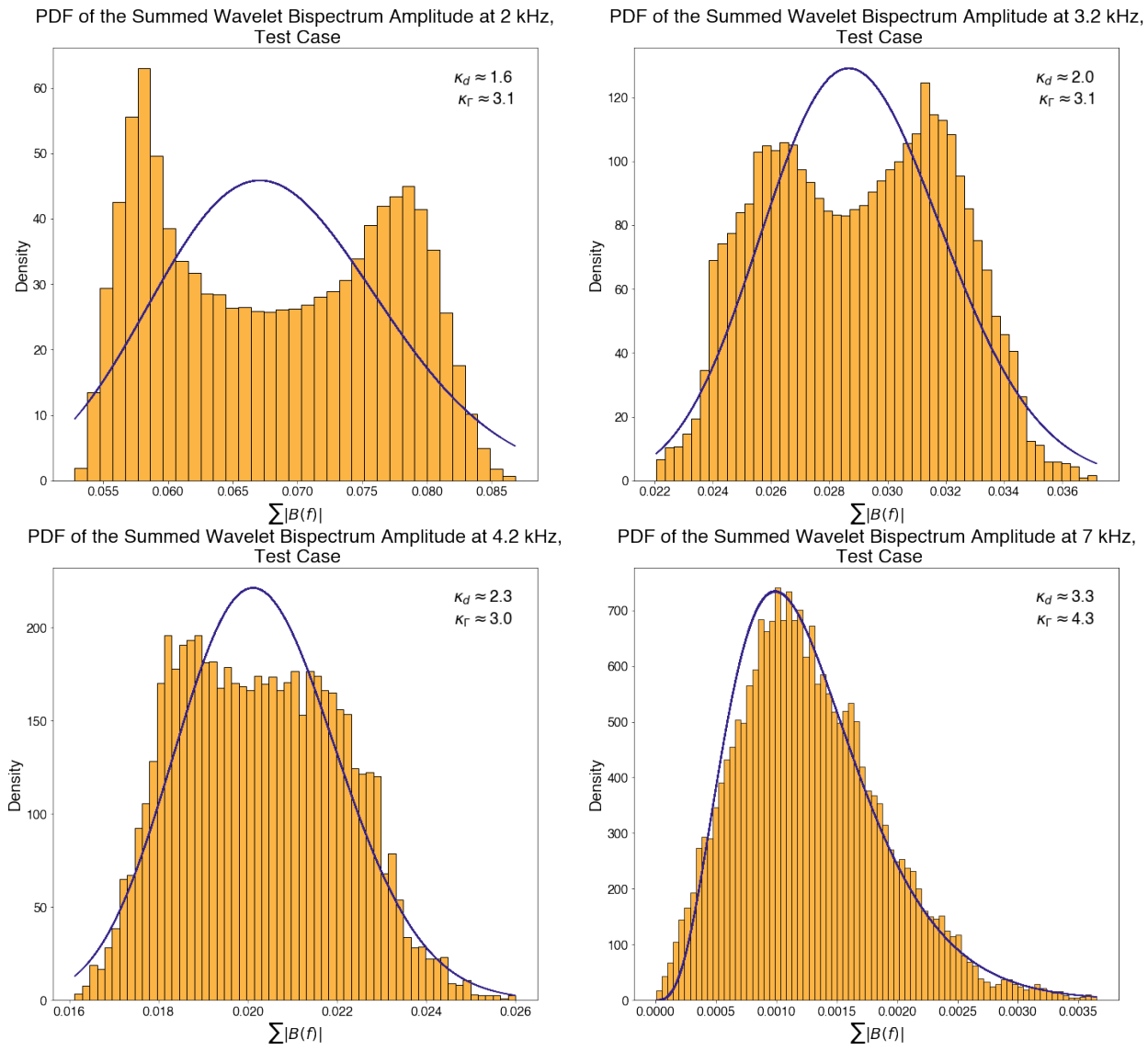

Figure 3.23: Distribution functions of the amplitude of the summed wavelet bispectrum at the driven frequencies in our test case. Note that the Gamma distributions are a poor fit at 2, 3.2, and 4.2 kHz due to the lack of intermittency, while the fit is better for the intermittent 7 kHz.

Finally, we note that the kurtosis of the amplitude of the summed wavelet bispectrum does not increase with frequency (Figure 3.24). This means that while there may be intermittentency in the power spectrum (Figure 3.17), the energy transferred via three-wave coupling in the test system does not meet Frisch's definition of intermittency, although it does have a non-Gaussian distribution at many frequencies.

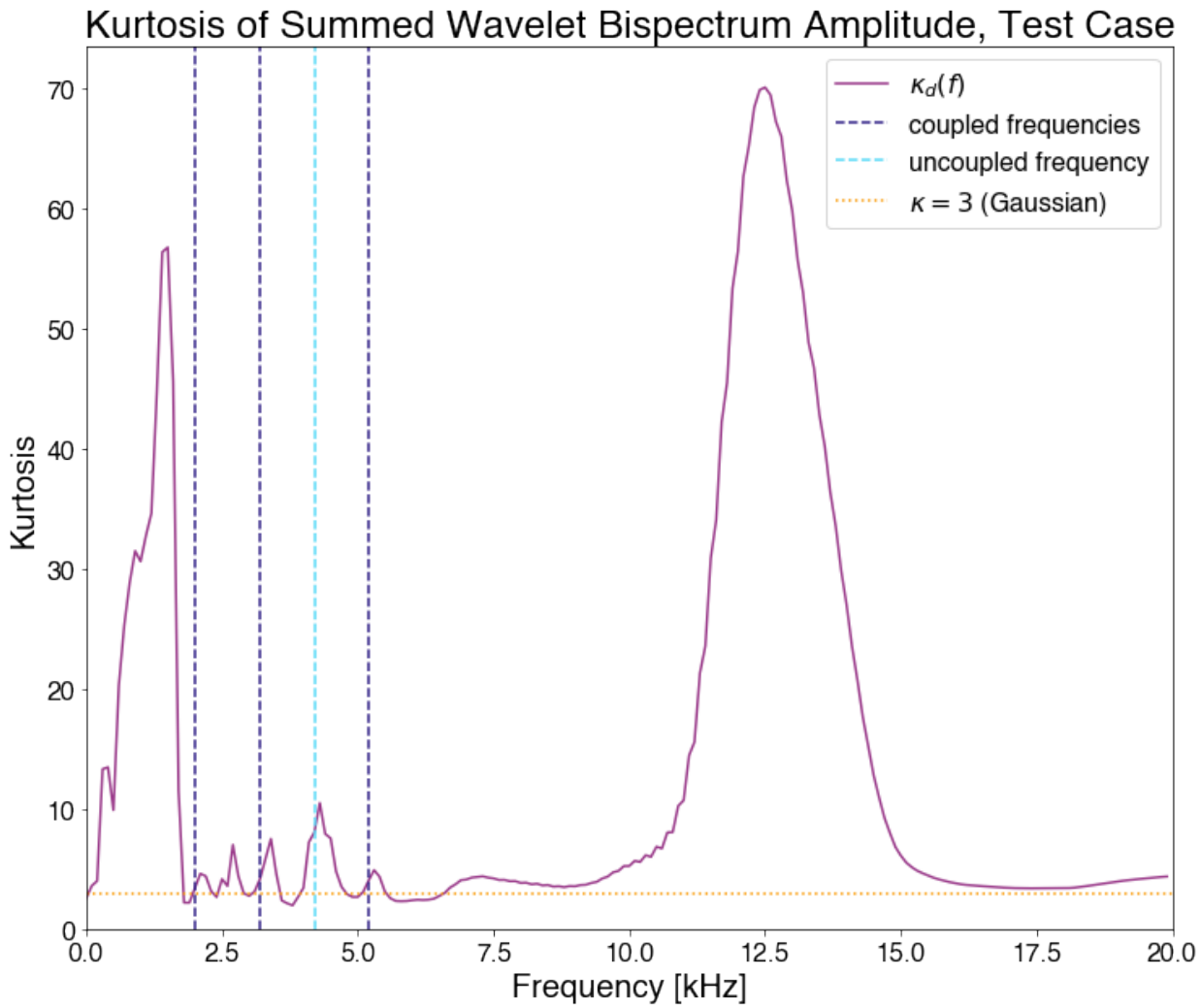

Figure 3.24: Kurtosis as a function of frequency for the amplitude of the summed wavelet bispectrum in our test case. Although the amplitude of the summed wavelet bispectrum is non-Gaussian at many frequencies, this does not meet the strict intermittency criteria of increasing kurtossis with frequency.

3.7 Summary

The analysis tools used in this thesis are based on digital transforms of measured time series from a turbulent plasma. The wavelet transform provides a nearly instantaneous measurement of the frequencies present at any moment and functions as a digital filter bank, transforming a single fluctuating time series into many time series corresponding to the individual frequency bands which make up the original signal. We select the Morlet wavelet for this study, which is the product of a

sinusoidal fluctuation and a Gaussian window scaled by the frequency of the sinusoid. The wavelet transform is used to compute the instantaneous wave power spectrum and study the intermittency of the fluctuation power within individual frequency bands. We next compute the instantaneous wavelet bispectrum, which is proportional to the rate of energy transfer between waves. Unlike more common Fourier transform methods and the ensemble-averaging of short-time Fourier transforms, wavelet analysis reveals the intermittency of wave power at various frequencies.

Chapter 4: Intermittency of the Power Spectrum in Dipole Plasma Turbulence

This chapter will apply the techniques introduced in Chapter 3 to study two-dimensional electrostatic turbulence under a variety of conditions on CTX. We focus in particular on the intermittency of the fluctuation power, as measured by the wavelet power spectrum and its associated probability distribution function. We find that the fluctuation power is always intermittent, having kurtosis greater than 3 at nearly all frequencies and increasing with frequency (meeting Frisch's criteria).

In addition to observations of fully developed turbulence sustained by plasma heating, two techniques are used to modify the baseline turbulence by launching electrostatic waves into the plasma: driving coherent tones and applying active feedback. Active feedback corresponds to launching broadband fluctuations which are amplified and phase-delayed versions of the measured turbulent spectrum. Waves are launched from the bias probes described in Section 2.4.2 and use the feedback/drive system detailed in Section 2.5 to interact with the plasma. Launching waves into the turbulence decreases the intermittency of the driven waves while increasing the intermittency of other waves. Similarly, application of active feedback to amplify the turbulence increases coherence (decreases intermittency), while feedback suppression increases the intermittency of the wave energy.

This chapter is organized into three primary parts and includes some additional observations. First, the statistics of the wave power spectrum for sustained plasma turbulence without external wave launching is presented. Next, we present observations of wave intermittency when the time-averaged intensity of the fluctuations is elevated (Section 4.2 or reduced (Section 4.3). Finally, we demonstrate how the linear interference of three waves close in frequency can replicate a pattern

that appears during one of the driven cases. For the following examples, all wavelet transforms are conducted over the 450 – 550 ms time window, while statistics are calculated over the 470 – 530 ms time window to avoid any edge effects from the wavelet transform. All plasma parameters are fluctuating about a stable average and any turn-on effects from feedback or drive systems have dissipated prior to the period studied.

4.1 Intermittency of Fluctuation Power in Electrostatic Turbulence

Using the wavelet power spectrum from Section 3.3, we first examine a plasma exhibting the baseline turbulence in CTX. Figure 4.1 shows the wavelet power spectrum for this fully-developed electrostatic turbulence, as measured by fluctuations of the floating potential. An ensemble-averaged Fourier power spectrum is included in Figure 4.2 for comparison. Most of the fluctuation power falls in a band between 1 and 12 kHz, visible in both spectra. The long-time power spectrum is the same whether calculated from an ensemble of Fourier spectra or by time-averaging the wavelet spectrum. However, the Fourier spectrum does not capture the temporal dependence of the fluctuation power, including major features such as the relatively quiescent period from ~480-490 ms seen in the wavelet power spectrum.

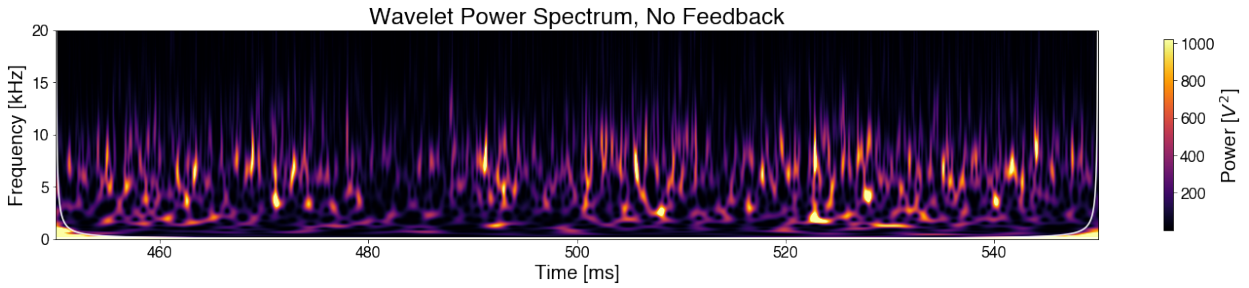

Figure 4.1: Wavelet power spectrum for a base-case CTX plasma during the feedback experimental run.

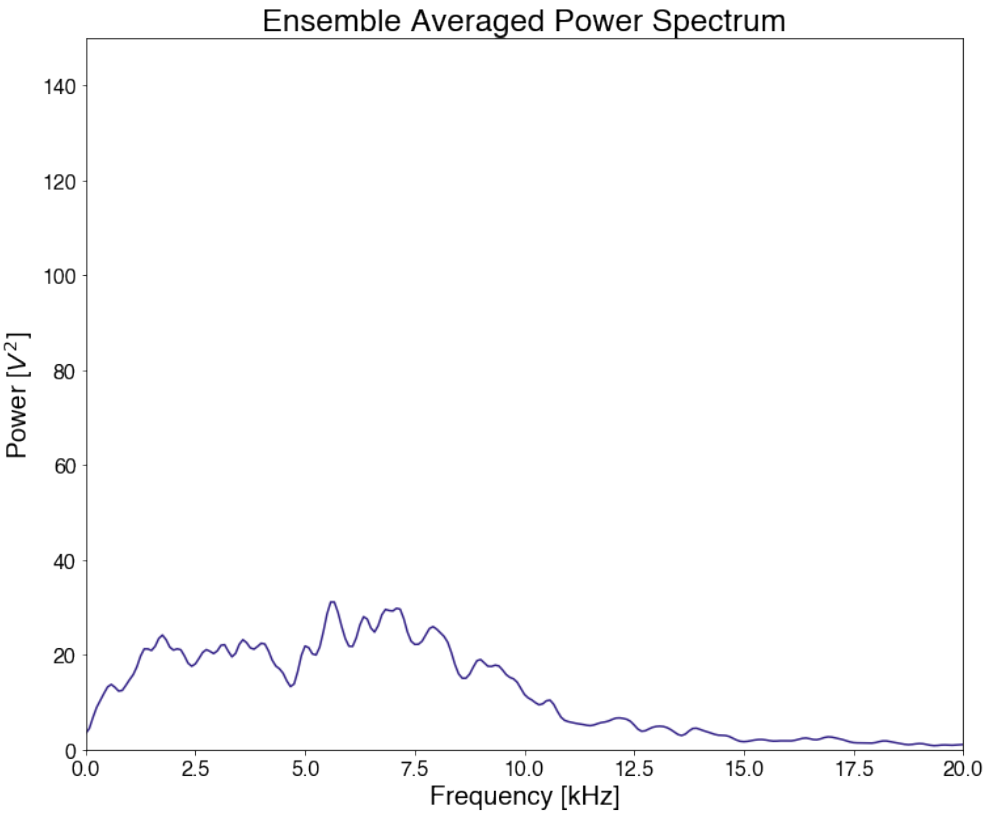

Figure 4.2: Ensemble averaged Fourier power spectrum for a base-case CTX plasma during the feedback experimental run.

The wavelet power spectrum makes clear that the frequency content of the signal changes rapidly in time, so we turn to the probability distribution function (PDF) of the power in the floating potential fluctuations to quantify the degree of intermittency. Figure 4.3 shows the PDF of the fluctuation power at four different frequencies, each overlaid with a corresponding Gamma distribution [102]. The kurtosis value for each frequency is included on their respective histogram, and displayed as a function of frequency in Figure 4.4. Note that both definitions of intermittency are satisfied: the kurtosis is greater than 3 at all frequencies outside the cone of influence, and the kurtosis increases with increasing frequency.

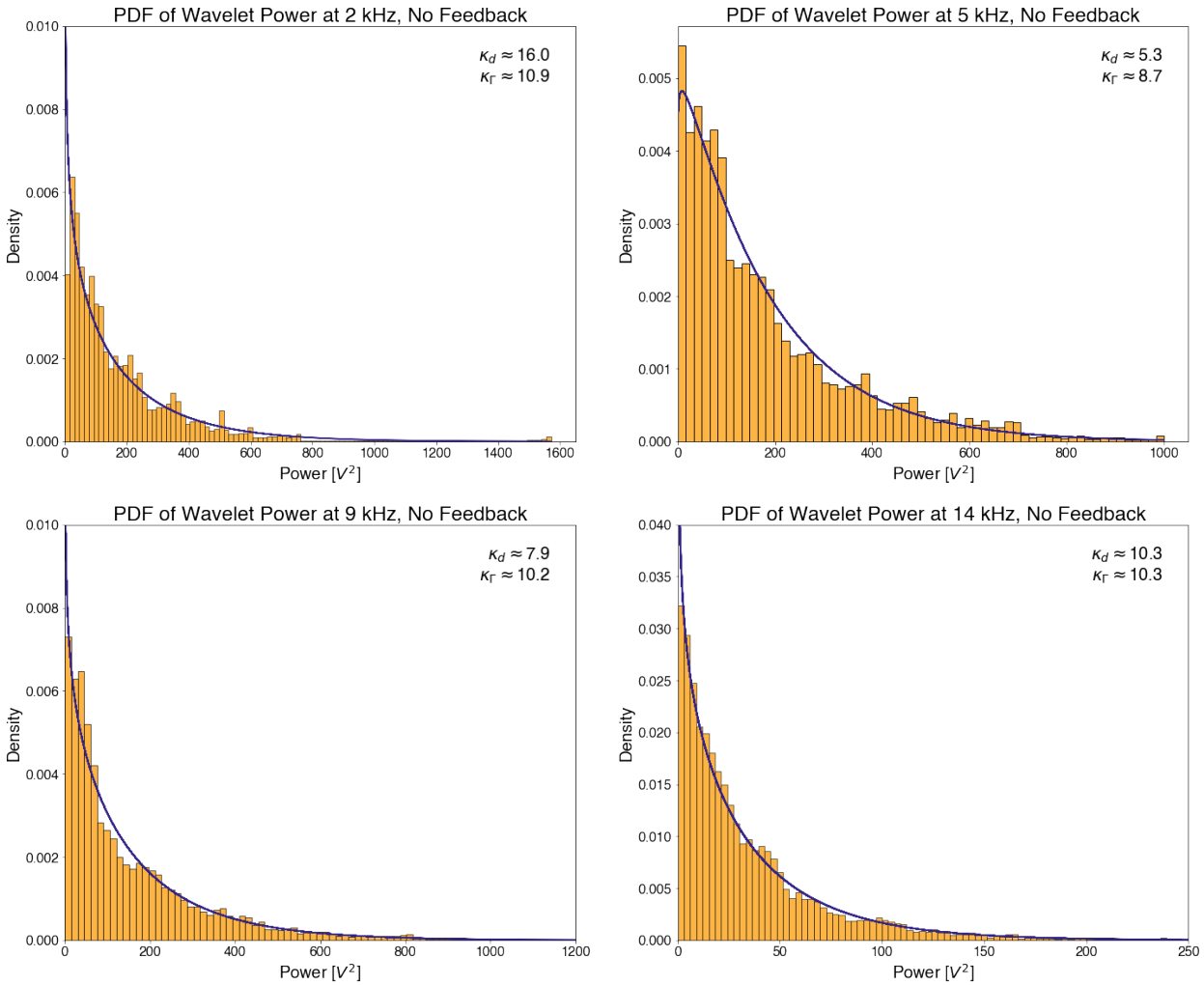

Figure 4.3: Histograms and PDF estimates of the power in fluctuations at 4 different frequencies (left to right top to bottom: 2 kHz, 5 kHz, 9 kHz, and 14 kHz). Kurtosis values for each are noted on the upper right of the plot.

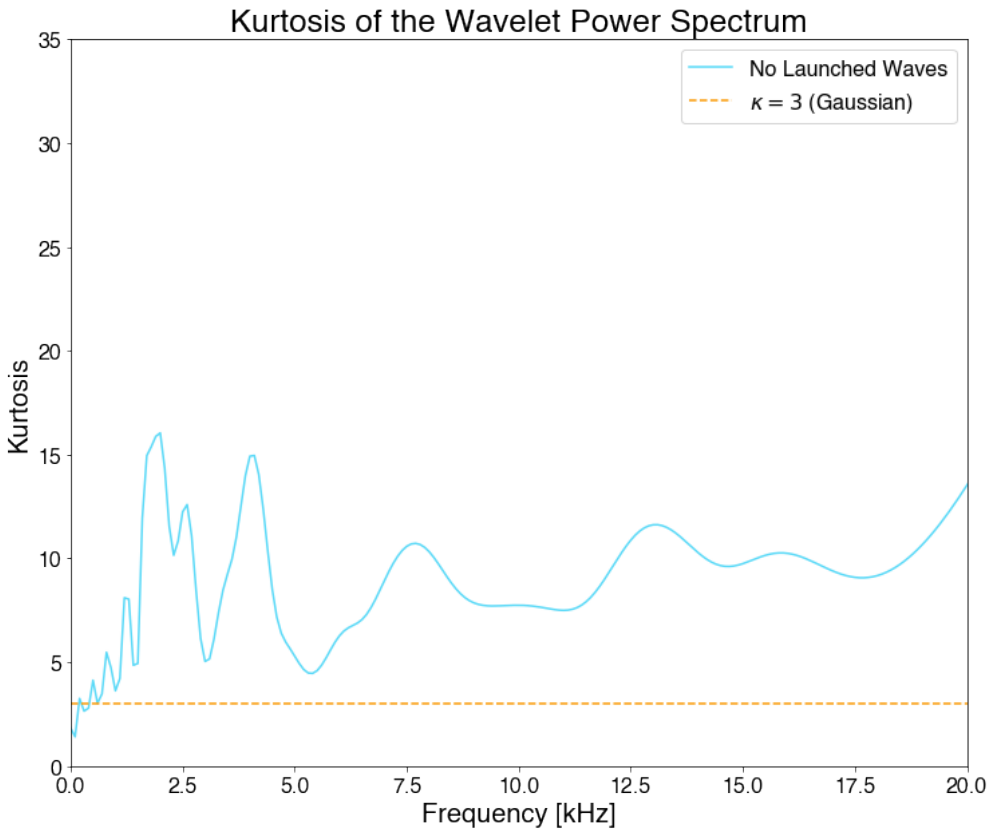

Figure 4.4: Kurtosis as a function of frequency for the baseline plasma. Note that the kurtosis is greater than 3 for all frequencies outside the cone of influence; the lowest frequencies (≤400 Hz) are within the cone of influence of the wavelet transform boundary and should be disregarded.

4.2 Increasing Fluctuation Power

Now that we have characterized the power spectrum of the baseline turbulence, we can investigate how that spectrum changes under feedback or when coherent tones are driven in the plasma. During amplifying feedback, both the wavelet and ensemble averaged Fourier power spectra show an increase in fluctuation power in the 1-12 kHz range (Figures 4.5 and 4.6 (left); compare to Figures 4.1 & 4.2). However, adding power to a broadband range of frequencies does not alter the intermittency of the power at all of those frequencies. Rather, those frequencies which see a significant increase in power under feedback see their intermittency reduced, as measured by the kurtosis (Figure 4.6).

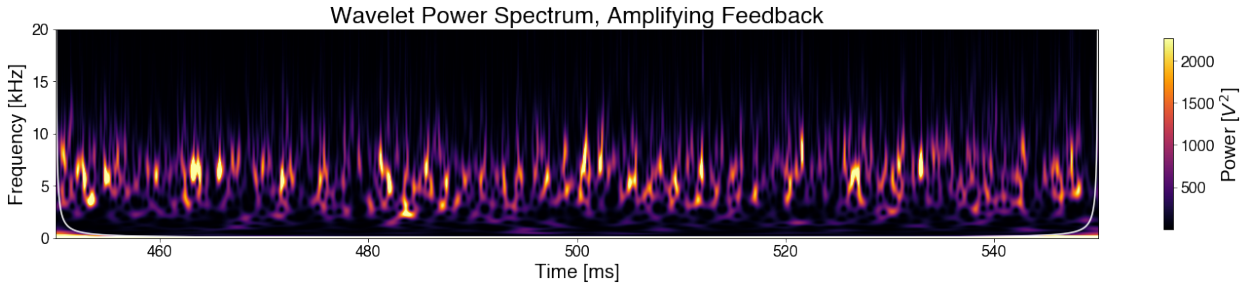

Figure 4.5: Wavelet power spectrum during amplifying feedback.

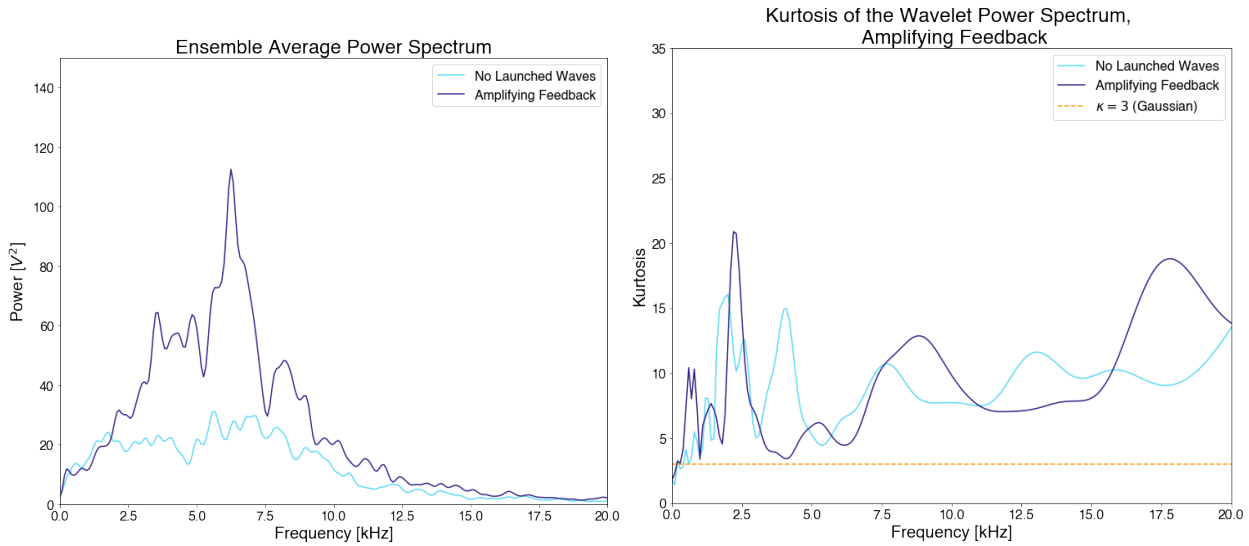

Figure 4.6: Ensemble averaged Fourier power spectrum (left) and kurtosis of the wavelet power spectrum as a function of frequency (right) for both the baseline and amplified turbulence. Note that the intermittency is reduced in the frequency range where the fluctuation power is most amplified.

Driving waves at a specific frequency using both bias probes also increases the peak power in both the wavelet (Figure 4.7) and Fourier (Figure 4.8, top) power spectra. In particular, driving a tone at 5 kHz creates peaks in the wavelet power spectrum which are comparable in amplitude to those created by amplifying feedback. Both the 5 kHz drive and amplifying feedback increase the total power in the potential fluctuations by a factor of 2, though the distribution of that power across frequencies is quite different.

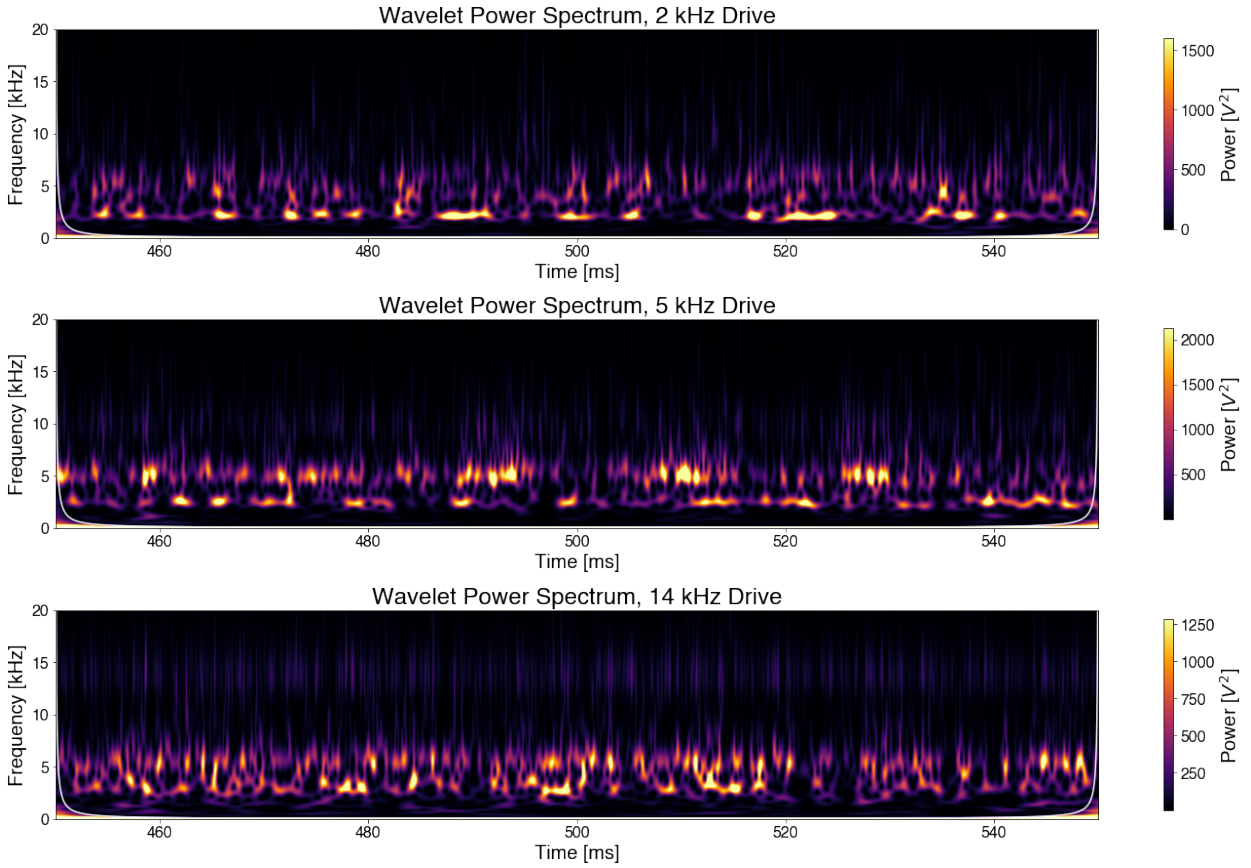

Figure 4.7: Wavelet power spectra for 2 (top), 5 (center), and 14 (bottom) kHz drives. Color bars are different for each sub-figure to ensure features of each are visible.

Additionally, driving a single coherent tone not only increases the power at that frequency, but also at harmonics of the driven frequency. This is clearest for the 5 kHz drive, where the half-harmonic (2.5 kHz), first harmonic (10 kHz), and second harmonic (15 kHz) are all visible; both 2 and 14 kHz drives show increases in power at their respective first and second harmonics (Figure 4.8). This is not particularly surprising, as it is well established that sinusoidal inputs to a nonlinear system can generate harmonics and subharmonics [85].

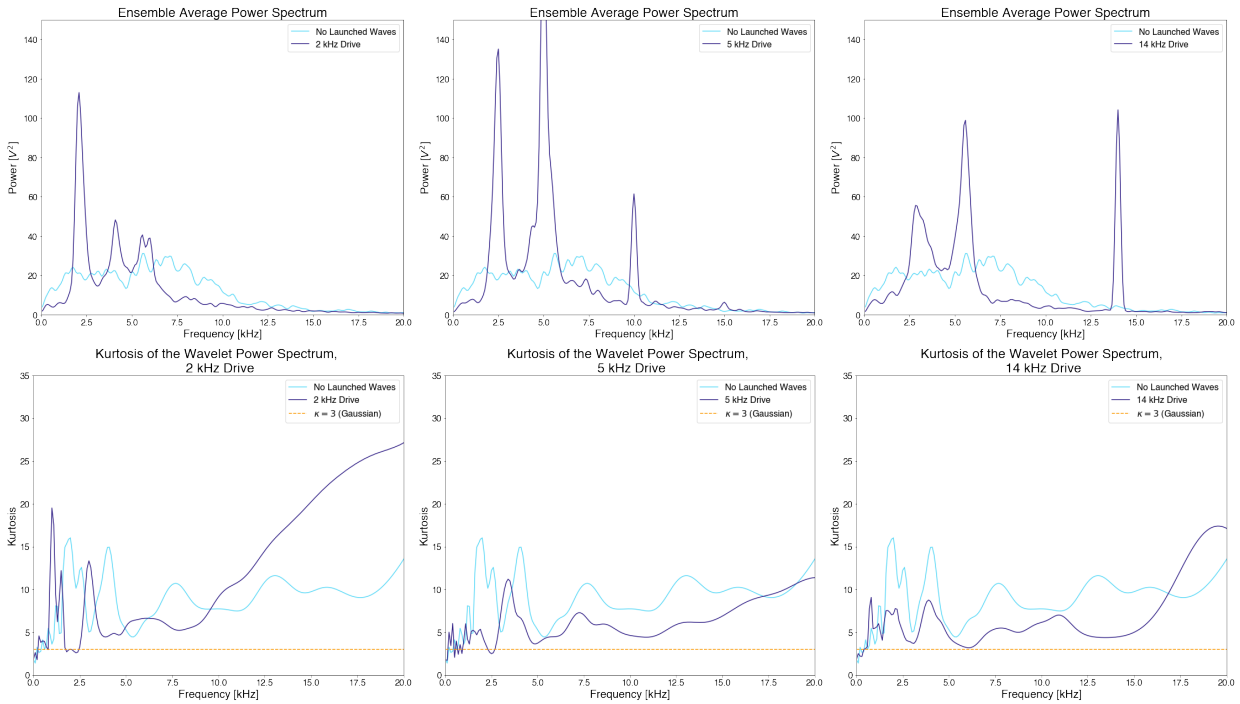

Figure 4.8: Fourier power spectra (top) and kurtosis as a function of frequency (bottom) for 2 kHz (left), 5 kHz (center) and 14 kHz (right) drives.

In contrast to the amplifying feedback, driving coherent waves into the plasma decreases the intermittency of the fluctuations at a broad range of frequencies, particularly if the drive is at or above the injection scale (5 kHz) (Figure 4.8, bottom). When the drive is below the injection scale (e.g. at 2 kHz), the intermittency of the fluctuations above 10 kHz increases rapidly. Additionally, the driven waves at 5 and 14 kHz each introduce of a small region in frequency space around their half harmonic where the power is approximately distributed as a Gaussian, rather than being intermittent. A 2 kHz driven tone also creates this region of near-Gaussianity, but at the driven frequency.

4.3 Reducing Fluctuation Power

Just as we can amplify the power in our turbulent fluctuations, we can also reduce the fluctuation power. This can be accomplished using either suppressing feedback or by driving two waves into the plasma simultaneously, one at 5 kHz and one at another frequency (Figures 4.9 and 4.10

top). Driving waves at two frequencies reduces the total power in the fluctuations by a factor of 2, while suppressing feedback reduces the fluctuation power by a factor of 1.4.

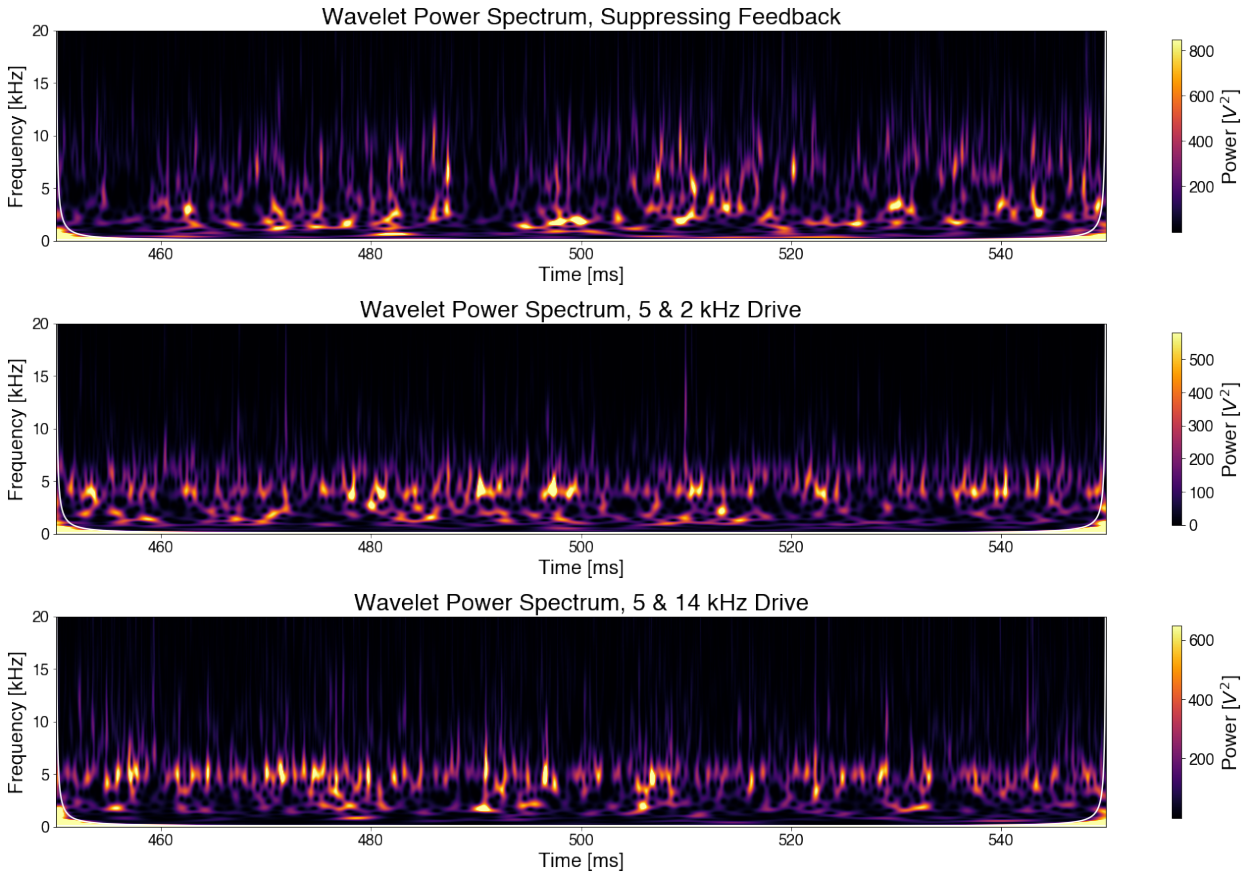

Figure 4.9: Wavelet power spectra during suppressing feedback (top) and drives of 5 & 2 kHz (center) and 5 & 14 kHz (bottom). Color bars are different for each sub-figure to ensure features of each are visible.

Again, the application of feedback alters the intermittency of the power spectrum in a frequency-dependent way, increasing intermittency at frequencies which are most suppressed (Figure 4.10, left). Driving waves at 5 & 14 kHz sharply reduces intermittency between $\sim 2 - 5$ kHz and increases intermittency at higher frequencies, exhibiting a pattern somewhat similar to the case of suppressing feedback. Driving waves at 5 & 2 kHz presents a particularly interesting change to the kurtosis, where intermittency is somewhat reduced below 8 kHz, but drastically increased above 8 kHz.

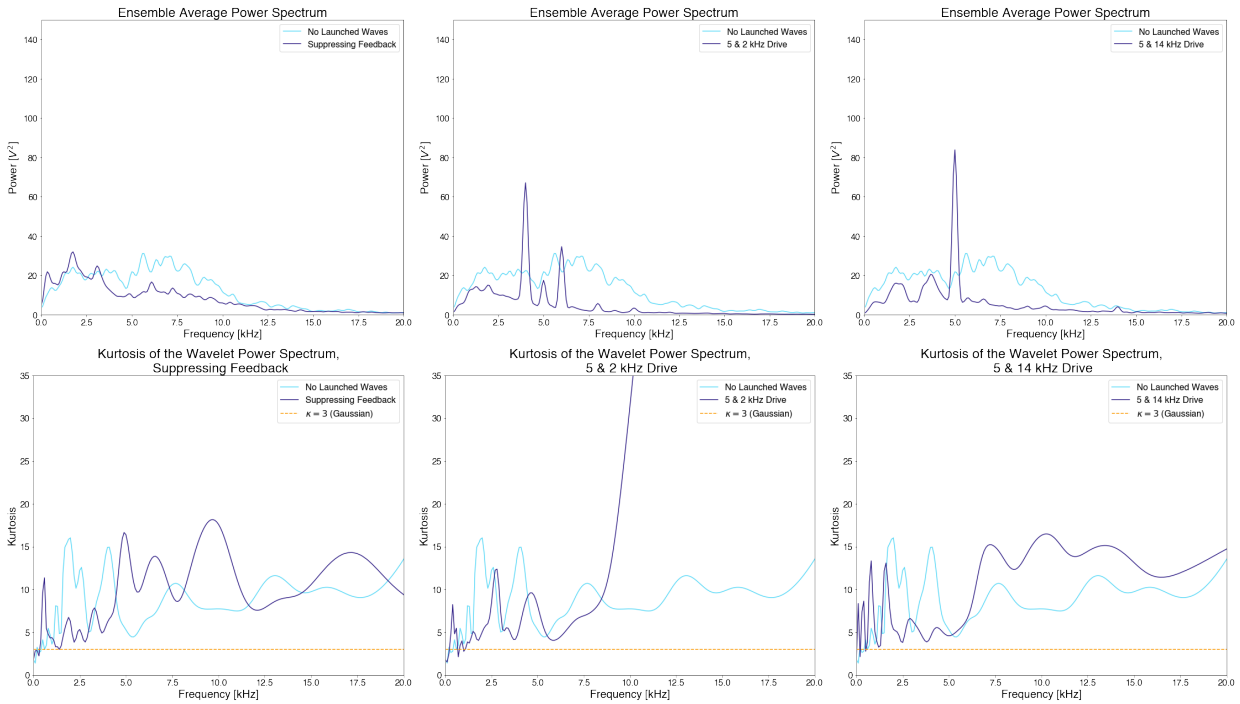

Figure 4.10: Ensemble averaged Fourier power spectra (top) and kurtosis as a function of frequency (bottom) for suppressing feedback (left), drives of 5 & 2 kHz (center), and drives of 5 & 14 kHz (right).

4.4 Wave Injection Modulated by Linear Interference Effects

Looking at the wavelet power spectra when coherent tones are being driven into the plasma, we see that even with constant driving power, that power is not constantly deposited into the fluctuations at the driven frequency (Figure 4.7). In particular, when a 5 kHz wave is driven, there appears to be a periodicity to the amplitude changes of fluctuations near 5 kHz. This periodicity is easily recreated by the superposition of three in-phase sinusoids at 4.94, 5.00, and 5.06 kHz with additive Gaussian noise of 5x greater amplitude. Thus, we see that linear interference effects can have a substantial impact on the temporal distribution of power at a given frequency.

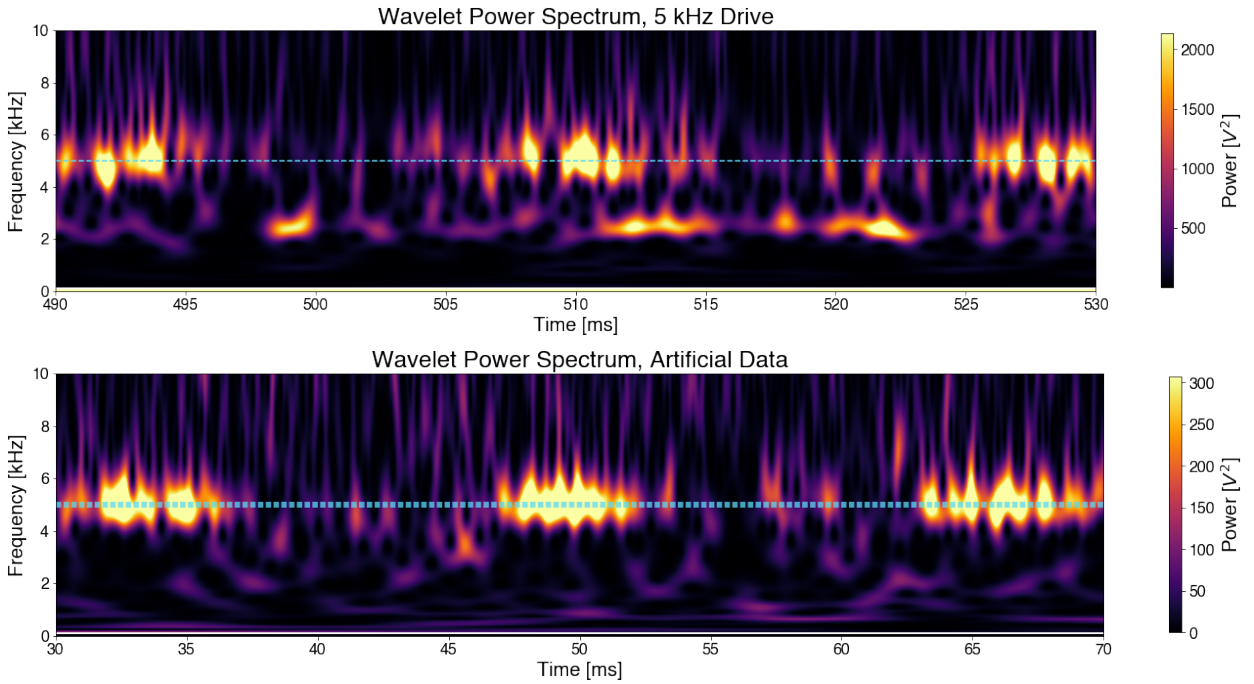

Figure 4.11: Comparison of the wavelet power spectra for a plasma with 5 kHz drive (top) and three in-phase waves separated by 60 Hz with additive Gaussian noise (bottom). The envelope structure visible in the 5 kHz drive is recreated quite well by the artificial data.

This linear combination of interferring waves and Gaussian noise also leads to a kurtosis profile that is remarkably similar to that of the observed turbulence with a 5 kHz drive, showing a decrease around 5 kHz and a fairly steady increase at higher frequencies. This implies that linear effects can create intermittent power spectra which are nearly indistinguishable from turbulent, nonlinearly driven systems. To determine whether nonlinear interactions are governing the power spectrum, higher order quantities, such as the bispectrum, must be invoked.

4.5 Summary

In this chapter, we present the first study of the intermittency of the fluctuation power spectrum in electrostatic dipole plasma turbulence. Using the wavelet transform, the fluctuation power can be simultaneously resolved as a function of time for a large number of frequency bands. A histogram of the wave power in each frequency band is used to construct the probability distribution function for those frequencies, which are well-approximated by a Gamma distribution and

have large kurtosis which increases with frequency, satisfying both definitions of intermittency. When feedback is used to amplify or suppress waves, the intermittency of amplified frequencies is reduced, while the intermittency of suppressed frequencies is enhanced. Driving a single wave at or above the injection scale has similar effects to amplifying feedback, while driving multiple waves has similar effects to suppressing feedback. Driving a wave below the injection scale of the turbulence increases the intermittency of the fluctuations above $\sim$ 8 kHz, whether that wave is driven singly or with another wave. Finally, artificial data from three interferring waves close in frequency is used to re-create the envelope effect seen when a 5 kHz wave is driven in the plasma, demonstrating that linear interferrence effects can generate spectra with statistics similar to those found in turbulent plasmas.

The power transferred between fluctuations via three-wave coupling can be studied using the bispectrum. We find that the summed wavelet bispectrum is always intermittent, even more so than the power spectrum. This indicates that the nonlinear transfer of energy between fluctuations is not continuous but occurs in bursts, analogous to the bursts of radial particle flux which have been observed on many experiments. The intermittency of the power transfer is reduced by feedback and by driving waves at or above the injection scale; if a wave is driven beloThe amount of power transferred tends to increase or decrease with the amount of power present in the coupled fluctuations, indicating that three-wave coupling is playing an important role in the dynamics of the system.

Chapter 5: Study of Power Transfer via Three Wave Coupling

Just as the previous chapter studied the temporal behavior of the fluctuation power under a variety of conditions, this chapter will apply a similar analysis to the summed wavelet bispectrum to characterize the power transfer via three wave coupling. While an understanding of the three-wave coupling coefficients is not available without a more detailed physical model of the system, the intensity of the power transfer via this three-wave coupling can nevertheless be characterized by the bispectrum. The summed bispectrum will be large when there is sufficient power in fluctuations which satisfy the three-wave frequency matching condition given in Equation 3.7, and small when the matching condition is not met or there is little power in the fluctuations. In this chapter, we show that the internittency of the power transefer via three-wave coupling, as quantified by the kurtosis of the amplitude of the summed wavelet bispectrum, is greater than the intermittency of the power itself (which was characterized in Chapter 4). We also show that the intermittency of the summed bispectrum generally decreases when fluctuations are launched into the plasma, whether as active feedback or coherent waves. These observations lead us to conclude that, under the conditions studied, the rate of wave-wave power transfer is not constant.

This chapter begins by describing the summed wavelet bispectrum of the baseline turbulence in CTX, then characterizes the effects of feedback and driven waves.

5.1 Power Transfer via Three-Wave Coupling in Fully Developed Turbulence

We begin by studying the wavelet bispectrum over the same $470 - 530$ ms time window used for the wavelet power spectrum, and compare the two quantities in Figure 5.1. Note the general correspondence between features in the two plots, such as those enclosed in the cyan boxes - more power being present in a frequency means that there is more power to transfer into or out of that

frequency.

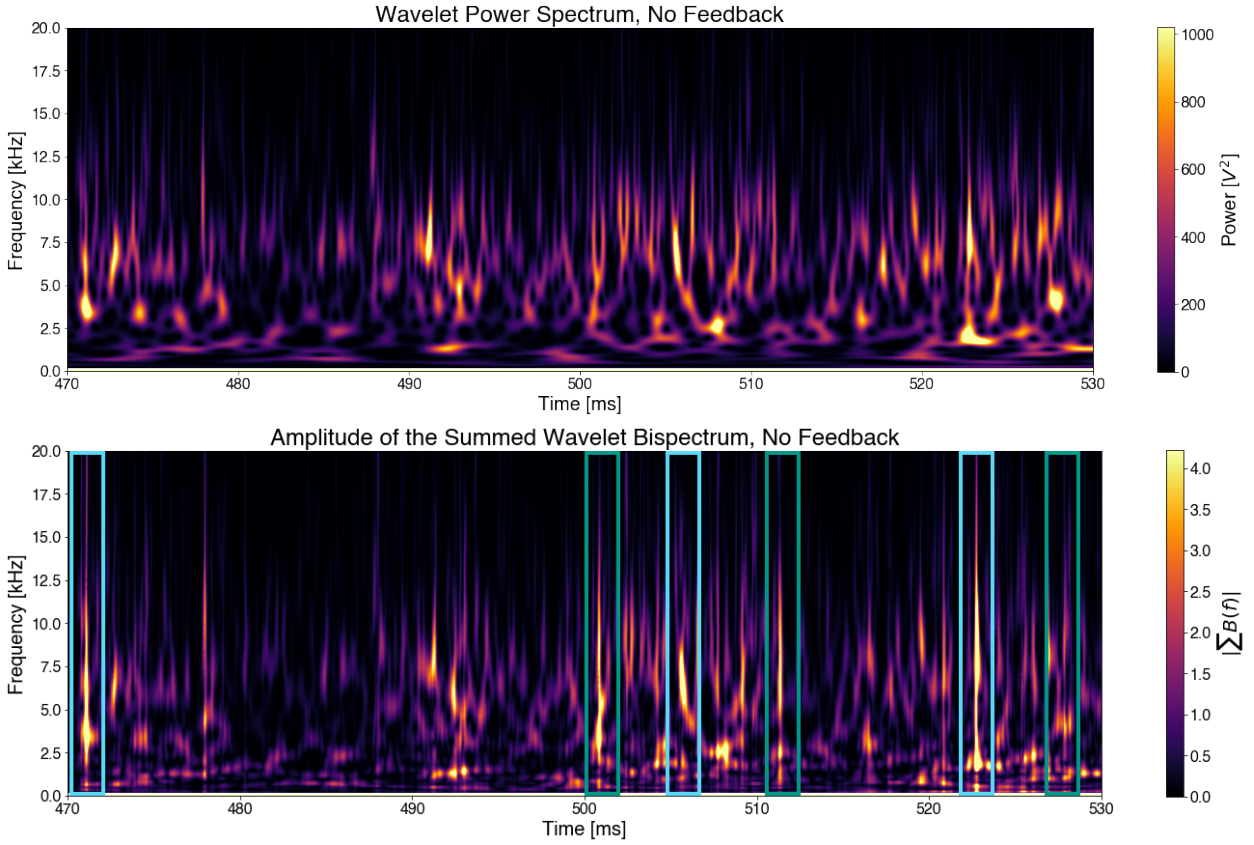

Figure 5.1: Wavelet power spectrum (top) and amplitude of the summed wavelet bispectrum (bottom) for the baseline turbulence. Note that many features from the power spectrum reappear in the bispectrum (cyan boxes), but some do not (green boxes).

However, the correspondence between peaks in the wavelet power spectrum and summed wavelet bispectrum is not one-to-one. At some times, the summed bispectrum shows large intensity - indicating significant power transfer - despite not having a particularly strong peak in wave power. This is seen, for example, the two "bursts" of high bispectral amplitude highlighted in the first two green boxes in Figure 5.1. A contrasting example is the last green box in Figure 5.1 when the "burst" in wave spectral power at 4 kHz and 8 kHz is relatively large when, at the same time, the summed bispectrum is relatively less intense, indicating that the burst of power may be produced by a mechanism not captured by the bispectrum.

Turning our attention to intermittency, Figure 5.2 indicates that the summed bispectrum is more intermittent than the power spectrum, though it generally follows the same pattern. This

makes some intuitive sense, as the bispectrum has an additional degree of freedom due to the phase coupling. This additional degree of freedom is the reason the bispectrum can be more intermittent than the power spectrum. Changes in the phase coupling between fluctuations may not significantly alter the power spectrum if there is little power at the coupled frequences to begin with, or if the fluctuations are only weakly coupled. Nevertheless, if the bispectrum is in general more intermittent than the power spectrum in other turbulent systems, and thus the phase couplings themselves are more intermittent, the standard random phase approximation for treating turbulent wave couplings may break down.

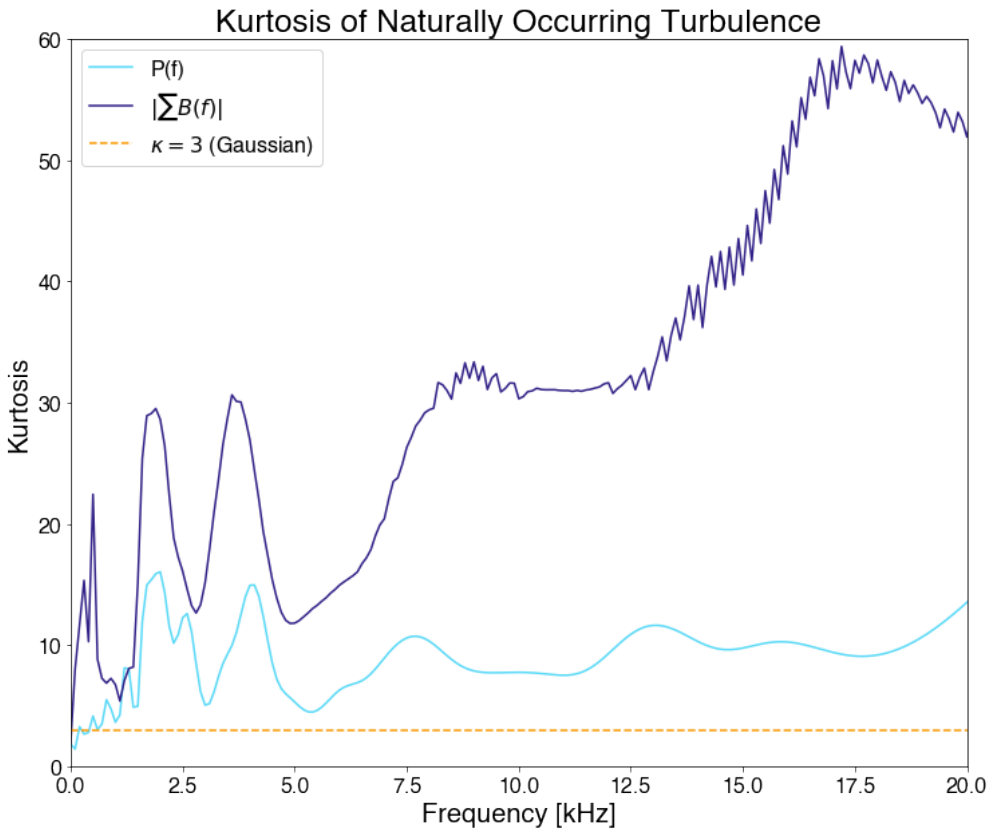

Figure 5.2: Comparison of the kurtosis as a function of frequency for the amplitude of the summed wavelet bispectrum and wavelet power spectrum during baseline electrostatic turbulence on CTX.

5.2 Effects of Feedback on Three-Wave Coupling

Just as we did for the baseline turbulence, we compare the wavelet power spectrum to the summed wavelet bispectrum for both amplifying (Figure 5.3) and suppressing (Figure 5.4) feed-

back. For this study, we trigger the feedback on and off to better illustrate how both the wavelet power spectrum and summed wavelet bispectrum change under feedback. Feedback is on from 500 – 520 ms for both amplifying and suppressing feedback. In both cases there is a marked change in both the power spectrum and summed bispectrum almost immediately when the feedback turns on, which disappears as soon as the feedback is turned off.

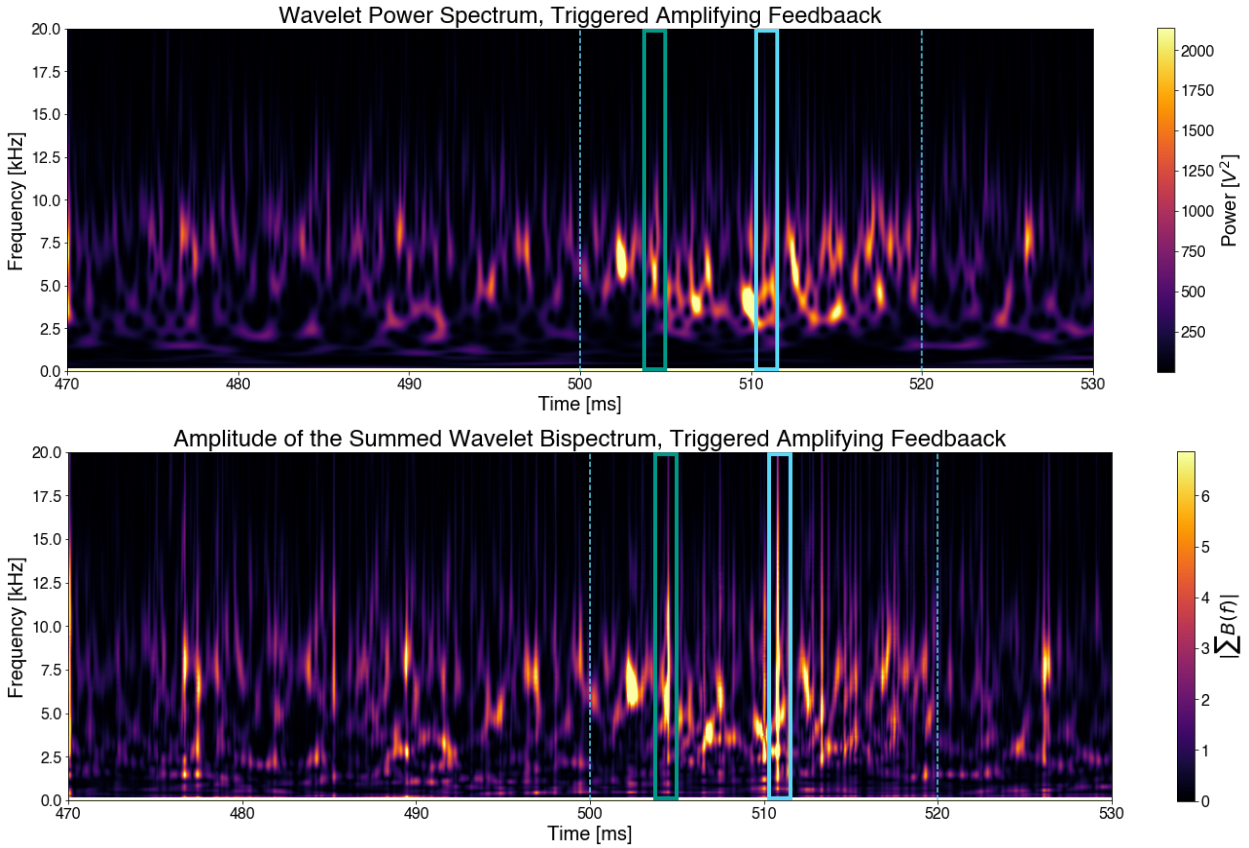

Figure 5.3: Wavelet power spectrum (top) and summed wavelet bispectrum (bottom) for amplifying feedback. Feedback is on for the 500-520 ms window. Note that the colorbars are different from those in Figures 5.1 and 5.4 to ensure features of each are visible.

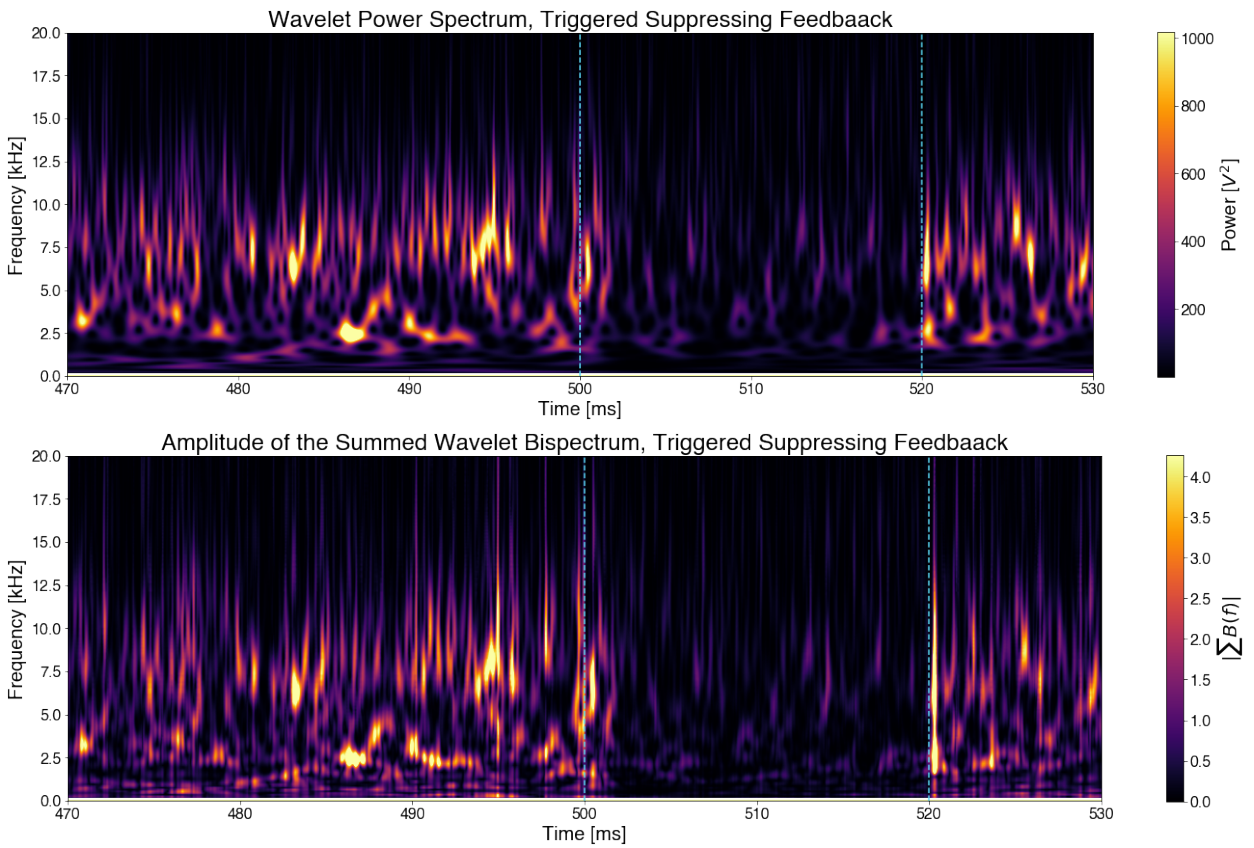

Figure 5.4: Wavelet power spectrum (top) and summed wavelet bispectrum (bottom) for suppressing feedback. Feedback is on for the 500-520 ms window.Note that the colorbars are different from those in Figures 5.1 and 5.3 to ensure features of each are visible.

Note the correspondence between the peaks of the summed wavelet bispectrum and the wavelet power spectrum for amplifying feedback, indicating that the waves which are most strongly coupled are receiving energy from the other fluctuations in the plasma. For example, the peak in both power and summed wavelet bispectrum in the green box corresponds with an increase in the bispectrum but not the power at many frequencies, suggesting those frequencies are giving up their power to the 7 kHz fluctuation at that time. Contrastingly, there are also moments of large bispectrum at many frequencies which do not appear to transfer power to a preferred frequency, such as the burst in the cyan box. Nearly all frequencies show a large bispectrum indicating power transfer is occurring, but the power spectrum at that time is unremarkable from many other times during amplifying feedback.

In the suppressing case, we note that having removed power from a broad range of fluctuations,

those fluctuations are no longer able to transfer much energy via three-wave coupling, and have consistently low bispectrum during feedback. Indeed, the most visible features in the suppressing case correspond to the rare instances of significant power being present in the fluctuations. Some instances of large summed wavelet bicoherence during suppressing feedback - such as the peak around 2 kHz at 506 ms - correspond to a distcint lack of power at that frequency and time in the wavelet power spectrum. Such a combination of high bispectrum and low power suggests that the wave is participating strongly in three-wave coupling, but that coupling is moving power out of that particular frequency. This is the other side of what happened during amplifying feedback, with many waves coupling to tranfer power into a specific frequency.

The correspondence of major features of the wavelet power spectra and wavelet bispectra during feedback suggest that three-wave coupling is an important mechanism by which this feedback modifies the turbulence.

As was shown in Figure 5.2, the summed bispectrum is consistently more intermittent than the power spectrum. This remains true during feedback, as can be seen in Figure 5.5. Electrostatic feedback decreases the kurtosis of the summed bispectrum across the frequency range of interest (Figure 5.6), in contrast to the more frequency-localized changes to the kurtosis of the power spectrum (Figures 4.6 and 4.10 left). This means that power is being transferred between waves more consistently during feedback than during the baseline fully-developed turbulence, further supporting the hypothesis that the feedback is acting on the plasma via three-wave coupling.

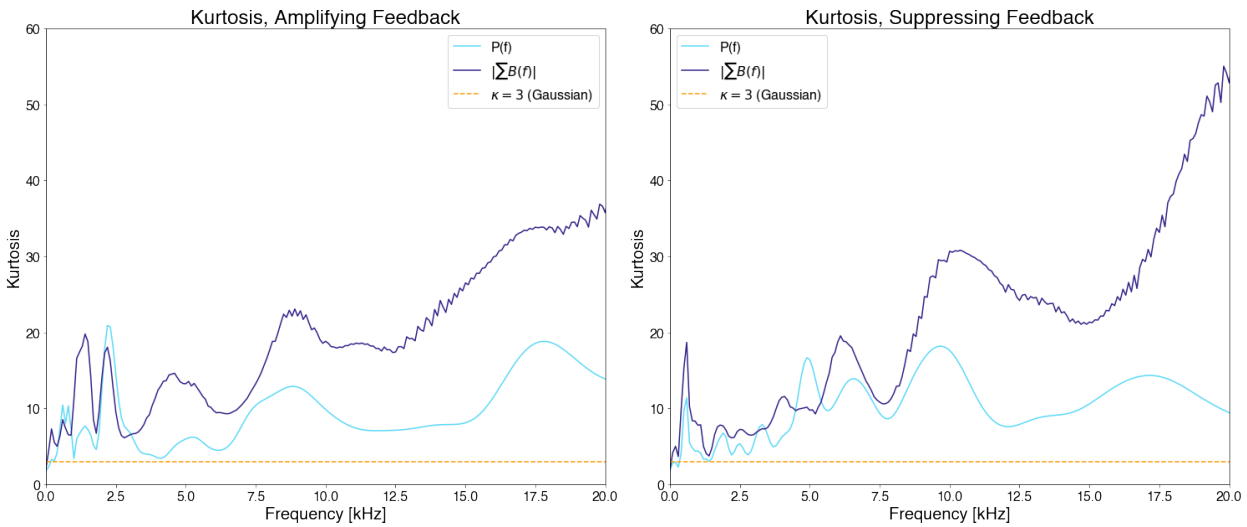

Figure 5.5: Comparison of the kurtosis as a function of frequency for the power spectrum and summed bispectrum during amplifying (left) and suppressing (right) feedback. The summed bispectrum is more intermittent than the power spectrum at most frequencies.

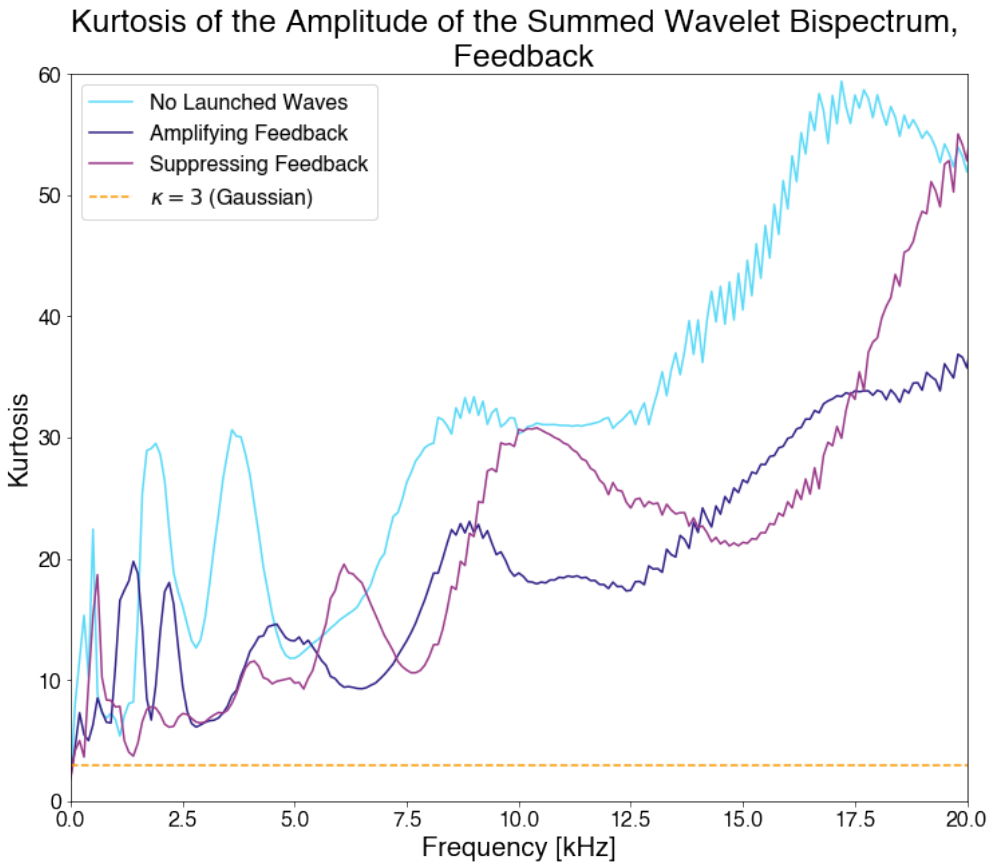

Figure 5.6: Comparison of the kurtosis as a function of frequency for plasmas with no feedback, amplifying feedback, and suppressing feedback. The baseline turbulence shows the most intermittency, while suppressing feedback shows the least.

5.3 Effects of Driven Waves on Three-Wave Coupling

Driving a coherent electrostatic wave in the plasma alters the natural exchange of energy between coupled frequnencies. In particular, driven waves primarily exchange energy with their own harmonics, as can be seen in Figure 5.7. (Note that this is likely because when a wave is launched at frequency f, a weaker wave is also launched in phase at $2f$ due to the nonlinearity of the probe sheath.) In these Fourier bispectrum plots, vertical and horizontal lines indicate a constant "parent" frequency (f_1 or f_2), while diagonal lines indicate a constant "child" frequency (f_3); all of these features are particularly visible in the 14 kHz drive case. It is important to remember that these plots do not tells us the direction of energy transfer between the three waves, only that a set of three waves is, on average, phase coupled and exchanging energy. However, when a wave is launched

into the plasma, the power must be transferred from the driven frequency into other fluctuations. Indeed, driving a wave at 5 kHz produces peaks in the summed bispectrum comparable to those produced by amplifying feedback, as can be seen in Figure 5.8. This indicates that a comparable amount of energy is being transferred into coupled waves by the 5 kHz drive as is transferred by amplifying feedback.

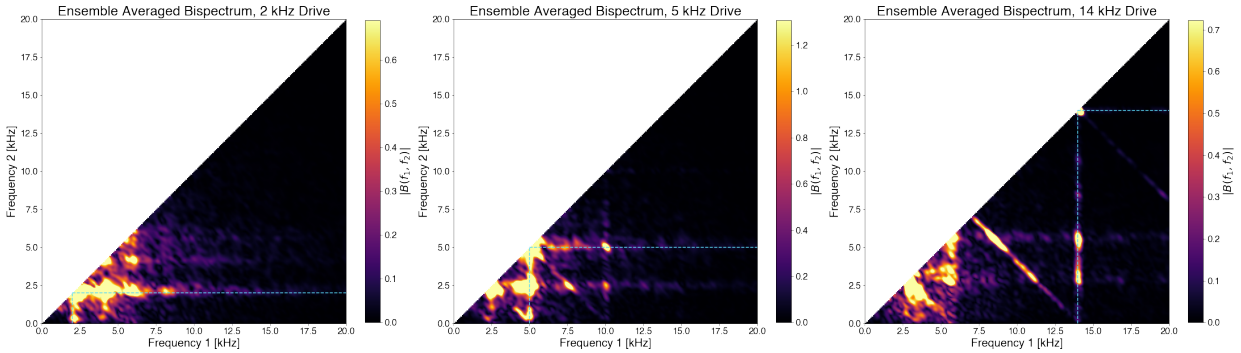

Figure 5.7: Fourier bispectrum for driven waves of 2 (left), 5 (center), and 14 (right) kHz. Note most significant power transfer is between the driven frequencies and their own harmonics, as well as the strongest features of the background turbulence near 5 and 2.5 kHz. Colorbars are different on each plot to preserve legibility of features.

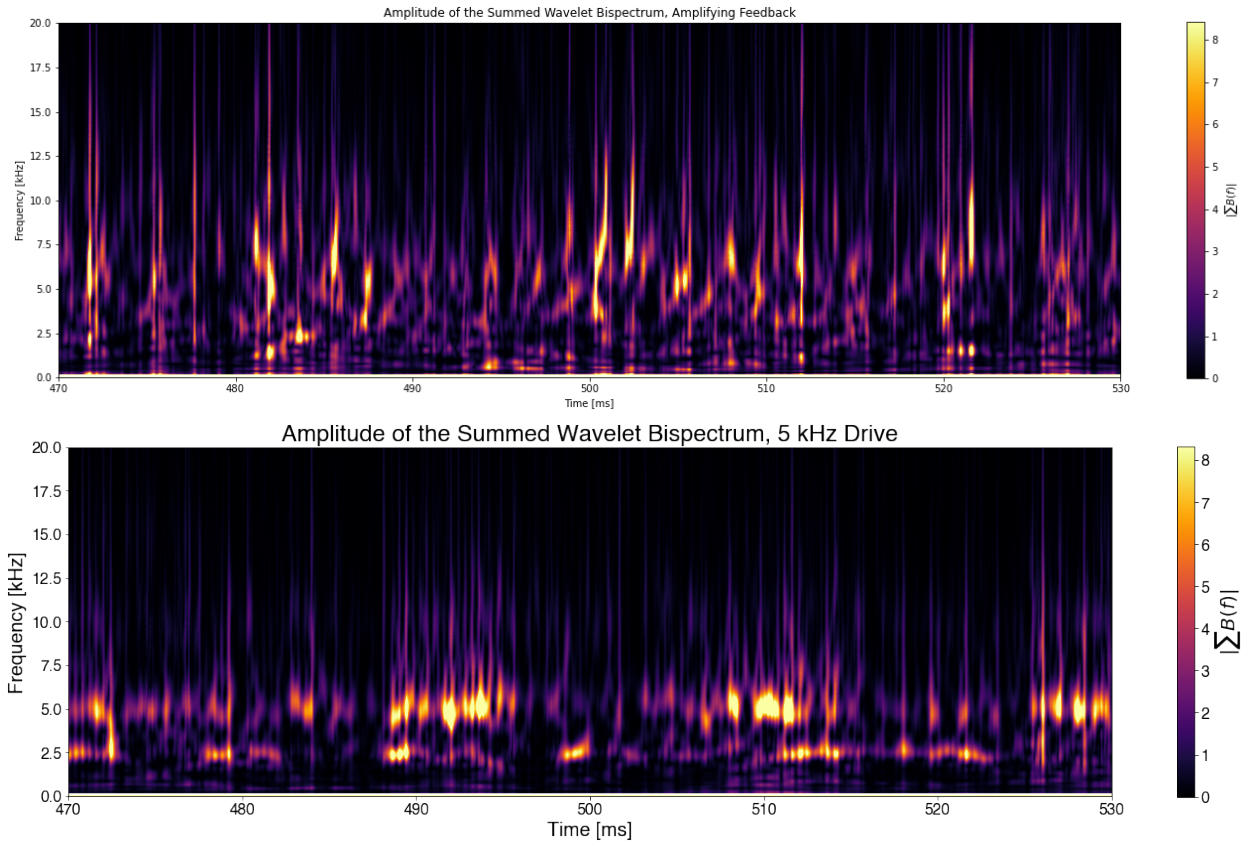

Figure 5.8: Amplitude of the summed wavelet bispectrum for plasmas modified by amplifying feedback (top) and a 5 kHz driven wave (bottom). Note that the colorbars are similar, indicating that the maximum power transferred via three wave coupling in each case is similar.

If we instead drive waves at two different frequencies, it does not necessarily mean that those frequencies will exchange energy any differently than they do when only one frequency is driven. Indeed, there appears to be no significant enhancement of the Fourier bispectrum between the two driven frequencies in either of the tested cases (Figure 5.9) when compared to the individual drives. Furthermore, when two waves are driven simultaneously, the bispectrum at all frequencies decreases - this is most evident for the 5 & 2 kHz case, where the entire colorbar has decreased by an order of magnitude and there is little interaction between the driven frequencies.

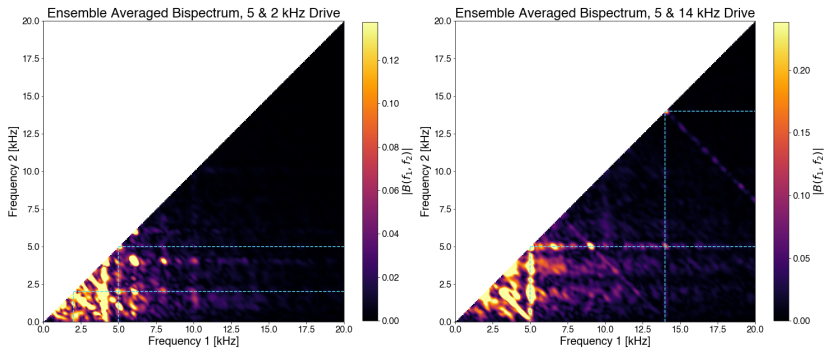

Figure 5.9: Fourier bispectrum for driven waves of 5 & 2 kHz (left) and 5 & 14 kHz (right). When compared to the bispectra for the individual drives in Figure5.7, the 5 & 2 kHz case indicates large reduction in phase coupling, while the 5 & 14 kHz case looks like a weaker superposition of the coupling when only one drive is present.REPHRASE

The intermittency of the amplitude of the summed wavelet bispectrum during drive shows similar reductions to the kurtosis as during feedback, as can been seen in Figure 5.10.

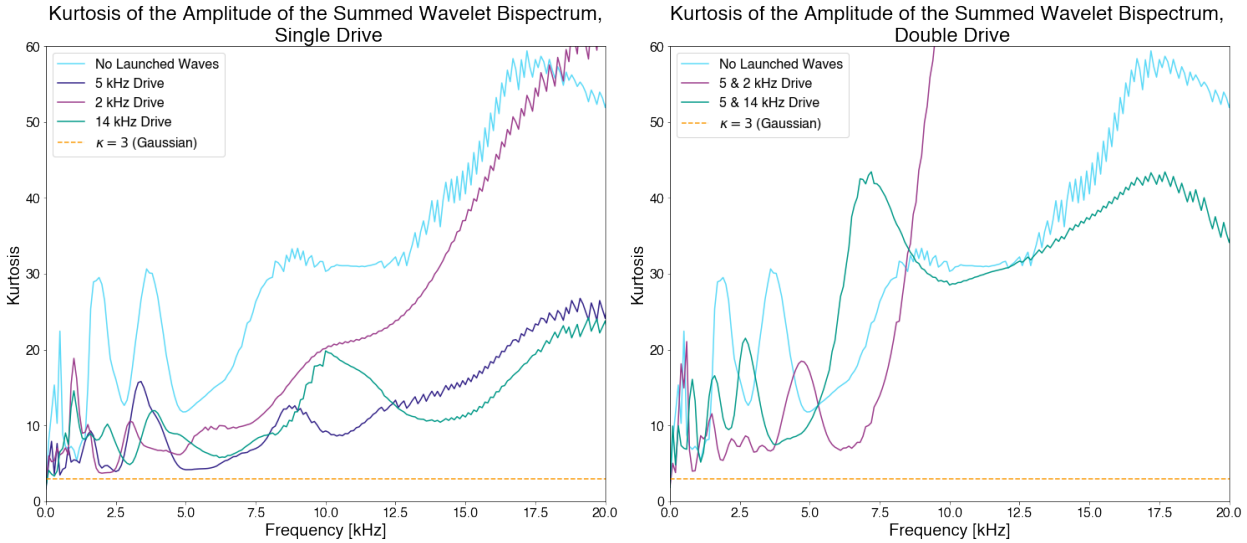

Figure 5.10: Kurtosis as a function of frequency for single (left) and double (right) drive cases. All drives reduce the intermittency of the fluctuations below $\sim$ 20 kHz.

5.4 Summary of Chapter 5

In this chapter, we demonstrate that the nonlinear transfer of power between fluctuations of different frequencies - as measured by the summed wavelet bispectrum - is always intermittent and exhibits non-Gaussian statistics. The degree of intermittency, as quantified by the kurtosis, is

greater than the intermittency in the wavelet power spectrum. The fact that the wave-wave power transfer is more "bursty" than the wave power itself is a consequence of the three-wave frequency matching requirement for power transfer to occur. Large bispectrum (significant power transfer) requires fluctuations to have both high power and match the three-wave resonance condition simultaneously.

We further show that amplifying feedback increases the power transferred and suppressing feedback decreases the power transferred, consistent with the respective changes to the power spectrum discussed in Chapter 4 and suggesting that three-wave coupling may play a role in how electrostatic feedback modifies the plasma. Although the overall magnitude of the power transferred via three-wave coupling increases with fluctuation power, launching waves into the plasma generally decreases the intermittency of this power transfer. Both feedback and driven waves reduce the intermittency of power transfer via three-wave coupling below $\sim$ 20 kHz. Finally, we show that even when two waves are strongly driven, they will not transfer significantly more energy than when a single wave is driven. Rather, because there is less power in the fluctuations overall, proportionately less energy is transferred, as is indicated by a reduction of the amplitude of the summed bispectrum.

Chapter 6: Conclusion and Summary

Plasma confined by a strong magnetic field exhibit low-frequency interchange and entropy mode turbulence that is responsible for the radial transport of heat and particles. Previous studies have shown that the turbulence in dipole-confined plasma consists of a broad spectrum of modes with chaotic phases and amplitudes. The ensemble averaged wave power spectrum has a power-law dependence consistent with a cascade of energy to both higher and lower frequencies. Measurements of particle flux shows the transport is highly intermittent, consisting of bursts of particles with non-Gaussian statistics and large kurtosis.

The research in this thesis builds upon earlier works and, for the first time, focuses on the statistics of the wave power and magnitude of the summed bispectrum, which is indicative of the power transfer between scales. The wavelet transform is used to calculate the frequency content of floating potential time series measured during fully developed steady state turbulence. The power at each frequency is found to vary rapidly in time and is statistically intermittent, having both a kurtosis greater than 3 at all frequencies and kurtosis increasing with frequency. Probability distribution functions for the power at each frequency are well approximated by a Gamma distribution.

Application of amplifying or suppressing feedback increases or reduces the power in the fluctuations; amplified fluctuations become less intermittent and suppressed fluctuations become more intermittent. Driving a single wave at or above the injection scale decreases the intermittency below $\sim$ 20 kHz, where the bulk of the fluctuation power is concentrated. Driving a wave at frequencies lower than the injection scale does not create this same reduction, and leads to a sharp increase in kurtosis above $\sim$ 10 kHz. Additionally, we have shown that periodic modulations of power at a given frequency are easily recreated by constructive interference with other waves which are close in frequency and generate spectra with statistics similar to those found in turbulent plasmas. This indicates that simple linear effects can significantly alter the time-evolution of the fluctuation

power spectrum.

Launching waves into the plasma as either active feedback or single frequencies reduces the intermittency of the power transfer between frequencies below $\sim$ 20 kHz. Driving two waves at or above the injection scale also reduces the intermittency of the power transfer. However, if one wave is driven at a frequency below the injection scale and the other at the injection scale, the intermittency of power transfer for fluctuations above $\sim$ 8 kHz is greatly increased, following a similar trend in the intermittency of the power spectrum. Strongly driving multiple waves cannot force them to exchange energy directly with each other.

Nonlinear wave interactions in plasma turbulence are complex, and there are a number of research opportunities which could follow from the work in this thesis to enhance our understanding. Numerical simulations have become an increasingly powerful tool for studying turbulence and have previously been used to compute the time-averaged particle and heat flux in dipole-confined plasmas [103, 104]; these simulations could also be used to characterize the turbulent wave spectrum. When simulations were compared to measurements of intermittent particle flux in the TJ-K torsatron under a similar wavelet analysis, experiment and simulation produced "remarkably similar" power spectra [105]. Additionally, analytic expressions for interchange-entropy mode turbulence for the conditions found in laboratory dipole experiments can be derived from the flux-tube averaged gyrofluid equations for entropy. Because the linear form of these equations were consistent with measurements of the radial particle flux as a function of both the plasma density and electron temperature profile [21], it is expected that the nonlinear estimates of wave-wave coupling may be consistent with the observations of this thesis.

Beyond the confines of dipole plasmas, there is a rich world of plasma turbulence to explore. The intermittency of the summed bispectrum being greater than the intermittency of the power spectrum could have implications for the validity of the random phase approximation commonly used in studies of turbulence; however, additional work is needed to determine whether this intermittency has a dynamical or statistical influence on the steady state turbulence. Studies of the intermittency of the bispectrum in other systems, particularly those exhibiting Alfvénic turbulence,

could indicate broader relevance of this result. Additionally, the linear interference effects demonstrated in this work tie in well with the work of Howes [106], who interprets spatially intermittent current sheets as the product of constructive interference between Alfvén waves and nonlinearly generated modes. With additional work, it is possible to determine whether the similarity of the turbulent data to the artificial interference pattern is merely coincidental or due to linear interferrence effects significantly altering the turbulent spectrum.

References

[1] B. Grierson, M. Mauel, M. Worstell, and M Klassen, "Transport induced by large scale convective structures in a dipole-confined plasma," *Physical review letters*, vol. 105, no. 20, p. 205 004, 2010.

[2] B. Grierson, M. Worstell, and M. Mauel, "Global and local characterization of turbulent and chaotic structures in a dipole-confined plasma," *Physics of Plasmas*, vol. 16, no. 5, p. 055 902, 2009.

[3] C. Torrence and G. P. Compo, "A practical guide to wavelet analysis," *Bulletin of the American Meteorological society*, vol. 79, no. 1, pp. 61–78, 1998.

[4] B. P. Van Milligen, C Hidalgo, and E Sanchez, "Nonlinear phenomena and intermittency in plasma turbulence," *Physical review letters*, vol. 74, no. 3, p. 395, 1995.

[5] T. Roberts, M. Mauel, and M. Worstell, "Local regulation of interchange turbulence in a dipole-confined plasma torus using current-collection feedback," *Physics of Plasmas*, vol. 22, no. 5, p. 055 702, 2015.

[6] M. G. Kivelson, M. G. Kivelson, and C. T. Russell, *Introduction to Space Physics*. Cambridge university press, 1995.

[7] K Rypdal and T. Brundtland, "The birkeland terrella experiments and their importance for the modern synergy of laboratory and space plasma physics," *Le Journal de Physique IV*, vol. 7, no. C4, pp. C4–113, 1997.

[8] A. Boxer, R Bergmann, J. Ellsworth, D. Garnier, J Kesner, M. Mauel, and P Woskov, "Turbulent inward pinch of plasma confined by a levitated dipole magnet," *Nature Physics*, vol. 6, no. 3, pp. 207–212, 2010.

[9] M. S. Davis, M. Mauel, D. T. Garnier, and J. Kesner, "Pressure profiles of plasmas confined in the field of a magnetic dipole," *Plasma Physics and Controlled Fusion*, vol. 56, no. 9, p. 095 021, 2014.

[10] H Saitoh, Z Yoshida, J Morikawa, Y Yano, T Mizushima, Y Ogawa, M Furukawa, Y Kawai, K Harima, Y Kawazura, *et al.*, "High-β plasma formation and observation of peaked density profile in rt-1," *Nuclear Fusion*, vol. 51, no. 6, p. 063 034, 2011.

[11] H Saitoh, Z Yoshida, J Morikawa, Y Yano, H Mikami, N Kasaoka, and W Sakamoto, "Observation of magnetic fluctuations and rapid density decay of magnetospheric plasma in ring trap 1," *Physics of Plasmas*, vol. 19, no. 6, p. 064 502, 2012.

[12] H. Warren and M. Mauel, "Observation of chaotic particle transport induced by drift-resonant fluctuations in a magnetic dipole field," *Physical review letters*, vol. 74, no. 8, p. 1351, 1995.

[13] B. Levitt, D. Maslovsky, and M. E. Mauel, "Measurement of the global structure of interchange modes driven by energetic electrons trapped in a magnetic dipole," *Physics of Plasmas*, vol. 9, no. 6, pp. 2507–2517, 2002.

[14] B Levitt, D Maslovsky, M. Mauel, and J Waksman, "Excitation of the centrifugally driven interchange instability in a plasma confined by a magnetic dipole," *Physics of plasmas*, vol. 12, no. 5, p. 055 703, 2005.

[15] M. E. Mauel, "Laboratory observations of wave-induced radial transport within an" artificial radiation belt"," *Le Journal de Physique IV*, vol. 7, no. C4, pp. C4–307, 1997.

[16] M. E. Brown and A. H. Bouchez, "The response of jupiter's magnetosphere to an outburst on io," *Science*, vol. 278, no. 5336, pp. 268–271, 1997.

[17] N André, A. Persoon, J Goldstein, J. Burch, P Louarn, G. Lewis, A. Rymer, A. Coates, W. Kurth, E. Sittler, *et al.*, "Magnetic signatures of plasma-depleted flux tubes in the saturnian inner magnetosphere," *Geophysical Research Letters*, vol. 34, no. 14, 2007.

[18] F. Darrouzet, D. L. Gallagher, N. André, D. L. Carpenter, I. Dandouras, P. M. Décréau, J. De Keyser, R. E. Denton, J. C. Foster, J. Goldstein, *et al.*, "Plasmaspheric density structures and dynamics: Properties observed by the cluster and image missions," *Space Science Reviews*, vol. 145, no. 1-2, pp. 55–106, 2009.

[19] M Peret, N Fedorczak, P Tamain, P. Ghendrih, L Vermare, T. Supra, and W. Teams, "A spectral model for interchange transport in tokamak scrape-off layers," *Nuclear Fusion*, vol. 61, no. 4, p. 046 045, 2021.

[20] S. Sugita, M. Yagi, S.-I. Itoh, and K. Itoh, "Interchange turbulence and radial transport in tokamak scrape-off layer dominated by meso scale structure," *Journal of the Physical Society of Japan*, vol. 79, no. 4, p. 044 502, 2010.

[21] D. Garnier, M. Mauel, T. Roberts, J Kesner, and P. Woskov, "Turbulent fluctuations during pellet injection into a dipole confined plasma torus," *Physics of Plasmas*, vol. 24, no. 1, p. 012 506, 2017.

[22] T. Pierre, A Escarguel, D Guyomarc'h, R Barni, and C Riccardi, "Radial convection of plasma structures in a turbulent rotating magnetized-plasma column," *Physical review letters*, vol. 92, no. 6, p. 065 004, 2004.

[23] D. J. Southwood and M. G. Kivelson, "Magnetospheric interchange motions," *Journal of Geophysical Research: Space Physics*, vol. 94, no. A1, pp. 299–308, 1989.

[24] C. Russell, D. Huddleston, K. Khurana, and M. Kivelson, "Observations at the inner edge of the jovian current sheet: Evidence for a dynamic magnetosphere," *Planetary and space science*, vol. 47, no. 3-4, pp. 521–527, 1999.

[25] D. D'ippolito, J. Myra, and S. Zweben, "Convective transport by intermittent blob-filaments: Comparison of theory and experiment," *Physics of Plasmas*, vol. 18, no. 6, p. 060 501, 2011.

[26] J. P. Freidberg, *ideal MHD*. Cambridge University Press, 2014.

[27] J. D. Jackson, *Classical electrodynamics*. American Association of Physics Teachers, 1999.

[28] M. N. Rosenbluth and C. Longmire, "Stability of plasmas confined by magnetic fields," *Annals of Physics*, vol. 1, no. 2, pp. 120–140, 1957.

[29] T. M. Roberts, "Local regulation of interchange turbulence in a dipole-confined plasma torus using current injection feedback," PhD thesis, Columbia University, 2015.

[30] D. Melrose, "Rotational effects on the distribution of thermal plasma in the magnetosphere of jupiter," *Planetary and Space Science*, vol. 15, no. 2, pp. 381–393, 1967.

[31] M. Mauel, D. Garnier, M. Roberts, and J. Kesner, "Toroidal confinement without parallel current: Interchange and entropy modes in a warm electron dipole plasma," in *Presentation to 2015 Sherwood Fusion Theory Conference (NYU, 2015, http://www. networkingworlds. com/sherwood2015/proceedings. php)*, 2015.

[32] D. J. Griffiths, *Introduction to Electrodynamics*. Prentice Hall, 1962.

[33] P. R. Julian, W. M. Washington, L. Hembree, and C. Ridley, "On the spectral distribution of large-scale atmospheric kinetic energy," *Journal of Atmospheric Sciences*, vol. 27, no. 3, pp. 376–387, 1970.

[34] U. Frisch and A. N. Kolmogorov, *Turbulence: the legacy of AN Kolmogorov*. Cambridge university press, 1995.

[35] S. Zweben, J. Boedo, O Grulke, C Hidalgo, B LaBombard, R. Maqueda, P Scarin, and J. Terry, "Edge turbulence measurements in toroidal fusion devices," *Plasma Physics and Controlled Fusion*, vol. 49, no. 7, S1, 2007.

[36] K Rypdal and S Ratynskaia, "Onset of turbulence and profile resilience in the helimak configuration," *Physical review letters*, vol. 94, no. 22, p. 225 002, 2005.

[37] F. Poli, S Brunner, A Diallo, A Fasoli, I Furno, B Labit, S. Müller, G Plyushchev, and M Podestà, "Experimental characterization of drift-interchange instabilities in a simple toroidal plasma," *Physics of Plasmas*, vol. 13, no. 10, p. 102 104, 2006.

[38] M. Burin, G. Tynan, G. Antar, N. Crocker, and C Holland, "On the transition to drift turbulence in a magnetized plasma column," *Physics of Plasmas*, vol. 12, no. 5, p. 052 320, 2005.

[39] P. K. Kundu and I. M. Cohen, *Fluid Mechanics, 3rd Edition*. Elsevier, 2004.

[40] L. Landau and E. Lifshitz, "Fluid mechanics. translated from the russian by jb sykes and wh reid," *Course of Theoretical Physics*, vol. 6, 1987.

[41] A. N. Kolmogorov, "The local structure of turbulence in incompressible viscous fluid for very large reynolds numbers," *Cr Acad. Sci. URSS*, vol. 30, pp. 301–305, 1941.

[42] R. H. Kraichnan, "Inertial ranges in two-dimensional turbulence," *The Physics of Fluids*, vol. 10, no. 7, pp. 1417–1423, 1967.

[43] R. H. Kraichnan and D. Montgomery, "Two-dimensional turbulence," *Reports on Progress in Physics*, vol. 43, no. 5, p. 547, 1980.

[44] T. Simonen, T. Chu, and H. Hendel, "Feedback control of collisional drift waves by modulated parallel-electron-current sink-experiment and interpretation," *Physical Review Letters*, vol. 23, no. 11, p. 568, 1969.

[45] A. Sen, "Control and diagnostic uses of feedback," *Physics of Plasmas*, vol. 7, no. 5, pp. 1759–1766, 2000.

[46] A. K. Sen, "Observability and controllability of plasma instabilities," *The Physics of Fluids*, vol. 18, no. 9, pp. 1187–1191, 1975.

[47] N Rath, S Angelini, J Bialek, P. Byrne, B DeBono, P Hughes, J. Levesque, M. Mauel, G. Navratil, Q Peng, *et al.*, "Adaptive control of rotating magnetic perturbations in hbt-ep using gpu processing," *Plasma Physics and Controlled Fusion*, vol. 55, no. 8, p. 084 003, 2013.

[48] A. J. Klein, D. A. Maurer, T. Sunn Pedersen, M. E. Mauel, G. A. Navratil, C. Cates, M. Shilov, Y. Liu, N. Stillits, and J. Bialek, "Suppression of rotating external kink instabilities using optimized mode control feedback," *Physics of Plasmas*, vol. 12, no. 4, p. 040 703, 2005.

[49] A. Garofalo, M. Chu, E. Fredrickson, M Gryaznevich, T. Jensen, L. Johnson, R. La Haye, G. Navratil, M Okabayashi, J. Scoville, *et al.*, "Resistive wall mode dynamics and active feedback control in diii-d," *Nuclear fusion*, vol. 41, no. 9, p. 1171, 2001.

[50] J. Hillesheim, W. Peebles, T. Carter, L Schmitz, and T. Rhodes, "Experimental investigation of geodesic acoustic mode spatial structure, intermittency, and interaction with turbulence in the diii-d tokamak," *Physics of Plasmas*, vol. 19, no. 2, p. 022 301, 2012.

[51] K. Gentle, "The texas experimental tokamak (text) facility user's facility," *Nuclear Technology-Fusion*, vol. 1, no. 4, pp. 479–485, 1981.

[52] T Uckan, B Richards, R. D. Bengtson, B. Carreras, G. Li, P. Hurwitz, W. Rowan, H. Tsui, and A. Wootton, "Plasma edge turbulence probing and feedback control and stabilization experiments," *Nuclear Fusion*, vol. 35, no. 4, p. 487, 1995.

[53] T Uckan, B Richards, A. Wootton, R. D. Bengtson, R Bravenec, B. Carreras, G. Li, P Hurwitz, P. Phillips, W. Rowan, *et al.*, "Feedback control and stabilization experiments on the texas experimental tokamak (text)," *Journal of Nuclear Materials*, vol. 220, pp. 663–667, 1995.

[54] R. Prater, "Feedback suppression of a large-growth-rate flute mode," *Physical Review Letters*, vol. 27, no. 3, p. 132, 1971.

[55] E. Novikov, "Intermittency and scale similarity in the structure of a turbulent flow," *Journal of Applied Mathematics and Mechanics*, vol. 35, no. 2, pp. 231–241, 1971.

[56] D. Jou, "Intermittent turbulence: A short introduction," *Scientia Marina*, vol. 61, pp. 57–62, 1997.

[57] W. H. Matthaeus, M. Wan, S. Servidio, A Greco, K. T. Osman, S. Oughton, and P. Dmitruk, "Intermittency, nonlinear dynamics and dissipation in the solar wind and astrophysical plasmas," *Philosophical Transactions of the Royal Society A: Mathematical, Physical and Engineering Sciences*, vol. 373, no. 2041, p. 20 140 154, 2015.

[58] R. H. Berman, D. J. Tetreault, and T. H. Dupree, "Simulation of phase space hole growth and the development of intermittent plasma turbulence," *The Physics of fluids*, vol. 28, no. 1, pp. 155–176, 1985.

[59] R. H. Berman, T. H. Dupree, and D. J. Tetreault, "Growth of nonlinear intermittent fluctuations in linearly stable and unstable simulation plasma," *The Physics of fluids*, vol. 29, no. 9, pp. 2860–2870, 1986.

[60] H. Warren, M. Mauel, D Brennan, and S Taromina, "Observation of wave-induced chaotic radial transport in a laboratory terrella experiment," *Physics of Plasmas*, vol. 3, no. 5, pp. 2143–2148, 1996.

[61] E. Yordanova, A. Vaivads, M. André, S. Buchert, and Z Vörös, "Magnetosheath plasma turbulence and its spatiotemporal evolution as observed by the cluster spacecraft," *Physical review letters*, vol. 100, no. 20, p. 205 003, 2008.

[62] V Angelopoulos, T Mukai, and S Kokubun, "Evidence for intermittency in earth's plasma sheet and implications for self-organized criticality," *Physics of Plasmas*, vol. 6, no. 11, pp. 4161–4168, 1999.

[63] M. Echim, H Lamy, and T Chang, "Multi-point observations of intermittency in the cusp regions," *Nonlinear Processes in Geophysics*, vol. 14, no. 4, pp. 525–534, 2007.

[64] V. Budaev, S. P. Savin, and L. M. Zelenyi, "Investigation of intermittency and generalized self-similarity of turbulent boundary layers in laboratory and magnetospheric plasmas: Towards a quantitative definition of plasma transport features," *Physics-Uspekhi*, vol. 54, no. 9, p. 875, 2011.

[65] C. Tao, F. Sahraoui, D. Fontaine, J. de Patoul, T. Chust, S. Kasahara, and A. Retino, "Properties of jupiter's magnetospheric turbulence observed by the galileo spacecraft," *Journal of Geophysical Research: Space Physics*, vol. 120, no. 4, pp. 2477–2493, 2015.

[66] R. Chhiber, A. Chasapis, R. Bandyopadhyay, T. Parashar, W. H. Matthaeus, B. Maruca, T. E. Moore, J. L. Burch, R. B. Torbert, C. T. Russell, *et al.*, "Higher-order turbulence statistics in the earth's magnetosheath and the solar wind using magnetospheric multiscale observations," *Journal of Geophysical Research: Space Physics*, vol. 123, no. 12, pp. 9941–9954, 2018.

[67] R Bruno, V Carbone, L. Sorriso-Valvo, and B Bavassano, "Radial evolution of solar wind intermittency in the inner heliosphere," *Journal of Geophysical Research: Space Physics*, vol. 108, no. A3, 2003.

[68] D. A. Schaffner, A Wan, and M. Brown, "Observation of turbulent intermittency scaling with magnetic helicity in an mhd plasma wind tunnel," *Physical review letters*, vol. 112, no. 16, p. 165 001, 2014.

[69] D. Toufen, F. Pereira, Z. Guimarães-Filho, I. Caldas, and K. Gentle, "Electrostatic turbulence intermittence driven by biasing in texas helimak," *Physics of Plasmas*, vol. 21, no. 12, p. 122 302, 2014.

[70] K Rypdal and S Ratynskaia, "Statistics of low-frequency plasma fluctuations in a simple magnetized torus," *Physics of Plasmas*, vol. 10, no. 7, pp. 2686–2695, 2003.

[71] J. A. Boedo, D Rudakov, R Moyer, S Krasheninnikov, D Whyte, G McKee, G Tynan, M Schaffer, P Stangeby, P. West, *et al.*, "Transport by intermittent convection in the boundary of the diii-d tokamak," *Physics of Plasmas*, vol. 8, no. 11, pp. 4826–4833, 2001.

[72] J. Boedo, "Edge turbulence and sol transport in tokamaks," *Journal of nuclear materials*, vol. 390, pp. 29–37, 2009.

[73] G. Kirnev, V. Budaev, S. Grashin, E. Gerasimov, and L. Khimchenko, "Intermittent transport in the plasma periphery of the t-10 tokamak," *Plasma physics and controlled fusion*, vol. 46, no. 4, p. 621, 2004.

[74] V. Sandborn, "Measurements of intermittency of turbulent motion in a boundary layer," *Journal of Fluid Mechanics*, vol. 6, no. 2, pp. 221–240, 1959.

[75] B. A. Grierson, "Interchange turbulence in a dipole-confined plasma," PhD thesis, Columbia University, 2009.

[76] B. J. Levitt, "Global mode analysis of centrifugal and curvature driven interchange instabilities," PhD thesis, Columbia University, 2004.

[77] A. F. Kuckes, "Interchange instability in a hot-electron plasma," *The Physics of Fluids*, vol. 9, no. 11, pp. 2239–2243, 1966.

[78] R. Dominguez and H. Berk, "Stability of interchange modes in a hot electron plasma," *The Physics of Fluids*, vol. 21, no. 5, pp. 827–834, 1978.

[79] L. Ferrari and A. Kuckes, "Instability in a hot electron plasma," *The Physics of Fluids*, vol. 8, no. 12, pp. 2295–2297, 1965.

[80] E. Ortiz, A. Boxer, J. Ellsworth, D. Garnier, A. Hansen, I Karim, J Kesner, and M. Mauel, "Effects of the hot electron interchange instability on plasma confined in a dipolar magnetic field," *Journal of fusion energy*, vol. 26, no. 1, pp. 139–144, 2007.

[81] R. J. Goldston, *Introduction to Plasma Physics*. CRC Press, 1995.

[82] N. A. Krall, "Stabilization of hot electron plasma by a cold background," *The Physics of Fluids*, vol. 9, no. 4, pp. 820–821, 1966.

[83] B. Van Milligen, E Sanchez, T Estrada, C Hidalgo, B. Brañas, B Carreras, and L. García, "Wavelet bicoherence: A new turbulence analysis tool," *Physics of Plasmas*, vol. 2, no. 8, pp. 3017–3032, 1995.

[84] T. D. De Wit, O. Alexandrova, I. Furno, L. Sorriso-Valvo, and G. Zimbardo, "Methods for characterising microphysical processes in plasmas," *Space Science Reviews*, vol. 178, no. 2-4, pp. 665–693, 2013.

[85] A. A. S. Choudhury, S. L. Shah, and N. F. Thornhill, *Diagnosis of process nonlinearities and valve stiction: data driven approaches*. Springer Science & Business Media, 2008.

[86] E. R. Kanasewich, *Time sequence analysis in geophysics*. University of Alberta, 1981.

[87] P. Welch, "The use of fast fourier transform for the estimation of power spectra: A method based on time averaging over short, modified periodograms," *IEEE Transactions on audio and electroacoustics*, vol. 15, no. 2, pp. 70–73, 1967.

[88] C. L. Nikias and J. M. Mendel, "Signal processing with higher-order spectra," *IEEE Signal processing magazine*, vol. 10, no. 3, pp. 10–37, 1993.

[89] Y. C. Kim and E. J. Powers, "Digital bispectral analysis and its applications to nonlinear wave interactions," *IEEE transactions on plasma science*, vol. 7, no. 2, pp. 120–131, 1979.

[90] C. L. Nikias and A. Petropulu, *Higher-order spectra analysis: A nonlinear signal processing framework*. PTR Prentice Hall, 1993.

[91] M. Rosenblatt and J. W. Van Ness, "Estimation of the bispectrum," *The Annals of Mathematical Statistics*, pp. 1120–1136, 1965.

[92] C. L. Nikias and M. R. Raghuveer, "Bispectrum estimation: A digital signal processing framework," *Proceedings of the IEEE*, vol. 75, no. 7, pp. 869–891, 1987.

[93] M. L. Williams, "The use of the bispectrum and other higher order statistics in the analysis of one dimensional signals," PhD thesis, University of London, 1992.

[94] I Daubechies, "The wavelet transform, time-frequency localization and signal analysis," *IEEE Transactions on Information Theory*, vol. 36, no. 5, pp. 961–1005, 1990.

[95] I. Daubechies, *The wavelet transform, time-frequency localization and signal analysis*. Princeton University Press, 2009.

[96] E. Sejdic, I. Djurovic, and L. Stankovic, "Quantitative performance analysis of scalogram as instantaneous frequency estimator," *IEEE Transactions on Signal Processing*, vol. 56, no. 8, pp. 3837–3845, 2008.

[97] Y. Li and S. Zhou, "A new instantaneous wavelet bicoherence for local fault detection of rotating machinery," *IEEE Transactions on Instrumentation and Measurement*, vol. 69, no. 1, pp. 135–143, 2019.

[98] M. Farge, "Wavelet transforms and their applications to turbulence," *Annual Review of Fluid Mechanics*, vol. 24, no. 1, pp. 395–458, 1992.

[99] D. P. Percival, "On estimation of the wavelet variance," *Biometrika*, vol. 82, no. 3, pp. 619–631, 1995.

[100] J. Graves, J Horacek, R. Pitts, and K. Hopcraft, "Self-similar density turbulence in the tcv tokamak scrape-off layer," *Plasma physics and controlled fusion*, vol. 47, no. 3, p. L1, 2005.

[101] J Horacek, R. Pitts, and J. Graves, "Overview of edge electrostatic turbulence experiments on tcv," *Czechoslovak Journal of Physics*, vol. 55, no. 3, pp. 271–283, 2005.

[102] O. Garcia, "Stochastic modeling of intermittent scrape-off layer plasma fluctuations," *Physical review letters*, vol. 108, no. 26, p. 265 001, 2012.

[103] S. Kobayashi, B. N. Rogers, and W. Dorland, "Gyrokinetic simulations of turbulent transport in a ring dipole plasma," *Physical review letters*, vol. 103, no. 5, p. 055 003, 2009.

[104] ——, "Particle pinch in gyrokinetic simulations of closed field-line systems," *Physical review letters*, vol. 105, no. 23, p. 235 004, 2010.

[105] N Mahdizadeh, M Ramisch, U Stroth, C Lechte, and B. Scott, "Investigation of intermittency in simulated and experimental turbulence data by wavelet analysis," *Physics of plasmas*, vol. 11, no. 8, pp. 3932–3938, 2004.

[106] G. G. Howes, "The dynamical generation of current sheets in astrophysical plasma turbulence," *The Astrophysical Journal Letters*, vol. 827, no. 2, p. L28, 2016.